An Ultra-precise Measurement of the Weak Mixing Angle using Møller Scattering

December 15, 2008

Abstract

We propose to measure the parity-violating asymmetry A_{PV} in the scattering of longitudinally polarized 11 GeV electrons from the atomic electrons in a liquid hydrogen target (Møller scattering). In the Standard Model, A_{PV} is due to the interference between the electromagnetic amplitude and the weak neutral current amplitude, the latter being mediated by the Z^0 boson. A_{PV} is predicted to be 35.6 parts per billion (ppb) at our kinematics. Our goal is to measure A_{PV} to a precision of 0.73 ppb. The result would yield a measurement of the weak charge of the electron Q_W^e to a fractional accuracy of 2.3% at an average Q^2 of 0.0056 $(\mathrm{GeV/c})^2$.

In the Standard Model, the Q_W^e measurement yields a determination of the weak mixing angle $\sin^2\theta_W$ with an uncertainty of $\pm 0.00026(\mathrm{stat}) \pm 0.00013(\mathrm{syst})$, similar to the accuracy of the single best such determination from high energy colliders. Thus, our result could potentially influence the central value of this fundamental electroweak parameter, a critical input to deciphering signals of any physics beyond the Standard Model that might be observed at the Large Hadron Collider (LHC).

In addition, the measurement is sensitive to the interference of the electromagnetic amplitude with new neutral current amplitudes as weak as $\sim 10^{-3} \cdot G_F$ from as yet undiscovered high energy dynamics, a level of sensitivity that is unlikely to be matched in any experiment measuring a flavor and CP-conserving process over the next decade. This provides indirect access to new physics at multi-TeV scales in a manner complementary to direct searches at the LHC. Some examples of potential new physics effects for which our measurement extends sensitivity beyond current and planned low energy measurements include new Z' bosons, electron compositeness, supersymmetry and doubly charged scalars.

J. Benesch, P. Brindza, R.D. Carlini, J-P. Chen, E. Chudakov, S. Covrig, C.W. de Jager, A Deur, D. Gaskell, J. Gomez, D. Higinbotham, J. LeRose, D. Mack, R. Michaels, S. Nanda, G.R. Smith, R. Suleiman, V. Sulkosky, B. Wojtsekhowski
Jefferson Lab

H. Baghdasaryan, G. Cates, D. Crabb, D. Day, M. Dalton, N. Kalantarians, N. Liyanage, V.V. Nelyubin, B. Norum, K. Paschke, S. Riordan, M. Shabestari, J. Singh, A. Tobias, K. Wang, X. Zheng
University of Virginia

J. Birchall, M.T.W. Gericke, W.R. Falk, L. Lee, W.D. Ramsay, S.A. Page, W.T.H. van Oers
University of Manitoba

D.S. Armstrong, T.D. Averett, J.M. Finn, J. Katich, J.P. Leckey
College of William & Mary

K. Grimm, K. Johnston, N. Simicevic, S. Wells
Louisiana Tech University

K.S. Kumar [Contact*], D. McNulty, L. Mercado, R. Miskimen
U. Massachusetts, Amherst

L. El Fassi, R. Gilman, R. Ransome, E. Schulte
Rutgers University

J. Arrington, K. Hafidi, P.E. Reimer, P. Solvignon
Argonne National Lab

E. Fuchey, C. Hyde, F. Itard, C. Muñoz Camacho
LPC Clermont, Université Blaise Pascal

F. Benmokhtar, G. Franklin, B. Quinn
Carnegie Mellon University

W. Deconinck, S. Kowalski, B. Moffit
MIT

R. Holmes, P. Souder
Syracuse University

N. Morgan, M. Pitt
Virginia Polytechnic Institute and State University

P.M. King, J. Roche
Ohio University

J.A. Dunne, D. Dutta
Mississippi State University

A.T. Katramatou, G. G. Petratos
Kent State University

A. Ahmidouch, S. Danagoulian
North Carolina A&T State University

P. Decowski
Smith College

J. Erler
Universidad Autónoma de México

M.J. Ramsey-Musolf
University of Wisconsin, Madison

Yu.G. Kolomensky
University of California, Berkeley

K. A. Aniol
California State U.(Los Angeles)

C.A. Davis
TRIUMF

J.W. Martin
University of Winnipeg

E. Korkmaz
University of Northern British Columbia

T. Holmstrom
Longwood University

S.F. Pate
New Mexico State University

G. Ron
Tel Aviv University

P. Markowitz
Florida International University

F.R. Wesselman
Xavier University of Louisiana

*kkumar@physics.umass.edu

Contents

Chapter 1

Introduction and Motivation

1.1 Overview

The theory of electroweak interactions, which are unified via the $SU(2)_L \times U(1)_Y$ gauge structure of the Standard Model, has survived stringent experimental tests over more than three decades. Consistency has been achieved at the $\sim 0.1\%$ level, where electroweak radiative corrections involving the top quark, the massive vector bosons, and the Higgs boson become manifest. All experimental data to date, with direct access to a center of mass energy of order 200 GeV in e^+e^- collisions, and approaching 1 TeV in the hard scattering of partons in $p\bar{p}$ collisions, are in agreement with theoretical predictions. Nevertheless, compelling theoretical arguments, input from cosmological observations, and the discovery of neutrino mass strongly motivate the exploration of the multi-TeV scale via direct searches at colliders, as well as via higher-precision electroweak measurements at low energy.

We propose to measure the parity-violating asymmetry in the scattering of longitudinally polarized electrons off unpolarized electrons, using the upgraded 11 GeV beam in Hall A at Jefferson Laboratory. Such a measurement would constitute more than a factor of five improvement in fractional precision over the published measurement of the same quantity by the E158 experiment at SLAC [1]. The electron beam energy, luminosity and stability at Jefferson Laboratory are uniquely suited to carry out such a measurement, which would constitute a new benchmark in sensitivity to probe the validity of the electroweak theory at the multi-TeV scale.

There are two primary reasons why the proposed measurement represents a compelling new opportunity:

- The two most precise independent determinations of the weak mixing angle,

$\sin^2\theta_W$, differ by 3 standard deviations from each other. While the world average is consistent with other electroweak measurements and constraints on the Higgs boson mass M_H, choosing one or the other central value ruins this consistency and implies very different new high-energy dynamics. The proposed A_{PV} measurement is the only method available in the next decade to directly address this issue with an independent determination at the same level of precision and interpretability.

- New neutral current interactions are best parameterized model-independently at low energies by effective four-fermion interactions via the quantity Λ/g, where g characterizes the strength and Λ is the scale of the new dynamics. The proposed A_{PV} measurement is sensitive to new interactions as small as 1.5×10^{-3} times the Fermi constant, G_F, which corresponds to a sensitivity of $\Lambda/g \sim 7.5$ TeV. This would be *the* most sensitive probe of new flavor and CP-conserving neutral current interactions in the leptonic sector until the advent of a linear collider or a neutrino factory.

This unique opportunity to probe TeV-scale dynamics was recognized as such in the recently completed NSAC long range planning exercise. Direct searches and indirect probes have always been an essential package for determining the shape of the electroweak theory. Classic examples of measurements that played central roles with discoveries using indirect probes are the observation of parity-violation in nuclear beta decay, the observation of weak-electromagnetic interference in lepton-quark deep inelastic scattering, and the agreement between direct and indirect determinations of the mass of the top quark. The more recent result of the $(g-2)_\mu$ anomaly is perhaps the harbinger of a program in search of the "New Standard Model"; such a future initiative would involve many new nuclear physics experimental projects.

There were four important points to emphasize from the long-range planning process and the associated report [2]:

1. The field of Fundamental Symmetries is now recognized for its accomplishments and future potential to further the larger goals of Nuclear Physics. Notably, the SLAC E158 A_{PV} result in Møller scattering was highlighted as one of the important accomplishments of the field in the previous 7 years.

2. The third principal recommendation calls for significant new investment in this subfield and emphasizes the importance of precision electroweak experiments to further our understanding of fundamental interactions and the early universe.

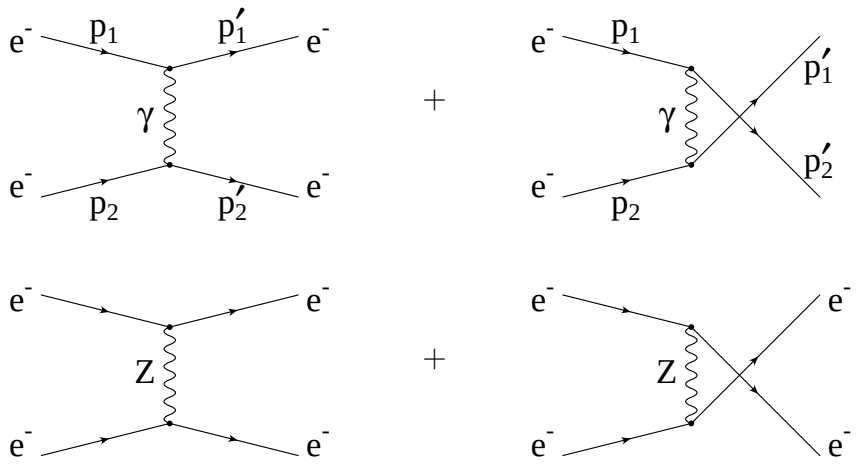

Figure 1.1: *Feynman diagrams for Møller scattering at tree level.*

3. One of the overarching questions that serves to define this subfield is: "What are the unseen forces that were present at the dawn of the universe but disappeared from view as the universe evolved?"

4. To address this question and as part of the third principal recommendation, significant funds were recommended for equipment and infrastructure for two new parity-violating electron scattering projects (Møller scattering and parity-violating deep inelastic scattering or PVDIS) that would use the upgraded 11 GeV beam at Jefferson Laboratory.

In the following, we introduce parity-violating electron scattering in general and Møller scattering in particular, the Standard Model prediction for A_{PV}, and then elaborate on the two bullets above.

1.2 A_{PV} in Møller Scattering

Polarized electron scattering off unpolarized targets provides a clean window to study weak neutral current interactions. These experiments measure an asymmetry defined by

$$A_{PV} = \frac{\sigma_R - \sigma_L}{\sigma_R + \sigma_L} \quad , \tag{1.1}$$

where σ_R (σ_L) is the scattering cross-section using incident right (left) handed electrons. A non-zero asymmetry constitutes parity nonconservation, dominated at $Q^2 \ll M_Z^2$ by the interference between the weak and electromagnetic amplitudes [3].

The leading order Feynman diagrams relevant for Møller scattering, involving both direct and exchange diagrams that interfere with each other, are shown in Fig. 1.1. The total unpolarized cross section, dominated by photon exchange, is given by

$$\frac{d\sigma}{d\Omega} = \frac{\alpha^2}{2mE}\frac{(3+\cos^2\theta)^2}{\sin^4\theta} = \frac{\alpha^2}{4mE}\frac{1+y^4+(1-y)^4}{y^2(1-y)^2}, \tag{1.2}$$

where α is the fine structure constant, E is the incident beam energy, m is the electron mass, θ is the scattering angle in the center of mass frame, $y \equiv 1-E'/E$ and E' is the energy of one of the scattered electrons. The parity-violating asymmetry A_{PV}, due to the interference between the photon and Z^0 boson exchange diagrams in Fig. 1.1, is given by [4]

$$A_{PV} = mE\frac{G_F}{\sqrt{2}\pi\alpha}\frac{4\sin^2\theta}{(3+\cos^2\theta)^2}Q_W^e = mE\frac{G_F}{\sqrt{2}\pi\alpha}\frac{2y(1-y)}{1+y^4+(1-y)^4}Q_W^e \tag{1.3}$$

where Q_W^e (proportional to the product of the electron's vector and axial-vector couplings to the Z^0 boson) is the weak charge of the electron. The electroweak theory prediction at tree level in terms of the weak mixing angle is $Q_W^e = 1 - 4\sin^2\theta_W$; this is modified at the 1-loop level [5, 6] and becomes dependent on the energy scale at which the measurement is carried out, *i.e.* $\sin^2\theta_W$ "runs". It increases by approximately 3% compared to its value at the scale of the Z^0 boson mass, M_Z; this and other radiative corrections reduce Q_W^e to 0.0469 ± 0.0006, a $\sim 40\%$ change of its tree level value of ~ 0.075 (when evaluated at M_Z).

The prediction for A_{PV} for the proposed experimental design is 35.6 parts per billion (ppb) and our goal is to measure this quantity with a statistical precision of 0.74 ppb and thus achieve a 2.3% measurement of Q_W^e. The reduction in the numerical value of Q_W^e due to radiative corrections leads to increased fractional accuracy in the determination of the weak mixing angle, $\sim 0.1\%$, comparable to the two best such determinations from measurements of asymmetries in Z^0 decays in the e^+e^- colliders LEP and SLC. At this level of accuracy, theoretical predictions of these processes must be made with full treatment of one-loop radiative corrections and leading two-loop corrections.

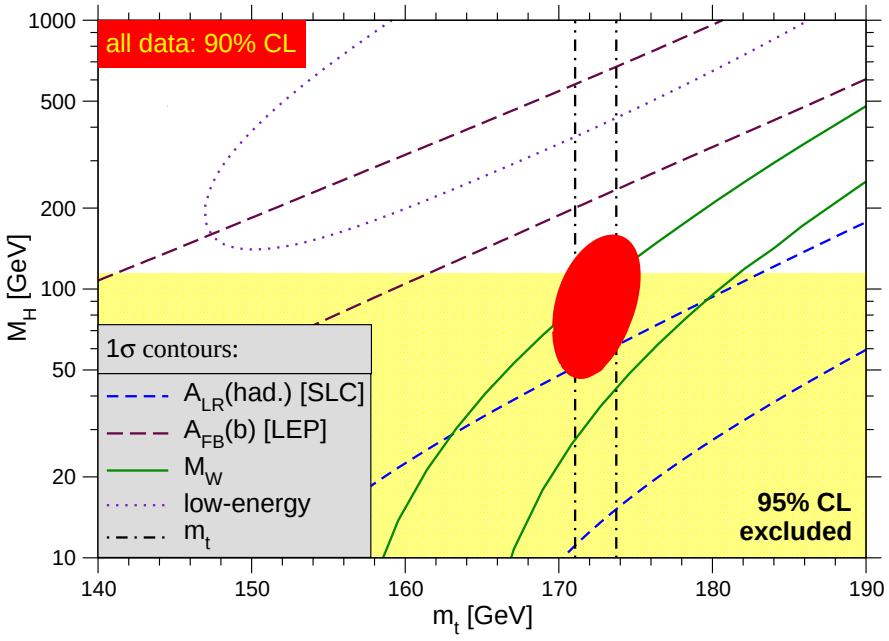

Figure 1.2: 1σ *bands from various precision measurements. The red (filled) ellipse is a 90% C.L. contour of all precision electroweak data. The shaded region is excluded via direct searches at colliders. The strongest constraint on the width of the purple (dotted) contour from current low-energy measurements is already now obtained from polarized Møller scattering (E158), while its shape and its location on the plot is mostly due to the NuTeV result [7, 8] on deep inelastic* ν*-scattering. As can be seen, it favors large values of* M_H*. The measurement proposed here would strongly dominate the future width and location of this contour.*

1.3 Precision Weak Mixing Angle Measurements

In order to test the electroweak theory at the one-loop level, one starts with three fundamental experimental inputs characterizing, respectively, the strength of electroweak interactions, the scale of the weak interactions, and the level of photon-Z^0 boson mixing. Precise theoretical predictions for all other experimental observables at the quantum-loop level can be made if experimental constraints on the strong

coupling constant and heavy particle masses, such as M_H and the top quark mass, m_t, are also included. The three fundamental inputs are chosen to be α (from the $e^{\pm}$ anomalous magnetic moment), G_F (from the muon lifetime) and M_Z (from the LEP Z^0 line-shape measurement).

Precision measurements of derived parameters such as the mass of the W boson, M_W, and the weak mixing angle, $\sin^2\theta_W$, are then used to test the theory at the level of electroweak radiative corrections. Consistency (or lack thereof) of various precision measurements can then be used to constrain the one unknown mass in the Standard Model, *i.e.* M_H, and search for indications of physics beyond the Standard Model.

Global analyses of all precision data have constrained the Standard Model Higgs boson to be within a relatively narrow window: 55 GeV $\leq M_H \leq$ 141 GeV at 90% C.L.. Further, direct searches at colliders require that the Higgs boson be heavier than 114.4 GeV at 95% C.L. [9]. The most precise inputs to the indirect limit come from precision measurements of various asymmetries in the production and decay of Z bosons at CERN and SLAC, and the measurements of the W boson mass from CERN and Fermilab.

While there is no significant conflict between direct and indirect limits on M_H, it is instructive to study the "pull" of individual measurements, as depicted in Fig. 1.2. Various measurements of the W boson mass are mutually consistent and the green (solid) line shows the 1σ allowed band of the grand average. The two dashed bands are the constraints from the most precise single determinations of the weak mixing angle, the blue (short-dashed) one from the left-right asymmetry in Z production at SLC ($A_{\rm LR}$(had)) and the maroon (long-dashed) one from the forward-backward asymmetry in Z decays to b-quarks ($A_{\rm FB}(b)$ [LEP]) [10].

With the constraint from the direct measurement of m_t from Fermilab (dot-dashed vertical black lines in Fig. 1.2), it can be seen that the M_W band points to a low M_H, almost (but not quite) in disagreement with the direct exclusion limit. However, the M_H constraints from the two weak mixing angle measurements are quite different [11]. On the one hand, the left-right asymmetry measurement in Z production from SLC $A_{\rm LR}$(had)) indicates a very small M_H which is already ruled out by direct searches. On the other hand, the forward-backward asymmetry measurement in Z decays to b-quarks from CERN ($A_{\rm FB}(b)$ [LEP]) indicates a very large M_H and is in tension with constraints from all indirect measurements (solid red ellipse). It is evident that a third determination of the weak mixing angle with similar precision is needed and would have a major impact on our view of the data. It could also guide particle phenomenology along the correct path to interpret indications of physics beyond the Standard Model that might be observed at the

LHC.

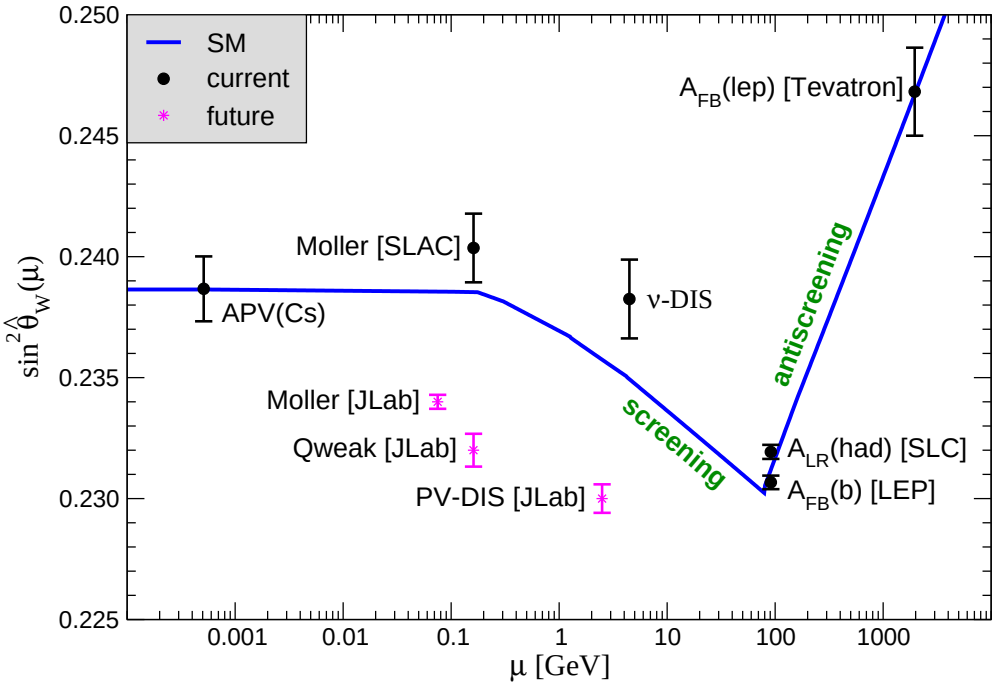

Figure 1.3: *Current and proposed weak mixing angle measurements vs. the energy scale μ. The three future measurements are located at appropriate μ values but the vertical locations are arbitrary.*

An additional advantage of the proposed measurement, which was not relevant to the discussion above, is that it would be undertaken at a low 4-momentum transfer scale, in contrast to the SLC and CERN measurements, both of which were carried out at the top of the Z^0 resonance. This difference in energy scales enhances the sensitivity of the proposed measurement dramatically to as yet undiscovered super-weak interactions at the TeV scale, which we discuss in the next section.

A convenient way to track various electroweak measurements is to use $\sin^2\theta_W$ as a bookkeeping parameter. As mentioned earlier in the discussion of the theoret-

ical prediction for A_{PV}, $\sin^2\theta_W$ "runs" due to electroweak radiative corrections, as shown in Fig. 1.3. Apart from the proposed measurement and the two Z^0 resonance measurements discussed above, various published and proposed measurements at different energy scales are also shown.

1.4 Contact Interactions

A fairly general and model-independent way to quantify the effects of new high energy dynamics in low energy processes is to express the resulting new amplitudes in terms of 4-Fermi contact interactions among leptons and quarks. Specializing here to vector and axial-vector interactions between electrons and/or positrons, such an interaction Lagrangian takes the form [12]:

$$\mathcal{L}_{e_1e_2} = \sum_{i,j=L,R} \frac{g_{ij}^2}{2\Lambda^2} \bar{e}_i \gamma_\mu e_i \bar{e}_j \gamma^\mu e_j, \tag{1.4}$$

where $e_{L/R} = \frac{1}{2}(1 \mp \gamma_5)\psi_e$ are the usual chirality projections of the electron spinor, Λ is the mass scale of the contact interaction, $g_{ij} = g_{ij}^*$ are coupling constants, and $g_{RL} = g_{LR}$.

For the proposed measurement with 2.3% total uncertainty, the sensitivity can be expressed as:

$$\frac{\Lambda}{\sqrt{|g_{RR}^2 - g_{LL}^2|}} = \frac{1}{\sqrt{\sqrt{2}G_F|\Delta Q_W^e|}} \simeq \frac{246.22 \text{ GeV}}{\sqrt{0.023 Q_W^e}} = 7.5 \text{ TeV}. \tag{1.5}$$

For example, models of lepton compositeness are characterized by strong coupling dynamics. Taking $\sqrt{|g_{RR}^2 - g_{LL}^2|} = 2\pi$ shows that mass scales as large as $\Lambda = 47$ TeV can be probed, far beyond the center of mass energies of any current or planned high energy accelerator. This allows electron substructure to be studied down to the level of 4×10^{-21} m.

The best current limits on contact interaction scales come from the high energy collider data of LEP 2 and the Tevatron, where the latter is sensitive to new interactions involving quarks. The strongest constraints on the coefficients in Eqn. (1.4) come from LEP 2. We emphasize, however, that the parity-conserving cross-sections and forward-backward asymmetries studied at LEP 2 are only sensitive to g_{RL}^2 and the combination $g_{RR}^2 + g_{LL}^2$. Making the additional assumption that the former (latter) is vanishing, the combination of all four LEP 2 experiments corresponds to

sensitivities of $\Lambda/\sqrt{g_{RR}^2 + g_{LL}^2} = 4.4$ TeV ($\Lambda/g_{RL} = 5.2$ TeV) while LEP 2 is blind to the parity-violating combination $g_{RR}^2 - g_{LL}^2$ probed by A_{PV}.

Thus, the proposed measurement would greatly extend the current sensitivity of 4-electron contact interactions both qualitatively and quantitatively[1]. Using Eqn. (1.5), it is also straightforward to examine its reach in specific models [13]. We discuss three examples below.

1.4.1 Supersymmetry

At the level of sensitivity probed, the proposed measurement could be influenced by radiative loop effects of new particles predicted by the Minimal Supersymmetric Standard Model (MSSM). The impact on the weak charges of the electron and the proton $Q_W^{e,p}$ have been analyzed in detail [14]. We reproduce the results here from a recent review [15]. In Fig. 1.4, the dots on the right hand side show the results of a random scan over a set of MSSM parameters whose values are consistent with current precision measurements and search limits. Generally speaking, there is a modest increase in the effects at larger values of the MSSM parameter $\tan\beta$ (the ratio of vacuum expectation values of the model's two Higgs scalars) or if one of the superpartner masses is relatively light. The allowed loop contributions to Q_W^e can be as large as +8% which, given our projected error bar, would constitute a deviation of 3.5 σ.

If the assumption of R-parity conservation is relaxed (RPV), tree-level interactions could generate even larger deviations in Q_W^e. The left-hand side of Figure 1.4 shows the allowed region in the parameters Q_W^e and Q_W^p after constraints from low-energy precision data have been taken into account. In this case, relative deviations from the Standard Model value of Q_W^e of up to −18% are allowed, a shift of almost 8 σ. The predicted correlations between the approved 4% Q_W^p measurement and our proposed Q_W^e measurement will provide tighter constraints than either measurement alone, another example of complementarity between precision electroweak experiments.

It should be emphasized that if nature is indeed supersymmetric, the sign of the relative shift in Q_W^e would, if large enough, distinguish between R-parity conserving (RPC) and RPV versions of SUSY. The difference is not academic, since RPC would imply that the lightest supersymmetric particle is stable and therefore an obvious

[1] Our proposed measurement is also complementary to new physics searches via the Electric Dipole Moment (EDM) of the electron which is modified only if the new interactions violate CP symmetry.

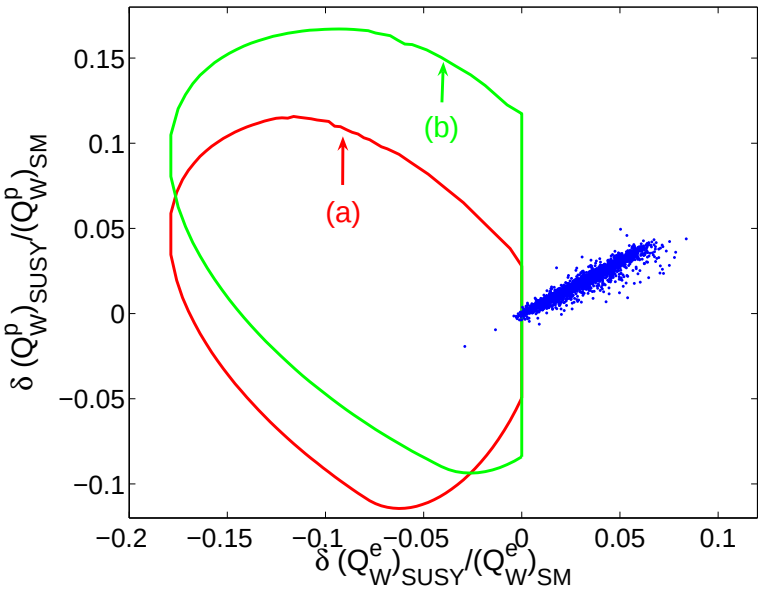

Figure 1.4: *Relative shifts in the electron and proton weak charges due to SUSY effects. Dots indicate the range of allowed MSSM-loop corrections. The interior of the truncated elliptical regions give possible shifts due to R-parity violating (RPV) SUSY interactions, where (a) and (b) correspond to different assumptions on limits derived from first row CKM unitarity constraints.*

candidate for the non-baryonic dark matter which is needed to understand galactic-scale dynamics. On the other hand, RPV would imply that neutrinos are Majorana particles. A 5% effect in Q_W^e interpreted as arising from RPV SUSY would generate a one-loop contribution to the neutrino mass of the order of 1 eV, comparable to current bounds.

1.4.2 Z′ Bosons

Many theories of new TeV-scale dynamics predict the existence of new, super-massive Z' bosons with masses in the TeV range. The LHC will be able to probe the region from 1 to 5 TeV, which is currently unexplored by any direct or indirect measurement. While the ultimate discovery reach of the LHC is about 5 TeV, it will be difficult to subject Z' bosons to detailed LHC measurements and to learn a significant amount beyond its mass. If an excess is seen at the LHC, low-energy mea-

surements such as the one proposed here would help to decipher what has actually been discovered.

The picture would improve after a luminosity upgraded LHC (SLHC) will have collected close to 1,000 fb^{-1}. Only then, and if the new boson is in the 1 to 2 TeV mass range, will CERN measurements of couplings become possible, a necessity to derive the charges of the $U(1)'$ symmetry that would underly the extended electroweak theory. However, it has been pointed out that even in this case, the SLHC is unable to separate out the leptonic and hadronic chiral couplings given the observables that would be analyzed. In particular, LHC measurements would at best be able to measure the ratio of the chiral leptonic couplings.

The proposed A_{PV} measurement would see an observable shift in many models that predict Z' bosons in the 1 to 2 TeV mass range. In the following we identify the chiral Z' couplings times $U(1)'$ charges to right-handed and left-handed electrons with g^2_{RR} and g^2_{LL}, and we also identify Λ with the Z' mass, $M_{Z'}$. For example, for the so-called Z_χ boson appearing in $SO(10)$ Grand Unified Theories one predicts

$$\sqrt{|g^2_{RR} - g^2_{LL}|} = \sqrt{\frac{4\pi\alpha}{3\cos^2\theta_W}} \approx 0.2,$$

implying that Z_χ bosons with masses up to about 1.5 TeV could affect the proposed measurement. Similarly, the Z_{LR} boson appearing in left-right symmetric models couples with strength

$$\sqrt{|g^2_{RR} - g^2_{LL}|} = \sqrt{\frac{\pi\alpha}{\cos^2\theta_W(1 - 2\sin^2\theta_W)}} \approx 0.24,$$

corresponding to a 1.8 TeV reach for this boson. Updating the analysis in reference [16] we obtain the current bound $M_{Z_\chi} > 1.16$ TeV and $Z_{LR} > 1.02$ TeV at 95% CL.

The impact of new constraints from the proposed A_{PV} measurement and SLHC has recently been demonstrated in these two specific models [17] and is depicted in Fig. 1.5. For technical reasons, masses and couplings have been scaled in the figure by a factor of 1.25. Given the couplings above, the figure corresponds to Z' masses of 1.2 TeV *i.e.* slightly above the current lower bounds. It can be seen that the proposed measurement would provide an important constraint such that a combined analysis with the SLHC data would allow for independent determinations of the left- and right-handed leptonic Z' couplings and make it thus possible to distinguish between models.

We should mention that Z' limits at colliders are often discussed together with mass limits on Kaluza-Klein gravitons in models with large extra dimensions. These

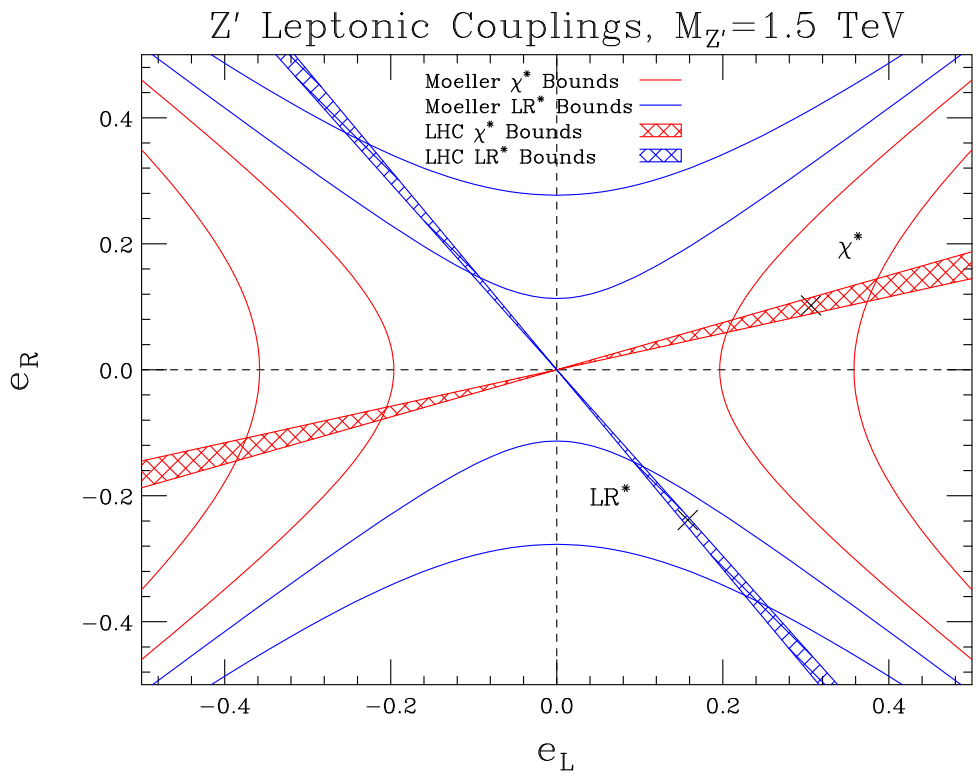

Figure 1.5: *Future constraints on chiral Z' couplings in two representative models for a 1.5 TeV mass. The hyperbolas are from a potential A_{PV} measurement while the hatched regions are from an SLHC. The latter were obtained assuming a given model with the parameters as discussed including statistical errors and uncertainties from parton distribution functions. There is a reflection symmetry (a doubling of the bands) because of an overall unphysical sign ambiguity. (Figure courtesy of F. Petriello et al.)*

may be difficult to disentangle from extra Z' bosons. Since their effects are very strongly suppressed for the low energy measurements of the type proposed here these would then serve as valuable control measurements.

1.4.3 Doubly-Charged Scalars

Doubly charged scalars naturally arise in extended Higgs sector models that contain complex triplet representations of SU(2). The left-right symmetric model, for

example, contains two such triplets – Δ_L and Δ_R – that transform under $SU(2)_L$ and $SU(2)_R$ respectively. The doubly-charged components of both triplets, $\delta^{++}_{L,R}$ can couple to two charged leptons:

$$\mathcal{L}^{\delta^{++}}_{\text{matter}} \sim h^{ij}_L \, \delta^{++}_L \bar{\ell}^C_i P_L \ell_j + h^{ij}_R \, \delta^{++}_R \bar{\ell}^C_i P_R \ell_j + \text{h.c.} \tag{1.6}$$

where ℓ_i denotes a charged lepton of generation i. The Møller scattering process is unique among lepton scattering observables to be sensitive to the $s-$channel exchange 4-electron amplitude that violates lepton number by 2 units:

$$\mathcal{M}^{\text{PV}} \sim \frac{|h^{ee}_{L,R}|^2}{2M^2_{\delta_L}} \bar{e_L} \gamma_\mu e_L \bar{e_L} \gamma^\mu e_L \quad , \tag{1.7}$$

with an analogous expression for right-handed projections.

Gauge and matter interactions involving the $\delta^{++}_{L,R}$'s can also lead to contributions to neutrinoless double-beta decay processes and charged lepton flavor violating processes such as $\mu \to e$ conversion [18]. In general, these processes can put severe limits on these possible new amplitudes, but in the latter case only in models predicting unsuppressed off-diagonal charged lepton couplings $h^{\mu e}_{L,R}$. Neutrinoless double-beta decay gives much weaker constraints for the Δ_L triplet because its vacuum expectation value is constrained to be smaller than a few GeV from electroweak precision data (the ρ parameter).

The amplitude in Eqn. (1.7) shows that the Δ_L model is equivalent to a contact interaction with $\Lambda = M_{\delta_L}$, $|g^2_{LL}| = |h^{ee}_L|^2/2$, and $g_{RR} = g_{LR} = 0$. The proposed A_{PV} measurement would therefore lead to the most stringent probe of the left-handed charged scalar and its coupling to electrons, with a reach of

$$\frac{M_{\delta_L}}{|h^{ee}_L|} \sim 5.3 \text{ TeV},$$

significantly above the LEP 2 constraint of about 3 TeV.

Chapter 2

Experimental Design

The experimental collaboration would base the design on the extensive experience gained from completed high flux integrating parity-violation measurements such as MIT-Bates ^{12}C [19], SAMPLE [20], HAPPEX [21] and SLAC E158 [1] as well as ongoing projects such as PREX [22] and Qweak [23]. In this chapter, we provide an overview of the experimental design and discuss the most important subsystems. Detailed considerations on each subsystem can be found in a series of appendices. We start by listing the main experimental parameters in Table 2.1. Since many of the technical choices are driven by our desire to measure a very small parity-violating asymmetry, collecting data at a very high rate is a priority.

2.1 Polarized Beam

The polarized electron beam is created using a technology first developed at SLAC to enable the original parity-violating electron scattering experiment [24]: laser-induced photoemission from a GaAs wafer. The circular polarization of the laser light determines the sign of the longitudinal polarization of the emitted electron bunch, thus facilitating rapid helicity reversal of the electron beam. Time "windows" are generated in the electron bunch train at a frequency of 2 kHz, with the sign of the beam's longitudinal polarization in each window assigned on a pseudo-random basis. For this proposal, we plan to use a beam intensity of 85 μA.

Nearby time windows of opposite helicity form window-pairs. After acceleration, the time-averaged responses of beam position monitors characterize the beam trajectory and energy for each window. The monitoring instrumentation has to be precise enough so that the relative cross-section (except for the influence of counting

Table 2.1: *Nominal design parameters for the proposed A_{PV} measurement.*

E (GeV)	11.0
E' (GeV)	1.8 - 8.8
θ_{cm}	46°-127°
θ_{lab}	0.23°-1.1°
$< Q^2 >$ (GeV/c)^2	0.0056
Current (μA)	85
Target Length (cm)	150
ρ_{tgt} g/cm^3 (T= 20K, P = 35 psia)	0.0715
Luminosity $cm^{-2}sec^{-1}$	$3.4{\cdot}10^{39}$
Time in weeks (hours)	30 (5040)
σ (μBarn)	45.1
Møller Rate (GHz)	153
Statistical Width(2 kHz flip, ppm/pair)	77.9
target raster size (mm)	5 x 5
ΔA_{raw} (ppb)	0.58
background fraction	8.3%
P_{beam}	85%
$< A_{pv} >$ (ppb)	35.6
ΔA_{stat} (ppb)	0.74
$\Delta A_{stat} / < A_{expt} >$	2.08%
$\delta(\sin^2\theta_W)_{stat}$	0.00026

statistics) is stable over nearby time windows at the level one part in 10^5, after beam fluctuations are regressed out. Therefore, beam properties must be measured window by window with high accuracy and further, they must be virtually unchanged after each helicity reversal. This implies that the beam centroid must be measured with precision at the level of a few microns, and should be stable to ∼10 microns, at 1 kHz[1].

Averaged over the entire data collection period, the beam trajectory must remain unchanged with respect to the sign of the electron beam polarization at the sub-nanometer level. It will be necessary to use a "slow reversal" of beam helicity to further cancel beam asymmetries, in particular higher-order effects such as potential

[1]This does not include 60 Hz noise, since data will be collected in time-slots phased to 60 Hz.

helicity-dependent variations in the beam spot size. A reversal from spin manipulation in the electron beam injector will be used with a period on the order of one week. It will also be desirable to divide production running between two slightly different energies that only differ by a $g-2$ spin flip through spin precession in the accelerator. The detailed considerations that address these issues are described in App. A.

2.2 Liquid Hydrogen Target

After acceleration to 11 GeV, the electron beam will impinge on a liquid hydrogen target. Hydrogen is the ideal source of target electrons for two reason. First, it provides the greatest electron target thickness for the least radiation length. Secondly, the irreducible backgrounds are confined to radiative electron-proton elastic and inelastic scattering, which are relatively well-understood. Scattering off other nuclei would include elastic scattering ($\propto Z^2$), breakup channels and scattering off neutrons, which introduce significant systematic error due to unknown and potentially large electroweak couplings.

In order to achieve the necessary rate, more than 10 gm/cm^2 of liquid hydrogen is needed, making the target about 150 cm long, which in turn requires a cryogenic target system capable of handling a heat load of ~ 5 kW from the beam. This is far larger than the typical ~ 1 kW targets that are routinely in use and significantly larger than the planned target for the Qweak experiment.

Detailed technical considerations on the target design can be found in App. E. The preliminary assessment is that the E158 target cell is a good starting point for the design of the high power target required for this experiment. A possible path to sufficient target cooling was identified, though additional capital costs are required to implement the solution. Density variations at the helicity reversal frequency are also discussed. Scaling results from the G0 target to higher mass flow, larger rastered beam-spot size, and faster helicity reversal suggest the new target could have density fluctuations as large as 26 ppm corresponding to 5% excess noise. The uncertainties in these scaling arguments will diminish after the Qweak target is commissioned.

2.3 Hall A Layout

The experimental configuration downstream of the target is quite novel due to some remarkable features of the Møller scattering process. The topology of interest is in

the vicinity of 90° scattering in the center of mass (COM) frame. However, for a 11 GeV electron beam scattering off a target electron, the COM energy of each electron is 53 MeV. The laboratory frame is thus a heavily boosted frame and the laboratory scattering angles of interest are from 5 to 20 mrad. It also implies that scattered electrons in the laboratory frame between 2 and 8.5 GeV/c must be selected, a very large fractional momentum bite.

Finally, the measurement needs as much rate as possible and we must therefore accept scattered electrons over the full range of the azimuth. The available rate is more than 150 GHz. At this high rate, the only practical solution is to integrate the detector response of each window, eliminating dangerous dead-time problems. The integration technique requires that Møller-scattered electrons be focused into a region otherwise free of background. All of the above considerations have led us to a unique solution involving two back-to-back toroids, one them conventional (albeit long and quite skinny) and one quite novel. Collimation is a very important issue in such a system.

A schematic diagram of the apparatus situated in Hall A is shown in Fig. 2.1. The magnetic fields produce a ring focus of Møller-scattered electrons ~ 30 m downstream of the target at a radius of 0.95 m from the primary beam, out of line-of-sight of the target.

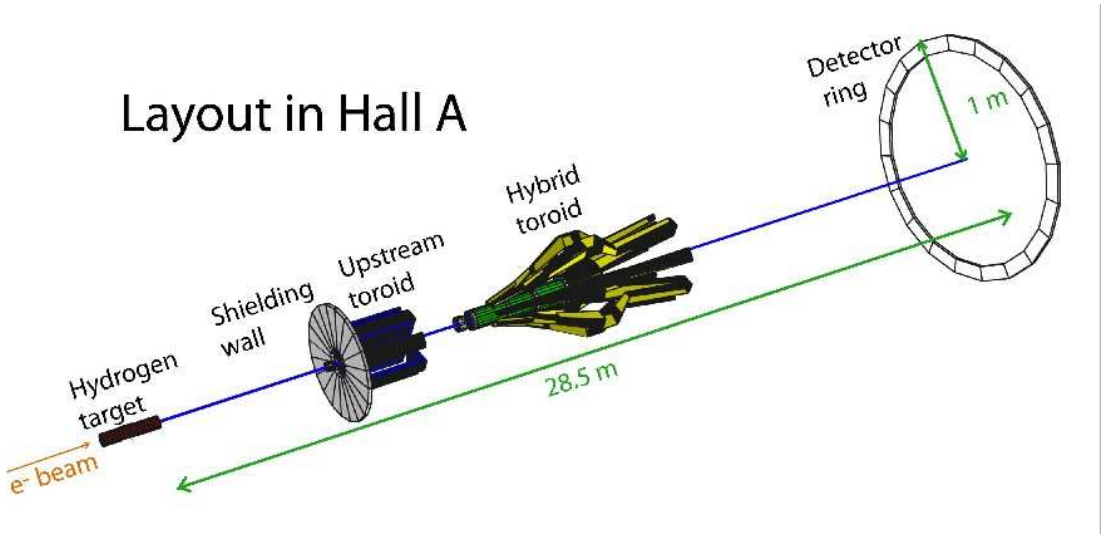

Figure 2.1: *Layout of the target, spectrometer and detectors in the Hall. The aspect ratio in this figure is 4:1.*

2.4 Toroidal Spectrometer

The salient features of the spectrometer/collimator system are:

- Full azimuthal acceptance for Møller-scattered electrons in the momentum range between 2.5 and 8.5 GeV/c.
- Clean separation from the primary background of elastic and inelastic electron-proton scattering, exploiting the energy-angle correlation of Møller electrons.
- Placement of detectors out of the line-of-sight of the target.
- Clean channel for the degraded beam and the associated hard bremsstrahlung photons to reach the beam dump.
- Minimization of photon backgrounds by designing a largely "two-bounce" system via judiciously placed collimators.

As discussed earlier, the selected Møller electrons represent a significant range in lab angle and energy and will emerge from a very long 1.5 meter target. Minimizing background rates to an acceptable level requires bringing these very different trajectories, from a large region of phase space, into a tight radial focus separated from the majority of the principle backgrounds. The solution is a combination of two toroidal magnets which together act in a non-linear way on the charged particle trajectories. The first is a conventional toroid placed 6 m downstream of the target and the second, a novel hybrid toroid placed between 10 and 16 m downstream of the target. The two toroidal fields are constructed out of seven azimuthally symmetric coils. This choice and the detailed description of the design of the two primary magnets is given in App. B.

2.5 Detectors

The toroidal spectrometer will focus the Møller scattered events onto a ring of 95 cm radius which is located 28.5 m downstream of the target center. (See Figure 2.2.) At the same z location, the more rigid electrons from elastic electron-proton scattering form a focus at the smaller radius of 70 cm. The electrons are selected by a primary collimator to come from seven sectors uniformly distributed in the azimuth and covering exactly one-half the azimuth.[2]

[2]This configuration contains 100% of the available statistics in the azimuth; see App. B.

Due to azimuthal defocusing in the magnets however, the Møller electrons populate the full range of the azimuth at the detector plane. It can be seen in Fig. 2.2 that stiffer tracks from electron-proton scattering at smaller radii do not defocus as much; gaps can be seen in the azimuthal distribution interspersed with areas of high density. Another demonstration of this effect can be seen in Fig. B.5 in App. B where the stiffer Møller tracks at smaller angle undergo smaller azimuthal defocusing. The detector must thus have radial and azimuthal binning for detailed understanding of the signal and background and for systematic checks.

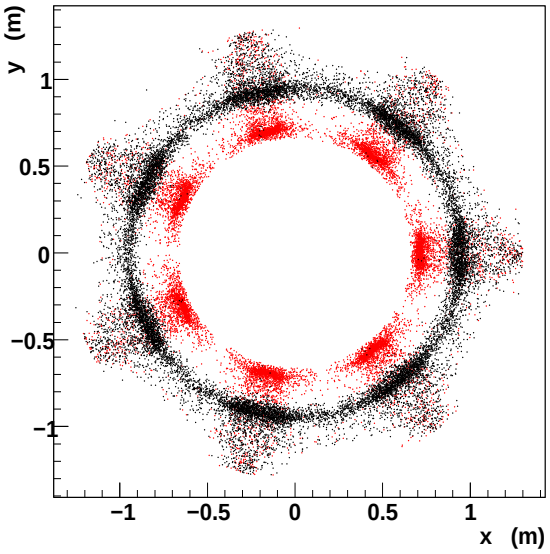

Figure 2.2: *Simulation of $e+e \rightarrow e+e$ (black dots) and $e+p \rightarrow e+p$ (red dots) final state electrons at $Z = 28.5$ downstream of the target center. The Møller electrons are bent by larger angles due to their lower average momenta and so appear at larger radii. The simulation includes initial and final state radiation in the target.*

As already mentioned, the detector response will be integrated over the duration of each helicity window to measure the scattered flux. Nevertheless, event-mode acquisition at much lower beam currents for systematic studies is also required. The detector must collect all Møller scattered events in the nominal acceptance, contribute negligible noise relative to the counting statistics of the signal, and be radiation-hard. Because the tail of all radiative electron-proton elastic and inelastic processes results in an important systematic correction, the detector must also be

able to measure these background electrons in *several* bins so trends in yield and asymmetry can be compared to simulations. Finally, the detector must be insensitive to soft backgrounds, minimize cross-talk between adjacent radial bins with widely different asymmetries, and not possess large biases between electron tracks which impact the detectors at different positions and angles.

The ideal detector material is artificial fused silica, since it is radiation-hard, and has negligible scintillation response. As described in App. C, the region between a radius of 0.6 to 1 m will be populated by a series of detectors with radial and azimuthal separation. This will produce measurements of A_{PV} for Møller scattering and equally important, also for the irreducible background processes of elastic and inelastic electron proton scattering. While most of the detectors will consist of 1-2 cm thick pieces of quartz, it is likely that the region of the Møller "peak" between 0.88 and 1 m will be augmented to be a "shower max" detector. Detectors would also be placed behind the main Møller detector and shielding to estimate hadronic background asymmetries. Finally, detectors at very forward angle would monitor window to window fluctuations in the scattered flux for diagnostic purposes. Conceptual designs for these detectors are presented in App. C.

2.6 Electronics and Data Acquisition

The integrated response of the Cherenkov light from electrons that traverse the detector is linearly proportional to the scattered flux. The parity-violating asymmetry is measured by averaging the fractional difference in the response of the detectors over many window-pairs. There are three aspects of the electronics and data acquisition (DAQ) specific to parity-violation experiments that are worth emphasizing, and we discuss them in the subsequent three paragraphs. The collaboration has extensive experience in these aspects of the experimental technique.

First, as mentioned earlier, the electronics must have the capability of measuring the fractional difference in the cross-section between two nearby time windows of opposite helicity with a resolution of less than 10 ppm, so that this quantity is dominated by the counting statistics of the scattered flux, which is expected to be 77 ppm. This in turn requires the ability to measure the integrated response of beam current monitors, beam position monitors, and Møller detectors' Cherenkov light photodetectors with low-noise electronics. This is described in detail in App. D.

Second, the Møller detectors' response to fluctuations in first-order beam parameters such as intensity, position, angle and energy must be continuously calibrated *simultaneously* with the collection of production data. The various ways of

accomplishing this at Jefferson Laboratory have already been implemented during HAPPEX and G0 measurements, including extensive collaboration with personnel from Accelerator Operations and careful consideration of impact on other Halls.

Finally, the success of the experiment will depend on careful preparation of the initial polarization states of the electron beam, which begins with a careful setup of the laser transport electronics of the polarized source. During data collection, there will be extensive electronic communication with optical and magnetic devices at the low energy end of the machine as various automated feedback loops of varying time frequencies will have to be incorporated. These systems will have to be implemented while paying careful attention to potential electronic cross-talk problems for which the proposed measurement will have sensitivity at an unprecedented level. Again, the collaboration has extensive experience on this aspect of the measurement.

Chapter 3

Systematic Control

The proposed A_{PV} measurement in some sense constitutes a fourth generation parity-violation experiment at Jefferson Laboratory. Apart from the obvious challenge of measuring a raw asymmetry with a statistical error of 0.58 ppb, an equally challenging task is to maintain and calibrate the absolute normalization at the 1% level. The collaboration continues to gain extensive experience on all aspects of such measurements as work continues on developing and executing the third generation experiments PREX [22] and Qweak [23]. In the following, we describe some of the principal challenges of controlling systematic errors in the proposed measurement.

3.1 Helicity Correlated Beam Asymmetries

Any change in the polarized beam, correlated to helicity reversal, can be a potential source for a false asymmetry. We have estimated the expected leading causes of beam-related systematic uncertainty and conclude that they can each be controlled at the desired level. Under reasonable assumptions, the helicity-correlated beam changes in intensity and trajectory will each contribute uncertainties at the level of 0.05 ppb. A possible helicity-correlated variation in the size of the electron beam spot introduces additional uncertainty of $\sim$0.1 ppb. We briefly expand on these conclusions in the following; more details can be found in App. A.

Extensive tools for tightly controlling beam intensity changes under helicity reversal have been developed in previous experiments. The nonlinearity between the detectors and beam current monitors is typically controlled at the 0.5% level. Given the goal of 0.05 ppb contributed error, this implies that the run-averaged intensity asymmetry must be smaller than 10 ppb. Intensity feedback will be employed to

assure convergence within that bound.

A change in beam position or angle will result in a change in the measured flux. Numerical estimates of such changes were made using Monte Carlo simulation, with results which are similar to expectations based on scaling the beam-motion sensitivities measured in HAPPEX-II. From these estimates, the detected flux in one azimuthal segment of the spectrometer is expected vary by approximately 8.5 ppb/nm, and approximately 85 ppb/nanoradian.

A large degree of cancellation of this position and angle senstivity is expected when considering the full azimthal symmetry of the detector. A conservative estimate of a factor 10 reduction in sensitivity is taken to account for detector alignments tolerances. After applying corrections for small position and angle differences, an uncertainty of approximately 10% is likely to remain. Accordingly, in order to keep the contributed uncertainty to less than 0.05 ppb, the helicity-correlated position differences, averaged over the run, must be kept to less than 0.5 nm and the angle differences to less than 0.05 nrad.

As discussed in App. A, it is a reasonable goal to hold the systematic offset in the beam centroid due to helicity reversal to these specifications. During the relatively short HAPPEX-II experiment, position differences were kept to less than 2 nm and angle differences to less than 0.2 nrad; only a modest improvement over these goals is required. However, given the likely level of random beam jitter, convergence to these small values is not guaranteed. It is likely that feedback on measured helicity-correlated position and angle differences will be necessary in order to assure convergence within the required precision specifications in the run time proposed.

The sensitivity to changes in the spot size has been estimated as well, and are found to be at the level of (12 ppm)$\times\delta\sigma/\sigma$. Work on the laser table should be able to bound the spot size asymmetry to be less than 10^{-4}, in which case the potential effect would be as large as 1 ppb before cancellation. Since this effect should not change sign with the injector solenoid spin-manipulation, or a $g-2$ spin flip via energy change, we assume a factor of 10 suppression from cancellation, so that the net contribution will be at the level of 0.1 ppb.

Taken together, helicity-correlated changes in the beam are expected to contribute around 0.14 ppb uncertainty. Extensive details justifying these assertions and our overall strategies are provided in App. A.

3.2 Longitudinal Beam Polarization

The experiment requires a relative accuracy of the electron beam polarization measurement at the level of ∼0.4%. A comparable level of accuracy has been previously achieved by the SLD collaboration [26] using a Compton polarimeter with a $\sim$ 46 GeV pulsed beam at SLAC. JLab has accumulated extensive experience with polarimetry below 6 GeV, and presently boasts two separate polarimeters with quoted accuracies at or near the 1% level. However, these polarimeters have never been cross-checked with each other at this level of precision, nor has any experiment yet matched this level of precision on a beam polarization observable.

The prospects for improving polarimetery at JLab to the necessary level are good. Upcoming experiments in the JLab "6 GeV" program, in both Halls A and C, require 1% polarimetry [22, 27, 28, 23]. These requirements will lead to the upgrade of the Hall A Compton polarimeter, the development of a Hall C Compton polarimeter and improvements to existing Moller polarimeters which use ferromagnetic foil targets. These 6 GeV experiments will be an excellent introductory challenge to very high-accuracy polarimetry at JLab, and should sharpen techniques both in controlling systematic uncertainties and in cross-comparing high-precision polarimeters.

In order to reach a robust 0.4% accuracy, we propose to develop two separate, continuous polarimeters for the current proposal, each independently normalized to that level of accuracy. Each polarimeter should provide a 0.4% statistical precision in comparable time periods of not more than several hours, in order to facilitate cross-checks and systematic studies. This redundancy, both in the measurement and monitoring of the beam polarization, will provide a new benchmark in precision electron beam polarimetry. We discuss both polarimeters in extensive detail in App. G and App. F.

3.3 Transverse Beam Polarization

If there is any transverse polarization component to the beam on target, the apparent A_{PV} as a function of the azimuthal angle would show a modulation due to the vector analyzing power A_T in Møller scattering, a QED effect involving the interference between the tree-level amplitudes and the two-photon exchange amplitudes. The relevant parameter for A_T is the center of mass beam energy, which is 53 MeV, and the electron's boost factor in the rest frame is rather modest. The magnitude of A_T is such that even a few percent transverse polarization can result in an azimuthal

modulation of the measured polarization asymmetry that is an order of magnitude larger than A_{PV}. While this effect should cancel if one averages data over the full range of the azimuth, imperfect cancellation could lead to a significant systematic error.

There are some interesting features of A_T that facilitate a strategy that would allow us to keep this potential systematic error under control. First, if one looks at A_T as a function of the COM scattering angle, or equivalently $y \equiv 1-E'/E$, one finds that A_T must vanish at $y = 1/2$, which corresponds to 90° scattering in the COM frame, due to CP symmetry. Thus, the maximum A_T occurs at $|y-0.5| \sim 0.2$, at the very edges of the momentum acceptance and more importantly, A_T is of opposite sign at these two extremes. This leads to an order of magnitude suppression in the effective A_T averaged over all detectors in a sector.

Figure 3.1 shows the polarization asymmetry for an incoming beam that is 100% transversely polarized, in each of the 7 ϕ-sectors. The three colors represent the three different ϕ-specific detectors, each of which contain very different y distributions. The black line shows the estimate of the average of the three detectors, corresponding to A_T of $\sim$ 1.5 ppm. Note how the average depends quite sensitively on how the three detectors are weighted (pure counting on the left vs energy weighting on the right).

It is possible by passive setup procedures to limit the transverse component of the beam polarization at the target to be less than 1°. However, this implies that the "blue" detectors might see an azimuthal modulation in the measured polarization asymmetry as large as 100 ppb after initial setup.

As can be seen from the figure, one can measure the ϕ modulation to very high precision within a few hours. Thus, it should be possible to devise a feedback loop that would make small tweaks to the launch angle of the electron beam polarization at the low energy end of the machine based on the measured A_T's in the three kinds of azimuthal detectors over the previous few hours. This technique is designed to converge to zero transverse polarization. In practice, the suppression should go like $1/N$, where N is the number of adjustments. In principle, we should gain a factor of about 25 below the setup accuracy of 1° in a week. We will assume this factor for the duration of the entire data collection period for the estimate of the systematic error.

If one now further conservatively assumes only a factor of 10 suppression in the grand average of A_{PV} over the full range of detectors, then the total systematic error from the correction to A_{PV} is less than 0.07 ppb. If this level of suppression is difficult to achieve in practice, some of it can be recovered by a slightly different reweighting of the data from the three detector types (to flatten out the black line in

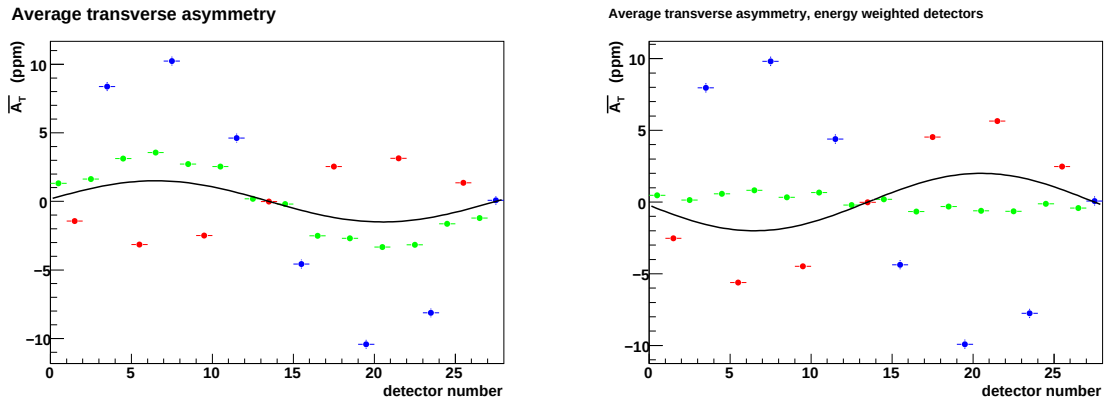

Figure 3.1: *Plot of average vector analyzing power for each of the three detector types, which have different y acceptance. The black curve represents the average transverse asymetry after further averaging over the four detectors in each complete segment. Error bars represent uncertainty in measurement after 1 hour of running at 85 μA. The left plot is for the case of counting detectors while the right plot is for the case of calorimeters (i.e. energy weighting). Color convention from Fig. B.8.*

the figure), with only a small loss in the statistical error in the measured longitudinal polarization asymmetry.

3.4 Absolute Value of Q^2

For momentum transfers $Q^2 \ll M_Z^2$, the parity-violating asymmetry in electron scattering at tree level is proportional to Q^2. The uncertainty in the Q^2 acceptance of the experiment therefore contributes directly to the ultimate uncertainty on Q_W^e. Our goal is to determine the average value of Q^2 in our detector acceptance with an error of 0.5%. Most of the techniques discussed below will be applied to the upcoming Qweak experiment which, due to the 1 GeV beam energy, will require relative corrections which are only a factor of 4 smaller than those in the present proposal.

The average Q^2 can be determined from a detailed Monte Carlo integration of $Q^2 = 4EE' \sin^2 \theta/2$ over the acceptance, where E is the beam energy determined by Hall A energy measurement systems, E' is given by 2-body kinematics, θ is the electron laboratory scattering angle at the $e + e$ vertex, and events are weighted

by the known $e + e \rightarrow e + e$ cross section. In the approximation where radiation is neglected, scale-type errors in dQ^2/Q^2 can be quite small, as given in Table 3.1. However, since the target is a 17% radiator, an average beam electron is significantly modified while passing through the target: it has multiple-scattered by more than 5% of the minimum accepted scattering angle and it can lose hundreds of MeV due to ionization and bremsstrahlung. This last, large correction for radiative energy loss is accurately predicted by QED at low momentum transfer for a Hydrogen target, but it is obviously critical that we benchmark the Monte Carlo by taking data with fast tracking detectors at nA-scale beam currents with target cells of different lengths.

Because the detectors will be oversized, the geometrical acceptance is largely defined by the target length and collimator apertures, plus a small dependence on rastered beam size. However, the presence of a radiative tail will introduce some dependence of the Q^2 acceptance on the detector outer radial cutoff as well as the spectrometer tune. This higher order issue will be constrained by a combination of careful survey of the detectors and the fast tracking detectors in order to confirm the spectrometer tune. Another higher-order issue which can be examined with fast tracking detectors is the extent to which the Tungsten collimators are not 100% absorptive, potentially yielding energetic electron shower products which end up in the detector acceptance.

Table 3.1: *Scale-type contributions to the error on Q^2 when radiation is neglected. The distance to the acceptance-defining collimator is 10 meters. The center of the collimator is taken to be at 12 cm radius from the beamline. Note that the error dR/R is the uncertainty in the radial coordinates of the as-built collimator conservatively determined using a Coordinate Measuring Machine. Small radial misalignments have negligible effect on Q^2 due to the azimuthal symmetry of the collimation system.*

Parameter	Uncertainty	Contribution to dQ^2/Q^2
dE/E (beam energy)	$< 5 \times 10^{-4}$	$< 0.1\%$
dL/L (tgt center to collimator)	< 5 mm	$< 0.1\%$
dR/R (error on collimator center)	< 0.1 mm	$< 0.17\%$
Total		$< 0.25\%$

3.5 Backgrounds

3.5.1 Elastic *ep* Scattering

The principal irreducible background under the Møller "peak" is radiative elastic electron-proton scattering. This is most clearly seen in Fig. 3.2, where the red curve between the black vertical lines constitutes 8.3% of the signal. The background is quite easily modeled and then verified explicitly with auxiliary measurements of the radial profile of the scattered flux. The parity-violating asymmetry is also well known for this process. In particular, the Qweak measurement of the weak charge of the proton Q_W^p will directly be applicable to the prediction for this background asymmetry.

In order to estimate the background correction, one also needs to know the average Q^2 of the elastically scattered events off the proton that are accepted. The Q^2 distributions for the three different detectors are shown in Fig. B.7. The average is 0.004 GeV^2. Assuming an uncertainty of 4% on the knowledge of Q_W^p, this leads to a 0.3% systematic error

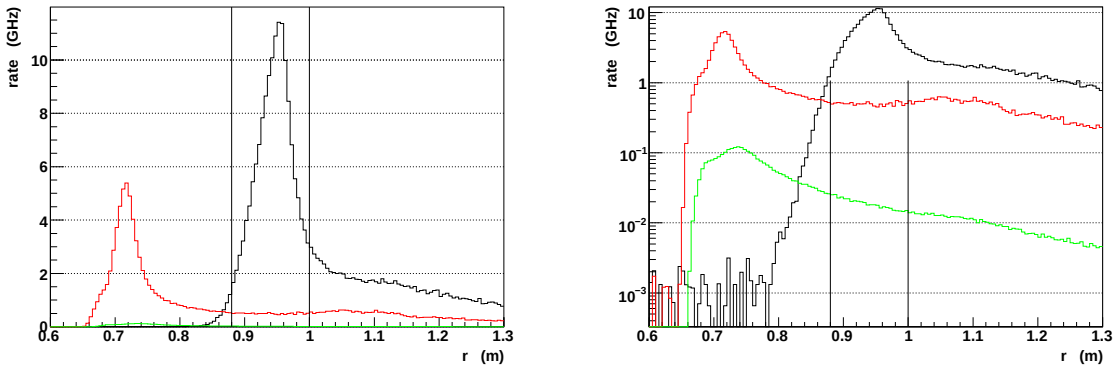

Figure 3.2: *Expected rate at radial position of elastic e-p (red) electrons, inelastic e-p electrons (green) and Møller (black) electrons at a plane 28.5 m downstream of the centre of the target. Bins are 5 mm wide. The black vertical lines represent the edges of the Møller detctors.*

3.5.2 Inelastic *ep* Scattering

A more challenging background correction is due to the smaller dilution from inelastic electron-proton scattering. Even though the contribution from the background is expected to be small, $\lesssim 0.5\%$, the asymmetry correction can be significantly larger due to the fact that the predicted coupling to the Z boson is more than an order of magnitude larger than Q_W^e. Indeed, this background was studied in E158 and the parity-violating asymmetry from inelastic electron-proton scattering was consistent with the formula $0.8 \times 10^{-4} \cdot Q^2(\mathrm{GeV})^{-2}$. At E158, the dominant systematic correction was indeed from this process: the average correction was 22 ppb, compared to the predicted electroweak Møller asymmetry of about 160 ppb.

For the configuration of the proposed measurement, we expect the fractional background to be smaller. This is because the inelastic cross-section stays roughly constant in the two cases (48 GeV vs 11 GeV) while the Møller cross-section is inversely proportional to the incident beam energy. Thus, the conservative estimate is that the correction will be at most 4% of the Møller asymmetry. We expect to be able to make the correction with an error less than 10% of itself. This is because we expect to be able to measure the parity-violating asymmetry in fine radial and azimuthal bins, which should provide a good handle on the variation of the parity-violating asymmetry in inelastic electron scattering as a function of the kinematic variables W and Q^2. We assign a systematic error of 0.4%. Figure 3.2 shows the radial distribution of inelastically scattered events in our most recent Monte Carlo simulations.

3.5.3 Hadrons and Muons

There is the possibility of pions and other hadrons to contribute at a small level to the signal in the Møller detectors. The polarization asymmetry of these pions depends on the processes that creates them. The most likely source of pions would come from real and virtual photoproduction off protons in the target. This background was studied for the E158 configuration and a conservative estimate $\lesssim 0.5\%$ was made. During the experiment, this was explicitly measured to be 0.12% in the Møller detector. The parity-violating asymmetry, measured in dedicated pion detectors that measured the hadronic leakage behind the Møller detector, was found to be ~ 0.5 ppm.

For the configuration of this proposal, we expect that the most conservative estimate is that the background fraction from pions is the same as in the E158 case. The Møller cross-section has gone up by a factor of 4, but the solid angle bite has

also gone up by about a factor of 4. In practice, fewer pions will be produced due to the fact that the beam energy is smaller, but we neglect that suppression factor here. Another potentially important factor might be whether the detectors at the main Møller peak are "shower max" detectors, so that the ratio of pion to electron signal is further suppressed. The asymmetry will likely be the same size, which would lead to a significant correction: ~ 0.5 ppb.

There is also a small probability of forward pions from deep inelastic scattering to enter the acceptance. A detailed study was carried out for the E158 case which we can ultimately replicate for the kinematics of the current proposal. These pions should be highly suppressed in the range of our kinematic acceptance. Nevertheless, the parity-violating asymmetry from such pions would be nearly 4 orders of magnitude larger and it would be quite challenging to prove through simulations that the contributions to A_{PV} are negligible. In a similar vein, there is also the possibility of a tiny fraction of muons or other hadrons from charged current processes, which would have a strong helicity dependence.

The above considerations lead to the conclusion that the hadronic leakage, both the flux and the polarization asymmetry, must be measured explicitly in the apparatus. We are indeed planning to do this as is discussed briefly in App. C.5. Based on the above considerations, our estimate for the pion asymmetry correction is 0.5 ppb and we assign a systematic error of 0.1 ppb to this correction.

3.5.4 Photons and Neutrons

In a forward spectrometer of the type being discussed for the proposal, it is very challenging to suppress neutral background from soft photons and neutrons. At E158, neutron background was heavily suppressed by burying the photodetectors in a lead shield and we will follow a similar strategy here. We have taken a preliminary look at the collimation system and we believe that we can greatly suppress photon background, designing a near-perfect "two-bounce" collimation system. There will be at most one or two edges from which photons could reach one of the primary detectors after undergoing only one bounce from the taget. The flux at these edges will be rather modest compared to the signal flux.

Further suppression can be achieved if necessary if the main Møller detector is made into a "shower max" detector. Based on previous experience and simulation, we anticipate suppressing this background at the level of a fraction of a percent and expect to make the correction with an error less than 0.1%. These backgrounds can be measured with special runs, such as by "blinding" the Cherenkov photodetectors and looking for the residual beam-correlated response. Such backgrounds are not

Error Source	Fractional Error (%)
Signal Statistics	2.08
Absolute value of Q^2	0.5
beam (second order)	0.4
beam polarization	0.4
$e + p(+\gamma) \rightarrow e + X(+\gamma)$	0.4
beam (first order)	0.3
$e + p(+\gamma) \rightarrow e + p(+\gamma)$	0.3
$\gamma^{(*)} + p \rightarrow \pi + X$	0.3
Transverse polarization	0.2
neutrals (soft photons, neutrons)	0.1
Total	1.02

Table 3.2: *Summary of projected experimental errors.*

expected to have any polarization asymmetry.

3.6 Summary of Systematic Errors

We summarize the considerations above and tabulate our estimates of the most important systematic errors in decreasing order of importance in Table 3.2. It is instructive to recall that the raw asymmetry is about 32 ppb and that the raw statistical error is 0.6 ppb or about 2%.

Chapter 4

Concluding Remarks

4.1 Collaboration

Our collaboration has extensive experience in the measurement of small, parity-violating asymmetries with proton and electron beams. In particular, we have brought together participants in the ongoing 3rd generation Jefferson Laboratory parity-violation program (Qweak [23] and PREx [22]), plus senior members of the completed E158 [1] program at SLAC. The experimental collaboration is still growing, and we hope to expand international involvement further. Theoretical support is provided by collaborators J. Erler and M. Ramsey-Musolf.

In the following paragraph, we list key subsystems and institutions who are interested in design, construction and implementation of them. Note that these are not firm or binding responsibilities, but simply the current thinking of the collaboration given each institution's current interests and previous experience. We have listed all the Canadian institutions (University of Northern British Columbia, University of Manitoba, University of Winnipeg and TRIUMF) as a group in this list and the detailed distribution of responsibilities among them will be determined later. As emphasized earlier, we expect the collaboration to expand should we receive PAC approval.

- Polarized source: UVa, JLab, Miss.St.
- Hydrogen Target: JLab, VaTech, Miss.St.
- Spectrometer: Canada, ANL, MIT, UMass, UVa
- Focal Plane Detectors: Syracuse, Canada, JLab

- Luminosity Monitors: VaTech, Ohio
- Pion Detectors: UMass/Smith, LATech
- Tracking Detectors: William & Mary, Canada, UMass/Smith
- Electronics: Canada, JLab
- Beamline Instrumentation: UMass, JLab,
- Polarimetry: UVa, Syracuse, JLab, CMU, ANL, Miss.St., Clermont-Ferrand
- Data Acquisition: Ohio, Rutgers
- Simulations: LATech, UMass/Smith, Berkeley

4.2 Synergy with the PVDIS Proposal

This measurement, at a level more than the Qweak and PREx measurements, will face significant challenges not only in the size of the asymmetry but also on the stringent requirements in terms of normalization errors such as the measurement of the beam polarization and the absolute value of Q^2. In these matters, we gain significantly also from overlap of collaborators with the PVDIS proposal. In particular, these two proposals will share the same beam line and the same beam polarization devices should they both be funded. The normalization errors are even more critical for the PVDIS proposal.

4.3 Beam Request

While it is too early to make a definitive beam request, we have pointed out that we need 30 weeks at a beam current of 85 μA to obtain our statistics goal. Some additional running will of course be needed to commission the experiment and also for systematic studies. This measurement is clearly a multi-year project in the Hall and detailed coordination will be needed to co-exist with other possible experiments in the Hall such as the PVDIS experiment discussed above.

It is also worth noting that the measurement discussed here will need running over at least two annual running cycles. In particular, such a challenging measurement would benefit a great deal from a first production run period with a fraction of the statistics. When it comes to making a beam time request, the possibility of obtaining an important intermediate result will be carefully taken in to account.

4.4 Cost and Schedule

We are beginning the exercise of coming up with preliminary cost estimates. It is clear that significant funds will be required from several agencies. We plan to seek funding from US DoE, NSF and Canada's NSERC. As emphasized in the introductory section, this project has been listed as part of the Fundamental Symmetries initiative in the NSAC Long Range Plan, and it has been included into the Plan's 10 year funding profile. The project has also been mentioned in the long range plan in Canada.

In terms of a project schedule, it is our goal to have funding requests to the major funding agencies by early 2010. Assuming we receive physics endorsement from the PAC, we would hope to be able to pass a technical review by the end of 2009. This timeline is necessary to start serious construction by 2012, which would give us a reasonable chance, given an appropriate funding profile, to be ready for installation in 2015.

Appendix A

Polarized Beam

A.1 Polarized Electron Source

Laser light illuminates a semiconducting photocathode, the surface of which has been chemically treated to produce a negative work function, refered to as a negative electron affinity (NEA) surface. The laser light wavelength is tuned to promote electrons from a specific valence band to the conduction band of the semi-conductor. The photocathode is held at a negative potential, so as the electrons from the conduction band exit the cathode they are accelerated into the injector beamline.

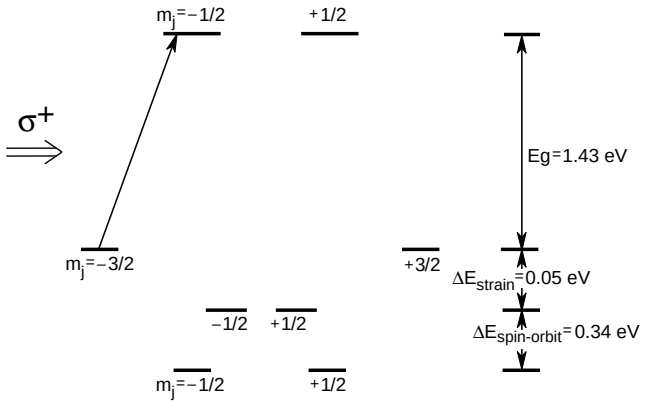

Figure A.1: *Band structure of GaAs, showing how circularly polarized laser light produces polarized electrons.*

Through doping or other stress applied to the photocathode, the degeneracy

in the spin-orbit states of the specific valence band are split, as shown in Fig. A.1. For circularly polarized light, the spin-1 photon is restricted to exclusively promote electrons to a single spin state. This process produces an electron beam polarization of nearly 100%, however, some depolarization occurs in the diffusion of the liberated electrons to the photoconductor surface. The CEBAF polarized source now routinely provides $\tilde{8}5\%$ polarization with up to a few hundred μA beam current.

Since the electron polarization is fully determined by the circular polarization of the incident laser light, it is possible to rapidly flip the helicity of the electron beam by changing the laser polarization. This is accomplished using an electro-optic Pockels cell, acting as a quarter-wave plate to produce circularly polarized light from the initial linear polarization. A reversal of the applied voltage on the Pockels cell reverses the circular polarization of the laser light, and thus the helicity of the electron beam. A schematic diagram of the experimental configuration is show in Fig. A.2.

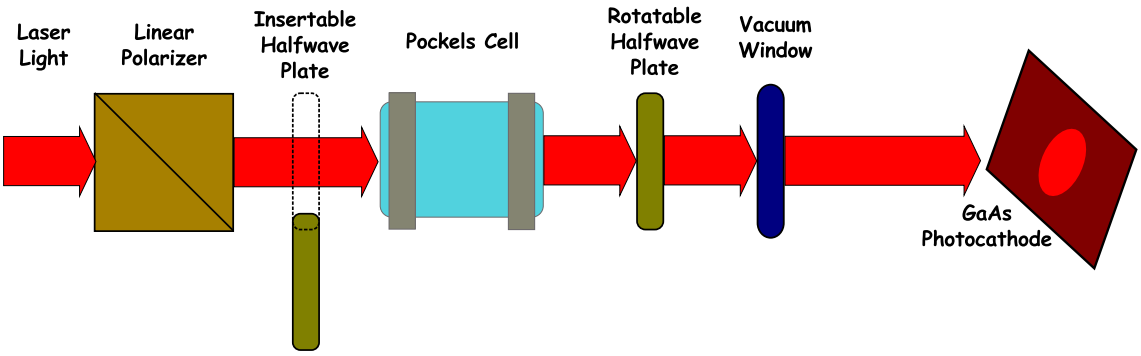

Figure A.2: *Schematic of the laser transport line that allows for rapid reversal of the electron beam polarization.*

A.2 Operational Experience

There is significant operational experience in using the polarized electron source for parity-violation experiments at Jefferson Lab [25]. One challenge of these experiments is that changes in the beam properties (intensity, position, profile) will change the detected scattered flux. If the changes in the beam are correlated with the electron helicity, the result can mimic the tiny parity-violating asymmetry. While

changes are typically measured and corrections are applied, the corrections are typically made with precision of around 10%. Helicity-correlated beam asymmetries (HCBAs) are therefore a potential systematic error in the measurement of small asymmetries, and a very high level of control of HCBAs is required for the precision measurement contemplated here.

A sophisticated understanding of the sources of HCBAs at JLab has been achieved. The HAPPEX-II experiment, which ran in Hall A in 2005, made use of this improved understanding to achieve run-averaged helicity-correlated position differences, measured in the experimental hall, which were consistent with zero systematic offset with uncertainties of < 2 nm and 0.2 nanoradian in angle (see Fig. A.3).

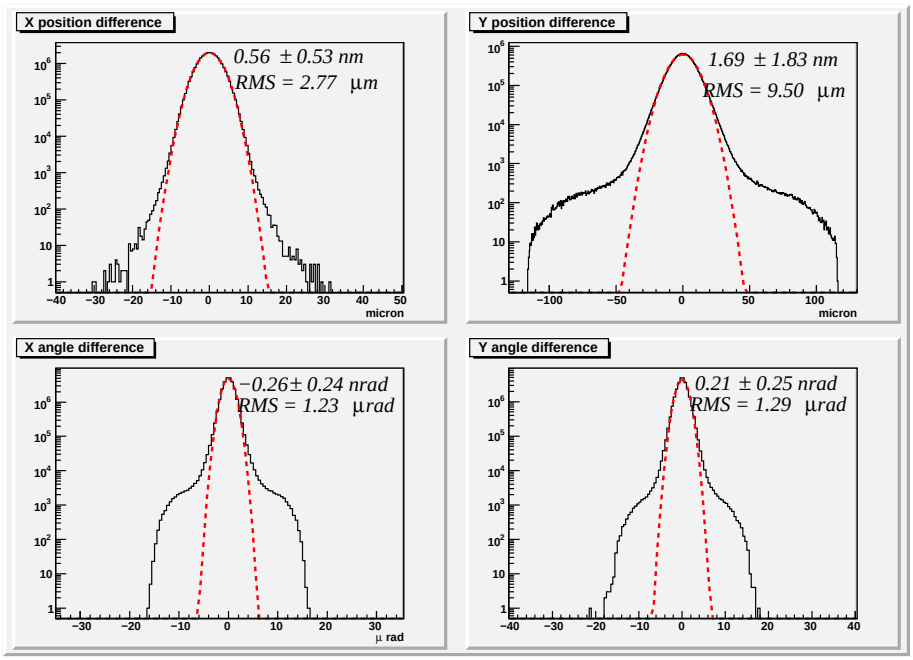

Figure A.3: *Beam position and differences, plotted for all* 27×10^6 *pairs of the HAPPEX-II analysis. Arithmetic means, widths, and centroid uncertainty due to random noise are shown. The systematic correlation to helicity was measured to be consistent with zero within the random beam noise. Gaussian fits are included for reference.*

The PREX experiment, to run in Hall A in early 2010, and the QWeak experiment, which will start in Hall C in mid-2010, have precision goals which are approximately an order of magnitude better than what has been previously achieved. The

PREX experiment aims to keep helicity correlated beam motion to < 1 nm (as was accomplished for HAPPEX-II) and to bound the beam spot difference to $< 10^{-4}$ of the intrinsic beam size. The ongoing research on the polarized soure for these experiments will provide important experience to accomplish the systematic goals for the proposal under discussion.

A.3 Adiabatic Damping

The impact of helicity-correlated spatial variation in the beam is greatly reduced in the accelerated beam impinging on the target due to the process of adiabatic damping. A simple consequence of relativistic mechanics is that the available phase space for a beam which has been adiabatically accelerated to a momentum p from a momentum p_0 is reduced by a factor of p/p_0. For the 3 GeV beam energy of the HAPPEX-II experiment, this corresponds to a reduction in beam motion in each dimension by a factor of ~ 95, compared to motion of the 100 keV injector beam.

The benefits of this effect are typically not fully realized; getting close to the theoretical limit requires detailed understanding of accelerator beam optics, tuning and diagnostics. The collaboration typically works closely with accelerator physicists to produce the best results and maintain them over the duration of data collection. The best performance from the HAPPEX-II experiment suggested that helicity-correlated variations were suppressed by factors up to ~ 30.

The benefits from adiabatic damping have lagged behind the theoretical maximum in part due to difficulties in configuring the 100 keV injector region. Additional diagnostics and optics in that portion of the injector would presumably allow greater benefits to be realized. Such work, in addition to other, already implemented, additions to diagnostics and control, should make it possible to realize a significant fraction of the theoretically maximum of supression factor of 180 for the case of a 11 GeV beam.

A.4 Slow reversals

The technique of "slow helicity reversal" generally refers to the introduction of an additional helicity flip, which changes the sign of the helicity relative to some sources of HCBA. An example would be the introduction of an additional half-cycle $g-2$ rotation, which would reverse the electron beam helicity with respect to the helicity of the beam created in the polarized source. The statistical consistency of data

sets taken in different states of the reversal can be used to demonstrate the absence of large, unknown systematic errors, and the combination of data sets (appropriately sign-corrected) provides a method for further canceling possible unmeasured or poorly-corrected HCBA effects.

At present, only one slow-reversal is commonly employed at CEBAF. A half-wave plate is inserted into the laser path to reverse the sign of laser polarization, relative to the voltage applied to the Pockels cell (see Fig. A.2). This slow-reversal is particulary effective for cancelling effects related to electrical and electronic signals, either from the logic or Pockels cell high voltage, which correlate to helicity. As a general rule, the HCBAs related to residual linear polarization, which are typically the dominant effects, also change sign along with the beam helicity under waveplate insertion. For this reason, other methods of slow-helicity reversal are desirable.

At 11 GeV, the total number of $g-2$ spin rotations will be large, on the order of 120π. It will be possible to change the orientation of spin, while maintaining very similar beam optics properties, by changing the energy of the accelerator by about 100 MeV. This interval is small enough to not require invasive reconfiguration of the experiment: backgrounds, spectrometer optics, etc. should remain very similar. This would be a very effective slow reversal, in that all HCBAs from the source should influence the final measurement with the opposite sign. Since this is disruptive to other halls, this method might be used a few times over the duration of the entire run.

A similarly effective slow reversal that can be used much more often can be created using spin manipulation in the injector. Spin manipulation (so-called Wien rotator) is necessary in the CEBAF source to align the electron polarization into the horizontal plane, and then to set the in-plane launch angle to optimize longitudinal polarization at the experimental target. In principle, it is possible to apply a half-cycle spin rotation without changing the optics of the beam. In practice, this will require a more complicated spin manipulation in the CEBAF injector than is presently in place. Plans for the PREX and QWeak experiments are to install a second Wein rotator and solenoid, along with other beamline changes, which will allow a helicity slow reversal using solenoidal spin manipulation without changes to the Wien rotator setpoints or other significant changes to the beam optics.

A.5 Requirements for 11 GeV

A.5.1 Rapid Helicity Flip

Previous parity-violation experiments at Jefferson Lab have used a rapid helicity reversal frequency of 30 Hz, which had the benefit of largely cancelling beam jitter and electronics noise related to 60 Hz line noise. It will be necessary for future experiments to flip the helicity much more quickly, in large part because it is expected that density flucuations in the high-power cryotarget are limited to frequencies below a few hundred Hz. This proposal is designing around a flip rate of at least 2 kHz, which implies that each helicity state is held for 500 microseconds. The goal is to flip the Pockels cell within 10 μs, which implies a dead-time of 2%.

At present, it appears that reducing the settling time to 50 μs is achievable for reversal rates of 250 Hertz. Additional development will be required for faster flip rates; there appears to be no apparent fundamental problem that will prevent settle times of 10 μsec or flip rates of 2 kHz. In order to avoid excess noise from 60 Hz line variations, a scheme for selecting helicity states will be required which will force complementary pairs at corresponding points in the 60 Hz cycle.

A.5.2 Measurement and Control of HCBAs

Monte Carlo simulation was used to estimate the sensitivity of the apparatus to beam motion. With the minimum acceptance angle defined by collimators placed 10 meters downstream of the target center, the detected flux in one azimuthal segment is expected to change by approximately 8.5 ppb for a 1 nm shift in the beam centroid. The results conform to simple scaling arguments from sensitivities measured during HAPPEX-II. This suggests the approximate sensitivity to changes in the beam angle, as well: 85 ppb/nanoradian. The ratio of these sensitivities roughly matches the accelerator which, as a rule of thumb, has a characteristic length of about 10 meters.

The goal in any measurement of a small asymmetry is to keep the cumulative correction averaged over the entire run due to random or helicity-correlated beam motion to be no larger than the grand statistical error, and to believe the correction to 10% of itself. An important benchmark to keep in mind is that the the width of the helicity-correlated asymmetry distribution of a single azimuthal detector segment will be around 190 ppm for the 1 kHz pairs. This corresponds to 23 ppm for the 15 Hz bunches. For the full detector, the corresponding numbers are 77 ppm and 8.7 ppm respectively.

Assuming that one can make the conservative assumption that one can gain a factor of 10 in suppression in sensitivity by averaging over azimuthal segments due to the symmetry of the apparatus, this implies:

- The beam centroid must be measured at two locations 10 m apart just upstream of the target with a resolution of a few microns at 1 kHz
- The beam centroid and angle jitter must less than 10 microns and 1 microradian respectively at 15 Hz
- If the beam jitter is significantly larger than quoted above, active position feedback on the electron beam at 1 kHz frequency will be necessary.
- The grand-average helicity-correlated position difference over the duration of the entire run must be less than 0.5 nm and the angle difference should be less than 0.05 nrad.

We elaborate on these issues below. The experience of HAPPEX-II, which found position (angle) differences of around 1 nm (0.2 nrad) suggests that these specifications should be achievable.

A.5.3 Beam jitter and monitor resolution

The typical resolution measured from the standard "stripline" beam position monitor (BPM) is around 2 micron at 15 Hz. This resolution would nearly double the width of a single azimuthal segment, as with the introduction of an additional contribution of 17 ppm random noise in the beam position correction. The distance between BPMs also becomes a crucial parameter for determination of the beam angle difference correction; With 10 meters between BPMs each with a resolution of 2 micron, the angle sensitivity introduces an addition source of about 24 ppm noise. In combination, this random noise dominate the statistical noise in the single detector measurement, which would significantly complicate studies of beam corrections for the system. While the noise should be reduced by a factor of 10 when averaged over the full azimuthally-symmetric detector, the combined contribution would be an excess noise of around 5%. New RF cavity BPMs have been built for the upcoming PREX and Qweak runs, although their ultimate resolution has not yet been determined. Ultimately, a factor of 10 improvement in resolution over the stripline BPMs will be required for this high precision measurement. The location of

the BPMs in the beamline design may also be important. Performing beam corrections with BPMs located at points of large beta functions may enhance the monitor sensitivity to orbit changes, thereby reducing the requirement for BPM resolution.

Even with a large improvement in BPM resolution, it will be difficult to determine the beam position correction sensitivities with better than around 10% precision, which implies that beam position jitter could become a signficant source of random noise. The typical rms width of the helicity-pair position difference during HAPPEX-II was between 3-10 micron at 15 Hz, which would imply corrections of up to 90 ppm and additional noise at the level of 9 ppm in each single detector. If the beam jitter is significantly larger than this expectation, then the resolution of this correction will introduce excess noise in the full detector signal.

A.5.4 Position Feedback

A more significant problem might be the slow convergence of the random beam jitter. Even with no systematic helicity-correlated offset, beam jitter of 5 micron would converge to zero with a 1σ range of 0.8 nm.

A systematic non-zero helicity-correlated position difference could be diagnosed more quickly, and the potential loss of statistical precision could be mitigated, by forcing the random jitter to converge through feedback. This feedback would necessarily be helicity-correlated, and operate with a time-scale between a few minutes and a few hours. The optimized feedback time-scale will depend on the safe dynamic range of the feedback system, the time scale of any slow-reversal or other significant beam disturbance, and the magnitude of the jitter, among other factors.

The goal of any such feedback would be to improve on the statistical rate of convergence for the beam position jitter by a relatively small amount. Under optimal feedback, the centroid would converge to zero as $1/N$, where N is the number of integration periods of the feedback cycle, compared to $1/\sqrt{N}$ for the case without feedback. A balance will need to be found between keeping the average feedback correction small, while still operating on a time scale that drives convergence to zero position difference. Updating feedback every hour, for instance would improve convergence by a factor of $\sqrt{8}$ on an ideal shift, while implying that the size of the correction would be around 4×10^{-3} of the beam jitter.

It is important not to mask serious configuration problems in the polarized source with the use of intensity and position feedback systems. For this reason, the average position correction will be monitored for significant non-zero average corrections which indicate the need to re-tuning of the polarized source. It is also crucial that any position dependent feedback does not change intensity asymmetries

in a way which reduces the rate of convergence of the crucial intensity feedback.

There are several mechanisms which could be used for position feedback. The commonly employed technique at Jefferson Lab, successfully employed by the G0 collaboration, uses a piezoelectric actuated mirror in the source optics to deflect the laser beam. Similar techniques were employed or tested by the E158 collaboration at SLAC and the SAMPLE collaboration at Bates.

Since the dominant source of position differences is a non-zero first moment in the helicity-dependent residual linear polarization distribution of the laser spot, a superior feedback mechanism might involve a birefringent element with a variable, linear variation of birefringence across the beamspot. Such a device could be conceptually similar to the continuously variable birefringent system, such as the Babinet-Soleil compensator.

There are several disadvantages to position feedback mechanisms which operate on the source laser. The most important is that the photocathode changes significantly on the time-scale of days. Ion back-bombardment damages the photocathode, creating a quantum efficiency "hole" at the laser spot and along a path to the electrical center of the cathode. Motion of the beamspot on the cathode can interact significantly with these strong QE gradients, changing the effective slope of the correction and creating significant coupling with electron beam intensity.

These complications can be avoided by using magnetic deflection of the electron beam. A system of 4 air-core magnetics has been constructed in the injector, with a fully isolated power and control system. These were constructed by the Electron Gun Group as a potential feedback mechanism. As expected, this system avoids the significant coupling to beam intensity which complicates use of the piezoelectric mirror. Further testing would be required to qualify this system at the required level of precision, and at the 2 kHz reversal frequency.

A.5.5 Beam spot-size asymmetry

Geometric arguments predict that the sensivity to a spot size asymmetry $\delta\sigma/\sigma$ is approximately (12 ppm)$\delta\sigma/\sigma$. An upper bound on the spot size asymmetry should be possible from measurements on the laser table of $\frac{\delta\sigma}{\sigma} < 1 \times 10^{-4}$, which would imply a net false asymmetry of about twice the statistical error bar over the course of the run. Spin precision spin flips, including both the $g-2$ and spin-manipulator slow reversals, will both serve to flip the helicity without changing the spot size asymmetry, and should provide a high degree of cancellation. Assuming roughly equal statistics are collected in each reversal state, the average effect from spot size should be reduced by a factor of 10.

A.6 Strategy for control of HCBA

As described above, modest improvements on the state-of-the-art are necessary to achieve sufficent control on the run-averaged helicity-correlated beam asymmetries. A summary of the strategy is presented here.

The intensity asymmetry requires control at the level of < 10 ppb. As with previous experiments, an automated helicity-correlated feedback on beam intensity will be required to achieve this small value. There does not appear to be any fundamental reason why the conventional asymmetry feedback scheme should not converge to this level. While this is approximately an order of magnitude beyond what will be required for the PREX and Qweak experiments, those runs will provide an opportunity to demonstrate feedback effiency at the required level.

Control of position differences will require careful configuration of the source optics. As is currently done, the optics system will be qualified first with diagnostics on the laser table, and then with measurements of HCBA in the electron beam in the low-energy injector. It is estimated that improvements in the injector measurements are feasible which would enable precision scans of important configuration parameters leading to the verification of injector position differences approaching ~ 20nm. As is required for the PREX experiment, the potential spot size asymmetry will also be bounded in laser table studies at the level of 10^{-4}, which limits the potential effect on the measurment at the level of 1 ppb.

Good optical transport throughout the injector and accelerator is crucial to realizing the benefits of the adiabatic phase space damping. It should be possible to achieve a damping factor approaching 100 (about half of the theoretical maximum) if further improvements in injector diagnostics are made. In combination with a source configuation giving position differences in the injector at the level of 20 nm, the average systematic helicity-correlated offset would lie in the 0.2 nm (0.02 nrad) range, sufficient for this measurement.

If the careful beam preparation succeeds at this level, the dominant source of helicity-correlated beam position difference would be the slow convergence of the random (non-helicity-correlated) beam motion. For this reason, it may be necessary to employ feedback on position differences. The feedback integration period would be long enough to allow small corrections to position differences, which are not likely to interfere with other aspects of beam preparation or delivery. The magnitude of feedback corrections will be monitored for signs of a required reconfiguration of the polarized source.

Several slow reversals will be employed. The insertable halfwave-plate in the source optics will be used frequently, possibly changed at 4-12 hour intervals. A

frequent spin-manipulation slow reversal is required to cancel spot size asymmetries, so the injector solenoid slow reversal should be used on a period of approximately 1 week. The $g-2$ energy change spin flip, should be used at least once, dividing the full data set in two. Although it is potentially more disruptive, it is also expected to be the most effective of the slow reversals, and the experiment would benefit from using it as often as once per month.

Appendix B

Toroidal Spectrometer

We have already listed the salient features of the spectrometer system in Sec. 2.4. Figure B.1 shows a three dimensional realisation of the current spectrometer design. Here we provide more details of the spectrometer design.

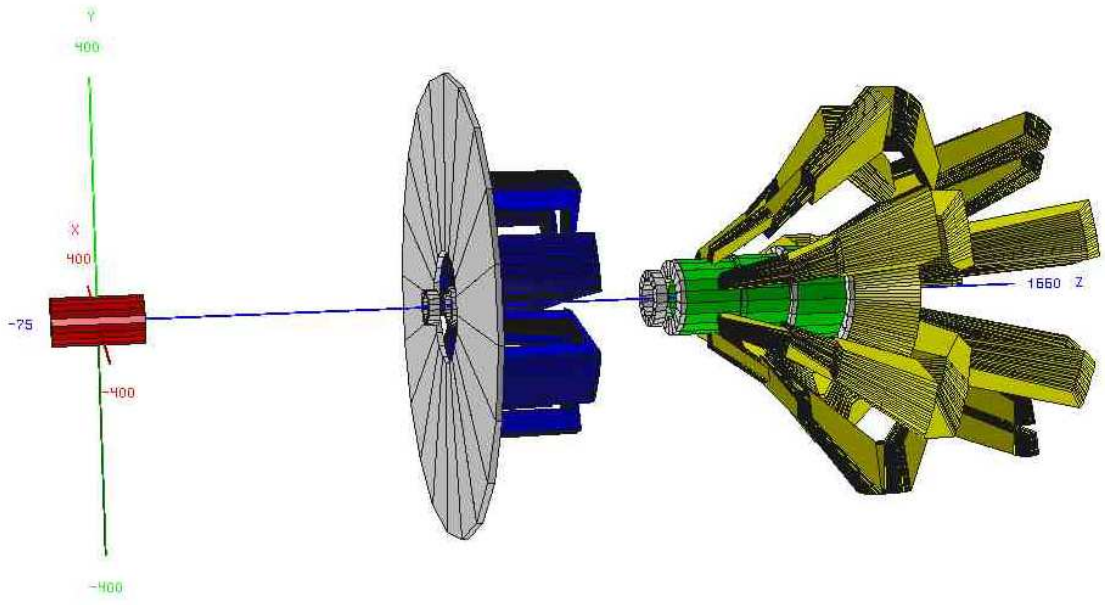

Figure B.1: *Three dimensional drawing of the spectrometer setup including the target (red), front (blue) and hybrid (yellow) toroid magnets and collimation surfaces (grey). The actual detectors are not plotted.*

B.1 Kinematics

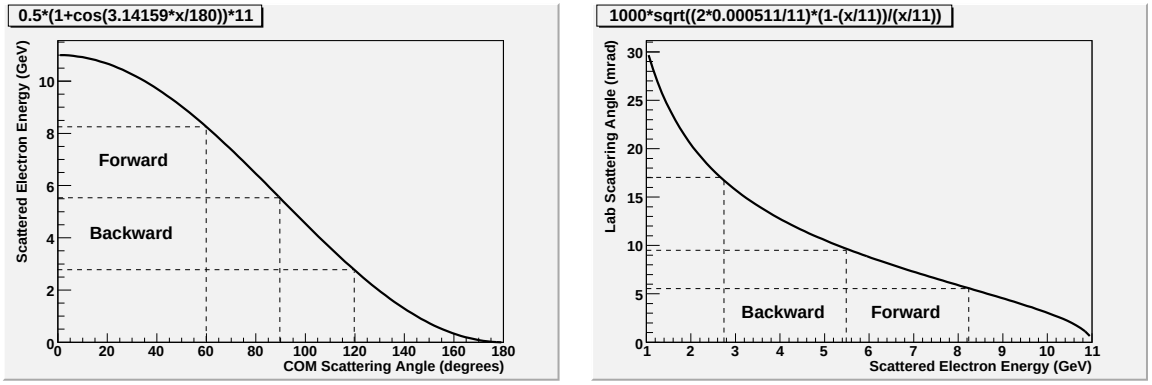

Figure B.2: *COM scattering angle vs scattered electron energy in the laboratory frame for an incident beam energy of 11 GeV is shown on the left. On the right is shown the scattered electron energy vs scattering angle in the laboratory frame.*

An important strategy in the design of the spectrometer is to maximize acceptance for Møller scattering events that have the largest analyzing power. In the COM frame, the maximum asymmetry, the minimum differential cross-section and the maximum figure of merit (FOM) occurs at a scattering angle of 90°. If the scattering angle is less than 90°, these are called "forward" Møllers and those with angle greater than 90° are called backward Møllers.

A nice feature of Møller scattering is the energy-angle correlation: there is a one-to-one correspondence between a COM scattering angle and the scattered electron energy in the laboratory frame. This is depicted on the left of Fig. B.2. In order to gain rate and accumulate statistics efficiently, it is required to accept a significant fraction of forward and backward Møllers, preferably from 60 to 120 degrees, which implies that one must accept scattered electrons over a wide range of energies.

The energy-angle correlation also implies that there is a one-to-one correspondence between the scattered electron energy and the scattering angle in the laboratory frame. This is depicted on the right of Fig. B.2. Thus, the laboratory scattering angle range and the energy range respectively for forward Møllers are 5.5 to 9.5 mrad and 5.5 to 8.25 GeV and the corresponding ranges for backward Møllers are 9.5 to 17 mrad and 2.75 to 5.5 GeV.

B.2 Maximum Azimuthal Acceptance

A principal challenge in the design is to accept scattered electrons over the full range of the azimuth to maximize the rate. There is an interesting feature of the event topology due the fact that one is dealing with identical particle scattering. Each forward Møller has a corresponding partner in the backward direction which represents the same event. Thus, one can obtain 100% acceptance over the full range of the azimuth in two ways. One way is to accept all scattered particles in the 9.5 to 17 mrad range over the full range of the azimuth. However, this precludes the use of toroids; one needs to cut into the azimuthal acceptance to place the coils.

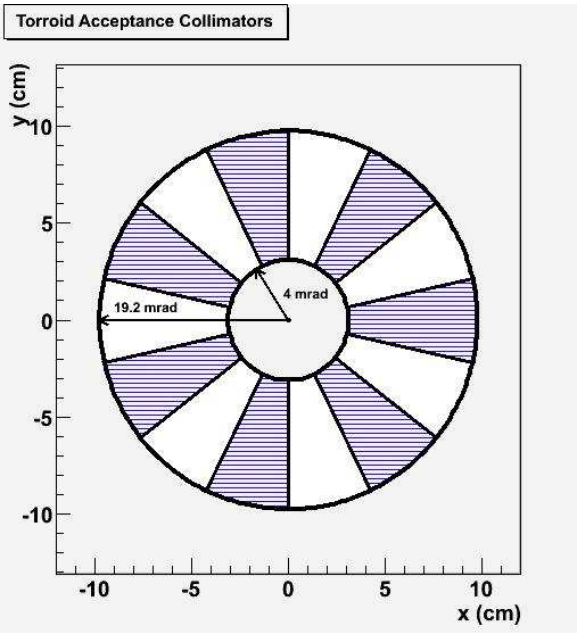

Figure B.3: *Primary collimator geometry for the proposed toroidal spectrometer.*

We have found a way to get 100% azimuthal acceptance with a toroidal geometry which is specific to identical particle scattering. This is depicted in Fig. B.3, which shows the primary acceptance collimator situated 6 meters from the target. The idea is to accept both forward and backward Møllers in a specific phi bite, by accepting particles between 5.5 and 17 mrad. Since we are dealing with identical particles, those that are accepted in this phi bite also represent all the statistics available in the phi bite that is diametrically opposed (180° away in phi). In the

figure, each clear phi bite is diametrically opposed by a shaded region, which would be shielded from the target and can be used to house magnet coils without any loss of acceptance. In principle, any odd number of coils would work; in the following, we describe our current design which contains 7 coils.

B.3 Realization

The action of the spectrometer can conceptually be divided into a radial and an azimuthal part. In the radial dimension, the successful interaction of the two magnets is key. In the first magent, as is usual with magnets, tracks are separated according to momentum. The total $Bd\ell$ of this magnet is small and thus the effect on the high energy, low angle Mollers is small. The important part is that the the lowest energy, highest angle Moller electrons are bent even further away from the beamline. This allows these particles to skirt the strongest field in the second magnet.

The hybrid toroid is in some sense the heart of the spectrometer concept. It is designed so that particles at different radial distance from the beam feel *very* different integral $Bd\ell$. This allows the hard, low angle Mollers to be bent strongly to the radial focal position while the soft, high angle particles are merely 'tickled' into place. This concept can best be seen in Figure B.4.

In the azimuthal dimension, the first magnet has another important role. As can be seen in Figure B.5, the higher energy Moller electrons are bent towards the middle of the open segment. They are given a trajectory that does not significantly diverge in azimuth so that they arrive at the hybrid toroid, and traverse the full almost 7 m of field, within the centre of the open segment - far from the coils themselves. They then continue, still without much azimuthal divergence to the detector plane.

On the other hand, the lower energy electrons are strongly defocussed by radial fields in the hybrid toroid and bend around into the regions behind the blocked portions of the collimator. By the time the electrons reach the detector plane 28.5 meters from the target, the full range of azimuthal angles is populated by Møller electrons.

The effect of this behaviour is that the energy distribution of detected electrons changes along the azimuth. By segmenting the detector azimuthally, it is to a certain extent posssible to separate the detected electrons in energy or other quantities. This separation is a distinct advantage in terms of understanding the detector and eliminating backgrounds.

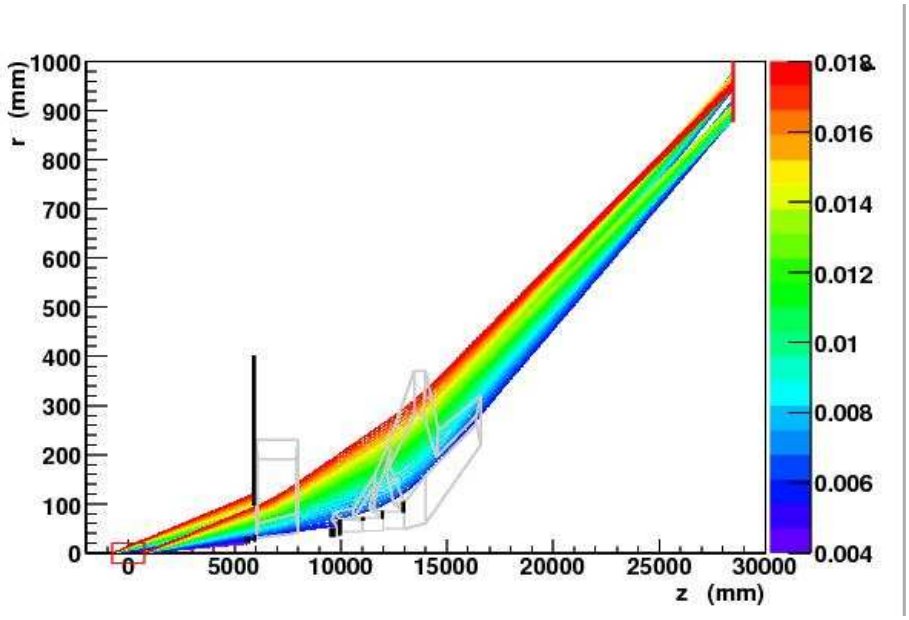

Figure B.4: *Plot of Moller electron transport through the spectrometer projected onto the radial coordinate. The color scale represents the initial angle θ_{lab} in milliradians. The spectrometer coils (grey) and collimators (black) are overlaid.*

B.4 Hybrid Toroid

The shape of the hybrid toroid is designed to provide a large range of total $Bd\ell$ correlated to the angle of the track. The design evolved under the imperative of maintaining a large current in a small volume near the beam line (due to the lowest angle tracks). Optimization is still ongoing and at this point, the specification is somewhat rough. However, it conforms to the basic requirements of managable current density and sufficient tolerances for water flow and support structure. The design concept is robust under small changes in geometry, and the performance will not significantly degrade as the concept evolves to accommodate winding schemes or realistic bend radii. The magnetic optics of the design are also not yet fully optimzed, so there is still hope of further improvement.

There are four primary features to this magnet:

- In order to maintain sufficient current at realizable density, the magnet fully encloses the beamline from z=10 meters to z=13 meters.

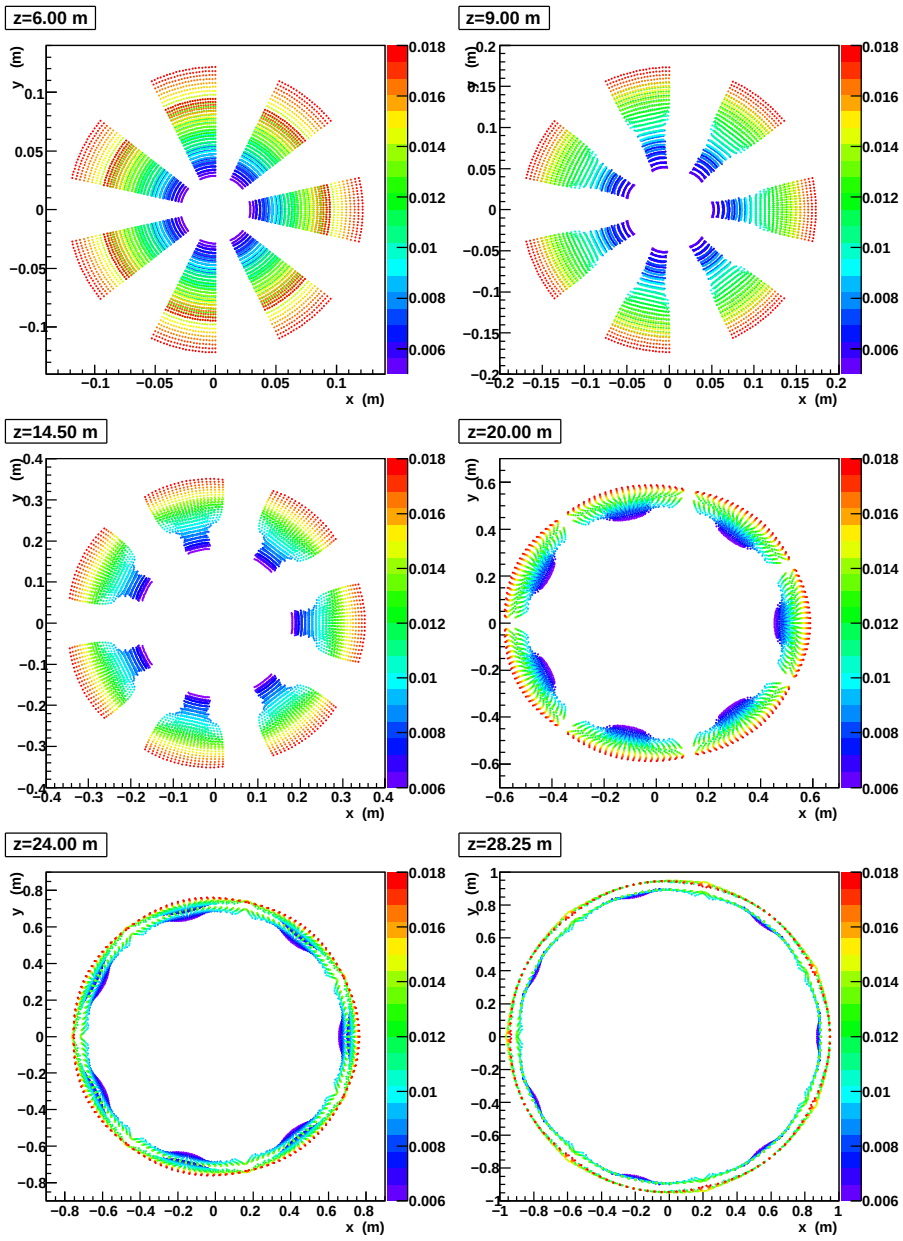

Figure B.5: *Plot of Moller electron transport through the spectrometer at various distances downstream of the target center. Details as in Figure B.5.*

- The current in the magnet grows along that distance from z=10 m to z=13 m, with current returning in 4 different vertical limbs, spaced along the beamline by about 1 m.
- the back-end of the magnet, with the highest current, juts out to keep the highest-energy Moller-scattered tracks in high field for a longer time.
- the top of the coil is dropping, over the radial range of accepted flux, so that some tracks receive less $Bd\ell$ by entering the field region comparatively late, or leaving it comparatively early.

Each of the 7 coils carries around 29 kA, and the total power consumption is estimated to be about 600 kW.

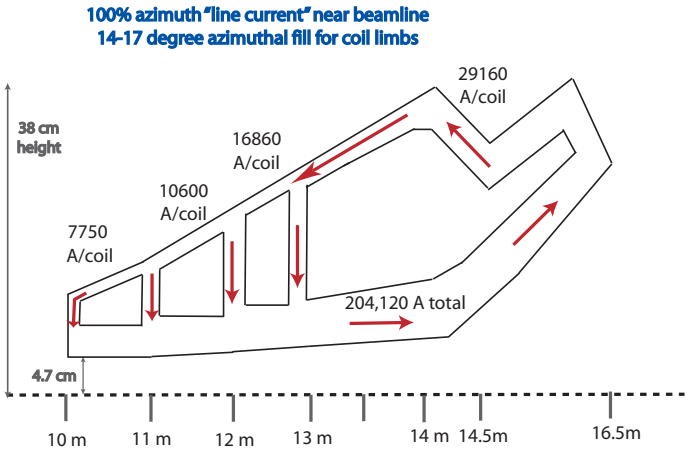

Figure B.6: *Schematic of the hybrid toroid design concept.*

B.5 Detector Simulation

The simulation of the performance of the toroidal spectrometer concept was done using the Geant4 framework [29]. The detection plane was chosen to be 28.5 m downstream of the center of the target since this is where the Møller electrons have their tightest radial focus. At this position the *ep* elastic (Mott) peak and the peak due to Møller electrons are separated by more than 20 cm. We have already talked about the radial distributions of scattered electrons from Møller, elastic e-p and

inelastic e-p scattering in Sec. 3.5.1, as shown Figure 3.2. The background is the result of initial and final state radiation in the target.

The anticipated position of the Møller electron detector is a ring with inner radius 0.88 m and outer radius 1.00 m, also shown in Fig. 3.2. The integral of the expected rate within this region is 154 GHz for the Møller electrons and 12.6 GHz for the Mott electrons - a background of 7.6%. If the calorimeter is a "shower max." detector, then the background would be 8.3% due to the slightly higher average energy of the background electrons. Figure B.7 shows the Q^2 distribution of the background from elastic e-p scattering that is accepted by the detector; this distribution is relevant for estimating the size of the background correction.

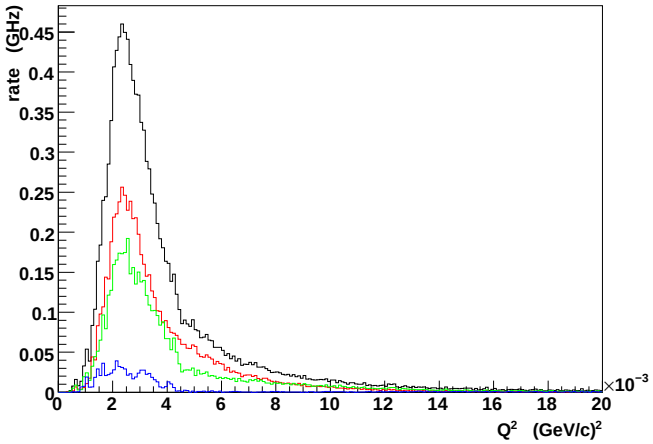

Figure B.7: *Rate of Mott electrons detected as function of Q^2, the square of the four momentum transfered in the scattering. Color convention from Fig. B.8.*

The detector ring is divided into 28 detectors of equal size (specifically azimuthal angle), which corresponds to 4 detectors per segment. These are arranged symmetrically, with one at the centre of the open part, one at the centre of the closed part and two which straddle the region between the open and closed part.

B.6 Møller Electrons

Figure B.8 shows the position of the Møller electrons in the z=28.5 m plane in radial coordinates. Here we establish the color convention which will be used in future plots

- red for the detector in the center of the open sector, blue for the detector in the centre of the closed sector and green for the detector which straddles the open and closed sector.

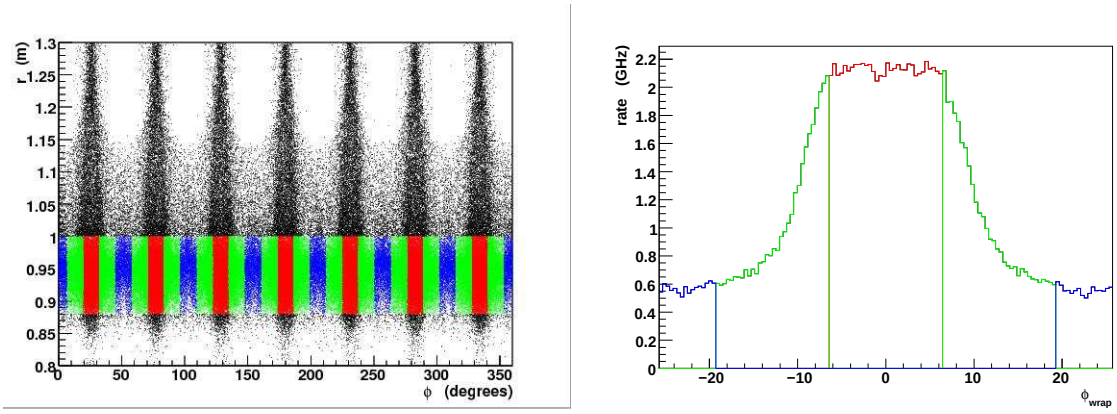

Figure B.8: *Møller electrons in the z=28.5 m plane in radial coordinates. The detected particles are colored according to which detector they hit, red for the detector in the center of the open sector, blue for the detector in the centre of the closed sector and green for the detector which straddles the open and closed sector. On the right is the rate of Møller electrons detected as function of ϕ_{wrap}, the azimuthal angle from the centre of the nearest open segment.*

For quantities that are azimuthally symmetric, the various detectors of the same "color" will have the same distribution and for the purpose of the following plots are combined. Figure B.8 shows the distribution on the right, plotted as expected rate at 85 μA beam current, of Møller electrons as a function of ϕ_{wrap}, the azimuthal angle from the centre of the nearest open segment.

Figure B.9 shows two distributions of Møller electrons that hit the main detectors. One can see that the "red" detector contains mostly forward Møllers, the "blue" detector is mostly backward Møllers and green has a mixture of both. The numbers relevant for estimating detector rates and predictions for asymmetries are listed in Table 2.1.

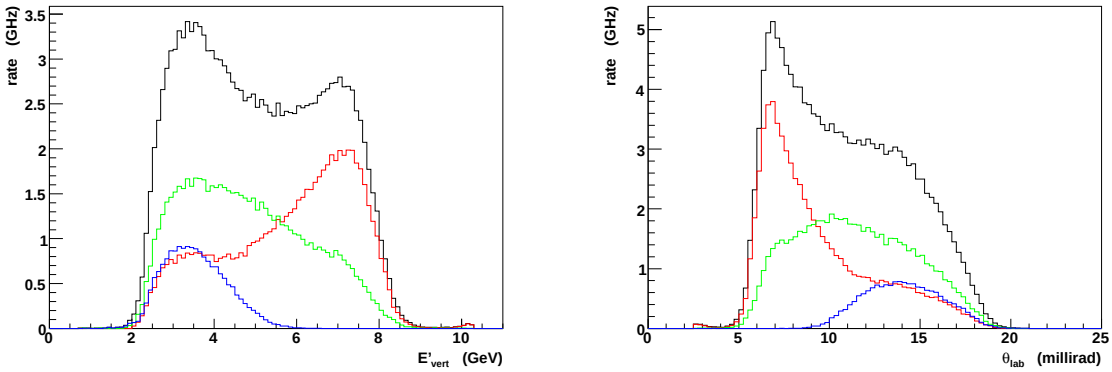

Figure B.9: *Rate of Møller electrons as a function of $\theta_{c.m.}$, the scattering angle in the centre of mass frame (right), and E'_{ver}, the energy of the scattered electron immediately after the interaction (left). Color convention from Fig. B.8.*

Appendix C

Main Detector

We have discussed the requirements of the detector systems in Sec. 2.5 In the following sections, we describe the conceptual designs for various detectors and discuss details.

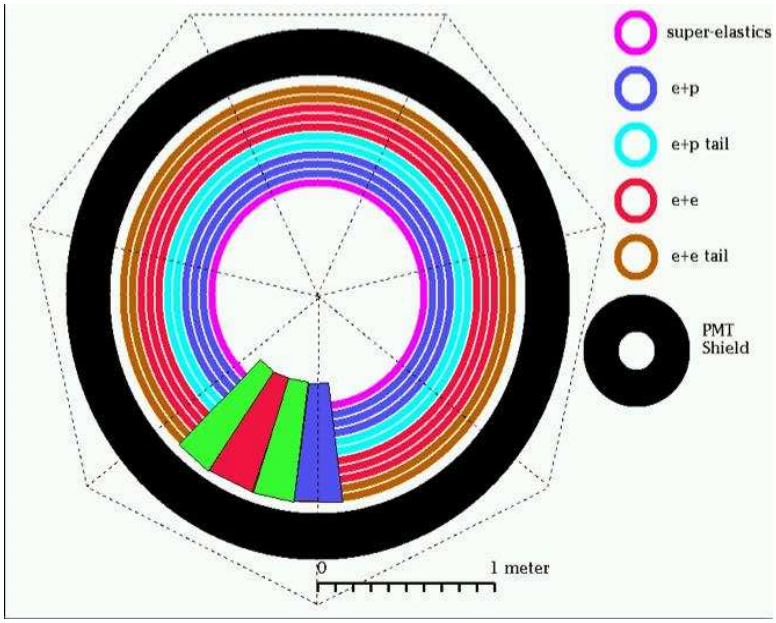

Figure C.1: *View of the detector, looking downstream, which shows the radial binning (rings) and in one sector, the azimuthal binning.*

C.1 Detector Design

The detector is based on Cerenkov light production in radiators of artificial, fused silica. These radiators are 5 cm wide in the radial direction, and 1-2 cm thick in the beam direction which Qweak simulations suggest is close to optimal [30]. Figure C.1 shows a front view in which all the Moeller electrons in the acceptance would be focused on the three red rings. Cerenkov photons undergo total internal reflection, escape from the outer radius of the radiator, then travel down an air lightguide [31] and are collected by phototubes behind a Lead shielding doughnut. Radial and azimuthal segmentation of the detector allows us to integrate the $e + e \rightarrow e + e$ signal, measure the backgrounds, and check that the yield and asymmetry have the expected variation with radius and azimuthal angle. The fact that the active element is a thin radiator means the detector response is essentially independent of incident electron energy and insensitive to neutral backgrounds. However, it will be equally sensitive to electrons and the small background of charged pions, so the latter need to be measured with ancillary detectors as briefly discussed below.

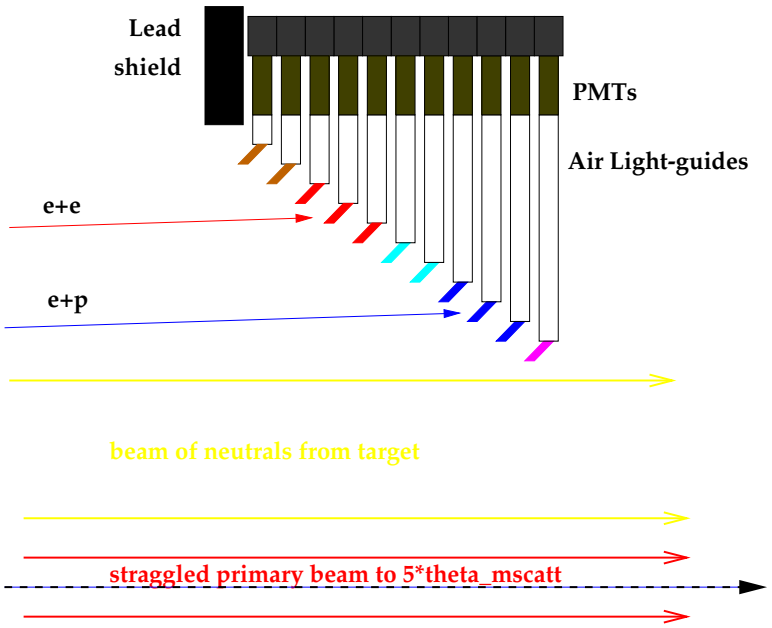

Figure C.2: *Detector side-view, showing the offset location of the radiators. The dimensions of the straggled primary beam (to* $5 \times \theta_{mscatt}$*) are shown, as well as the location of the beam of* γ*'s and n's from the target which shine through the collimator.*

Because of some residual azimuthal defocusing by the toroidal spectrometer, there is significant correlation between Q^2 and azimuthal angle. Therefore, we have divided each radial bin azimuthally into a central slice which detects events at low Q^2, a slice behind the coil which detects events at high Q^2, and two slices at intermediate Q^2. The total number of azimuthal bins is then 7 sectors x 4 bins/sector = 28, each bin covering approximately 12.9°. Presently, we plan to slightly overlap adjacent radiators to avoid missing tracks; double-counting causes a negligible increase in the statistical error.

As can be seen in the side view in Figure C.2, the offset location of the radiators provides room for the air lightguides while the upstream siting of the $e+e$ radiators minimizes contamination of the signal bins with showering from the higher asymmetry $e+p$ radiators. The phototubes will have UV glass windows and low-resistivity cathodes in order to provide high (nA-scale) currents while maintaining the cathode surface at an equipotential. The artificial, fused silica radiator material has 100% transmission of UV photons to well below 250 nm and has shown no measurable changes in transmission above 250 nm at a dose of 1 MRad [32]. In tests by the SLAC BaBar DIRC group [33], this material was also shown to have very low scintillation under x-ray bombardment. That result was confirmed on a separate lot of Spectrosil 2000 by the JLab Qweak main detector group. The BaBar DIRC group also showed this material emits negligible luminescence following intense irradiation. The "air" lightguides will consist of thin, aluminum boxes with highly polished interiors. They will be filled with dry air to minimize scintillation and to prevent degradation by nitric acid formation. A schematic view of a single radiator element, its lightguide, and PMT are shown in Figure C.3. Optimizing the lightguide design will entail significant study.

Some parameters of the detector are summarized in Table C.1.

C.2 Current-Mode Signal Magnitude

Assuming only a single radial bin for $e+e \rightarrow e+e$, the track rate in one of the 28 azimuthal bins will be approximately 5.5 GHz. Light in a single azimuthal detector element, as shown in Figure C.3, will be collected by a single 3" PMT with UV glass windows and will conservatively register 10 photoelectrons per track. With the PMT gain adjusted to 675, the resulting signal amplitude will be

$$I_{anode} = 5.5 \text{ GHz} \times 10 \text{ pe/track} \times 675 \times 1.6 \times 10^{-19} e/C = 6 \ \mu A.$$

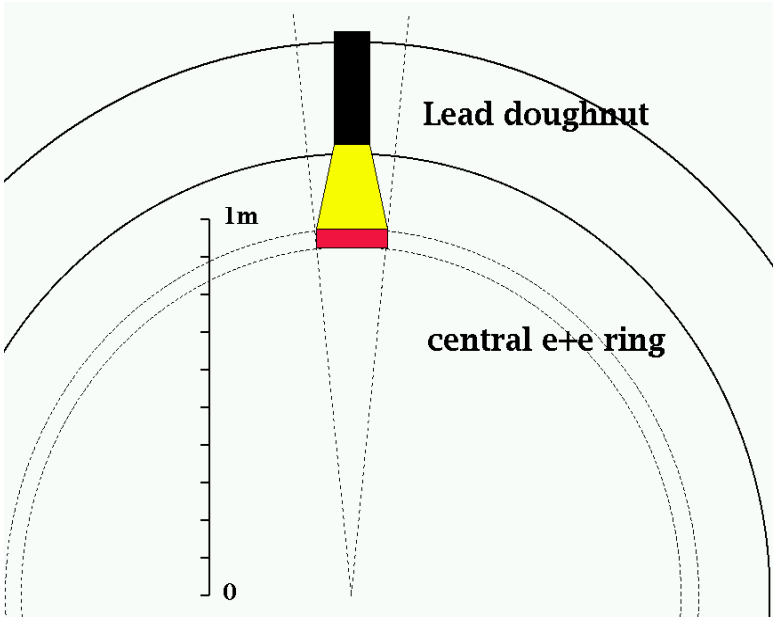

Figure C.3: *Schematic of a single radiator element (red) in the central $e+e$ ring.*

This is a large signal, and still below the nominal 10 μA maximum usually recommended by PMT manufacturers for good long-term stability.

Another consideration for the PMT operational envelope is the *cathode* current of 12 nA. This is far too much current to draw from a standard semiconducting bi-alkali cathode without collapsing the voltage in the center of the cathode, causing defocusing and loss of gain. Hence we will either use a conducting S20 ("multi-alkali") cathode as used in Qweak, or a cathode with thin conducting grid laid across a bi-alkali cathode. The trade-offs are a higher thermionic emission noise in the case of the S20 cathode (which is only an issue at the low rate of the event mode studies), versus reduced quantum efficiency in the case of the cathode overlaid with the conducting grid. The choice will require detailed study.

The current-mode PMT parameters are summarized in Table C.2.

C.3 Event-Mode Signal Magnitude

Event mode operation is helpful for verifying the magnetic optics and essential for detailed background studies. JLab's CW beam and the flexibility of PMTs allows

Table C.1: *Miscellaneous detector parameters.*

Parameter	Value
radiator shape	rectangular (e+p region)
	rhomboidal (e+e region)
radiator size	5 cm (H) x 2 cm (T), length 11 to 25 cm (increases with radius)
radiator material	artificial fused silica (Spectrosil 2000 or JGS1-UV)
radiator position	Z = 28.5 m downstream of the target center)
	(for central $e + e \rightarrow e + e$ detector)
	R = 57.5-62.5 cm (super-elastic region)
	R = 62.5-77.5 cm (e+p events)
	R = 77.5-87.5 cm (e+p tail)
	R = 87.5-102.5 cm (e+e events)
	R = 102.5-112.5 cm (e+e tail)
Lead doughnut dimensions	10 cm (thick) x 117.5 cm (inner radius) x 147.5 cm (outer radius)
Lead doughnut weight	7000 lbs

the detectors to be reconfigured for event-mode operation simply by reducing the beam current, increasing the PMT high voltage, and routing the signal from the parity ADCs (which integrate in 1 msec bins) to flash ADCs (which integrate in bins of a few nsec). At a gain of 1×10^7, the average voltage pulse across a 50 Ω termination is

$$V_{signal} = I_{signal} \times R = (10pe \times 10^7 \times 1.6 \cdot 10^{-19} C/e/10^{-8} sec) \times \ 50\Omega = 80 \text{ mV}$$

which is a robust signal. Even a single photoelectron signal of 8 mV, produced for example by Compton scattering of a few MeV gamma-ray background in the radiator, could be easily observed.

A modest rate of only 100K tracks/second would require the beam current be reduced to 1.5 nA. By employing a combination of laser attenuator and narrow chopper slit, the injector group provided stable beam to Hall C well below 1 nA during a summer '08 Qweak test. The beam position was checked at regular intervals by wire scanners.

The event-mode PMT parameters are also summarized in Table C.2.

C.4 Radiation Hardness

Radiation damage is in principle a concern, since Cerenkov light production occurs predominantly in the UV, which is exactly where loss in light transmission first

Table C.2: *Parameters for the PMT signals in an average azimuthal bin for* $e+e \rightarrow e+e$*. A single radial bin has been assumed.*

Parameter	**Value**
Total PMTs	308 (28 azimuthal bins x 11 radial bins)
current mode:	
$I_{cathode}$	9 nA
gain	675
I_{anode}	6 μA
non-linearity (goal)	5×10^{-3}
pulsed mode:	
$I_{cathode}$	0.16 pA at 100 KHz
gain	1×10^{7}
I_{anode}	1.6 μA
V_{signal} (no amp.)	8 mV for 1 pe; 80 mV for 10 pe
non-linearity (goal)	$< 10^{-2}$

shows up. For example, the familiar "yellowing" of lead-glass is due to the loss of transmitted light at the blue end of the spectrum. The dose to the artificial, fused-silica radiator material from the $e+e \rightarrow e+e$ events will be only 15 MRad by the end of the experiment. Given the average path length in the radiators of only a few cm, and our non-agressive short wavelength cutoff of 250 nm set by the UV glass of the PMT windows, no measurable loss is transmission is expected. This is ideal since it means that the photoelectron yield and any detector biases (e.g., with respect to Q^2) will be stable throughout the experiment.

All other detector construction materials in the beam envelope (such as radiator supports) must be vetted for susceptibility to damage under 15 MRad dose. Degradation by potentially elevated ozone and nitric acid levels may also be a factor in the choice of detector materials.

C.5 Pion Detection

The π/μ fraction at the detector can be estimated in event-mode by placing a thick absorber and scintillator telescope downstream of the main detector. Determining the asymmetry of the small pion background is more difficult because it has to be done in current-mode. We will bound the pion asymmetry at the required level by

dedicated runs in which increasing thicknesses of lead absorbers are placed in front of the radiators. This gradually ranges out the electromagnetic shower products, leaving a signal dominated by charged pions and muons.

It might be that the window-pair widths of the "pion" detector response in current mode are such that one might need quite a long time to bound the anticipated asymmetry of order 1 ppm, at the level of ~ 0.1 ppm. This accuracy is required to control the potential systematic error from the background polarization asymmetry subtraction at the required level. In this case, the "pion" detector will be designed to measure asymmetries in current mode in parallel with physics data collection.

C.6 Very Forward Angle Detectors

We also plan to place detectors at very forward scattering angles; these are typically referred to as "luminosity monitors" in parity experiments. They have two purposes. Due to the higher statistical precision per pulse pair than the main detector, they serve as a sensitive diagnostic of target density fluctuations. The small scattering angle also implies that they should have much smaller expected physics asymmetry than the main detectors, so they serve as a "null-asymmetry monitor".

In the current spectrometer design, it is anticipated that the region at < 2.5 mrad will be a field free region, so a suitable location for luminosity monitors is in the angular range 2.0 - 2.5 mrad at a distance of 30 meters downstream of the target. The scattered electron rate into the full azimuth at this location (coming equally from Moller and elastic e-p scattered electrons) is about 1314 GHz. An array of eight small artificial fused silica radiators with cross section 4 x 1.5 cm can be deployed in the ring from radius 6.0 - 7.5 cm. They can be 1 cm thick and made with a 45° angle to insure light transport through 35 cm long aluminum air-core lightguides. These will couple to 2 inch photomultiplier tubes shielded by lead. The rate in each detector would be about 164 GHz. This geometry is very similar to the geometry of the Q_{weak} downstream luminosity monitors, which have dimensions of 3 cm x 4 cm x 1.7 cm coupled to 35 cm air lightguides with an expected rate of 100 GHz. In that case, we typically collect 10 - 20 photoelectrons per event. Assuming 10 photoelectrons per event, we would expect a photocathode current of 262 nA. Given the similarities to Q_{weak}, we could employ a similar photomultiplier arrangement. A multi-alkali photocathode is used and the dynodes are tied together to run it in "unity-gain" mode. The output is fed into TRIUMF current-to-voltage preamplifier with a gain of 25 MΩ to yield a voltage of 6.6 V.

The total rate in the eight detectors will be $\sim$8.5 times higher than the main

detector, implying a three times smaller statistical error per pulse pair. Assuming the Møller and elastic e-p processes are the largest contributors to the signal in this detector, the expected physics asymmetry is ∼3 ppb, an order of magnitude smaller than the asymmetry in the main detector. So this would serve as a "null-asymmetry" monitor at that level and a check on any corrections procedure applied for helicity-correlated beam parameters.

One technical concern with these detectors is the high radiation dose that will be received by the artifical fused silica over the course of the run. It is about 23 Grad per detector. This is higher than the $\sim$ 2 Grad expected for the Q_{weak} downstream luminosity monitors. Small luminosity monitors made of the Spectrosil 2000 grade material have been demonstrated to show no signficant radiation damage up to 2 Grad exposure in PEPII at SLAC [34]. There is no reason to believe that there will be any degradation as one goes beyond 2 Grad, but if there were, the materials in these detectors are inexpensive enough that periodic replacements are feasible.

Appendix D

Electronics

With little or no modification, the low-noise electronics developed for the Qweak experiment by TRIUMF should be suitable for the 11 GeV Møller measurement. Signals handled by the front end electronics are shown schematically in Figure D.1 for one azimuthal slice assuming all $e + e$ events are collected on a single radial bin. The gain of the photomultiplier is set to yield an anode current of 6 μA. The current signal is converted to a voltage by a transimpedance preamplifier located close to the detectors. The voltage signal goes to electronics outside the Hall where it is sampled at 500 KHz with an 18-bit ADC. These digitized samples are then integrated over each spin state in an internal FPGA. The signal levels anticipated will be similar to those of the Qweak experiment, so the same, or very similar, electronics will be appropriate.

D.1 The TRIUMF Electronics

Preamplifiers Figure D.2 shows one of the preamplifiers built for the main detectors of the Qweak experiment. The main features are:

- Gain: V_{out}/I_{in} = 0.5, 1, 2, or 4 $M\Omega$, switch selectable.
- Output: ±10 volts. Adjustable ±2 V offset. Drives 130 m RG-213 cable.
- Input: current limit set by gain and 10 volt output limit.
- Power: +5 VDC on Lemo connector.
- Bandwidth: f_{3db} = 26 kHz.

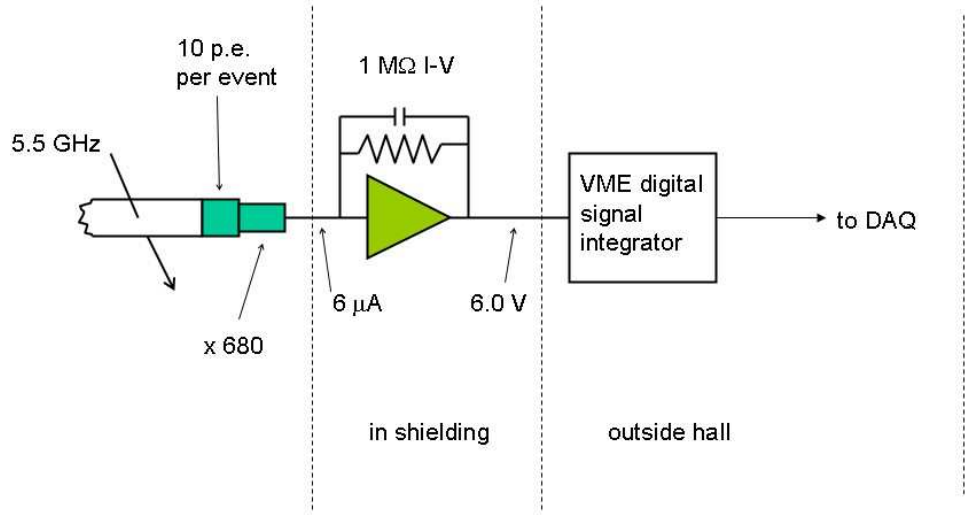

Figure D.1: *Possible front-end signals assuming a 5.5 GHz event rate and 10 photoelectrons per event. The photomultiplier gain is set to deliver 6 μA to the 1 $M\Omega$ current to voltage preamplifier.*

- Noise: 0.5 $\mu V/\sqrt{\text{Hz}}$ referred to output with 1 MΩ gain setting. (Amplifier noise specification assumes the input capacitance of 5 m of RG-62.)
- Packaging: two channels per 80 mm x 70 mm x 28 mm box.

Digital Integrators Figure D.3 shows a TRIUMF digital integrator built for the Qweak experiment. The module has 8 channels in a single width VME module. The main features are:

- Trigger: external NIM signal or internal trigger selectable.
- Integration time: selected as a number of samples, up to 1/30 second.
- Sample rate: selectable up to 500 ksps. 18-bit ADCs.
- Clock: internal 20 MHz or external NIM selectable.
- Input: ±10 volts. High impedance quasi-differential.

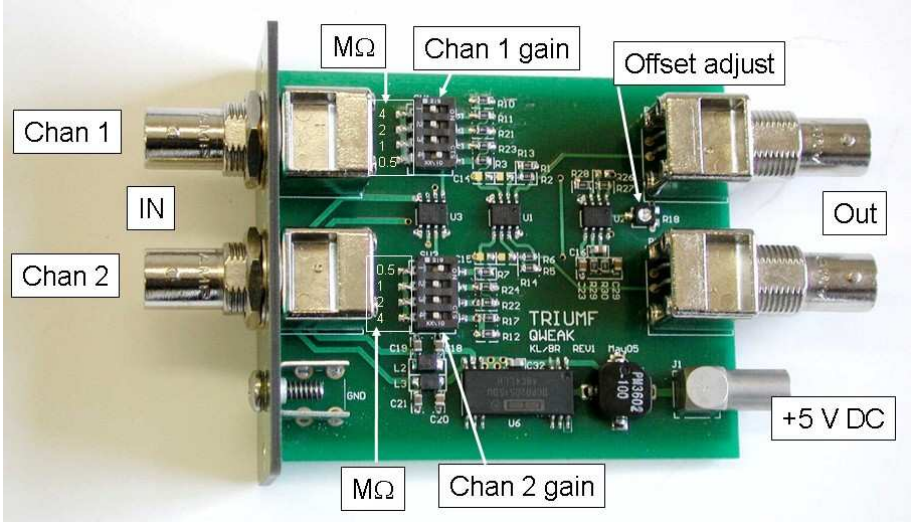

Figure D.2: *TRIUMF current-to-voltage preamplifier for the Qweak experiment.*

- Output: 32 bit sum. The integration period may be sub-divided into up to four blocks. No dead time between blocks.
- Anti-aliasing: 5-pole filter with 50 kHz cutoff.

D.2 Performance

Table D.1 shows that based on reasonable assumptions about the main detector signals on the Møller experiment, the Qweak electronics seem suitable. Noise in the table is referred to the preamp output. The total electronic noise is negligible compared to counting statistics. A null-asymmetry test with a battery-driven current source could be made in one shift at the part per billion level, or 0.1 ppb in 30 days.

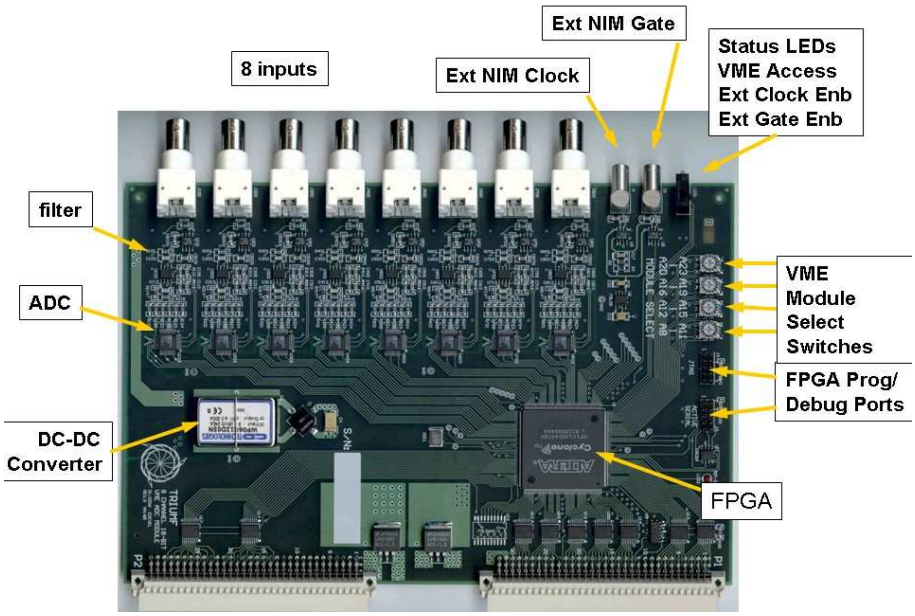

Figure D.3: *TRIUMF VME-based digital integrator for the Qweak experiment.*

Table D.1: *Comparison of various sources of noise assuming the signals of Figure D.1. "Beam on" shot noise is equivalent to counting statistics. The electronic noise is based on tests with TRIUMF electronics built for the Qweak experiment. The electronic noise alone is negligible compared to counting statistics. A null test with a noiseless battery could be made to* $\leq 10^{-9}$ *(one ppb) in a day.*

Type of Noise	charge quantization (e)	Spectral density $\mu V/\sqrt{Hz}$	RMS Noise in 500 Hz BW (1 ms integral)	RMS Noise in 50 KHz BW (VME input)
"beam on" shot	6800	114	2560 μV	25,600 μV
LED test shot	680	36	800 μV	8,000 μV
battery test shot	1	1.4	31 μV	310 μV
preamp		0.5	11 μV	110 μV
digital integrator		1.3	29 μV	290 μV

Appendix E

Hydrogen Target

As mentioned in the discussion of the experimental design, our preliminary assessment using the Computational Fluid Dynamics code `FLUENT` is that the E158 target cell is a good starting point for the design of the high power target required for this experiment. Experience with the Qweak target using JLab's high intensity, CW beam will be crucial for benchmarking our simulations so that the performance of the new target can be predicted with confidence. We also examined whether sufficient target cooling power will be available on site in the 12 GeV era. This can be a complex and potentially contentious issue since it depends on things which simply are not known today, such as the ultimate heat load of the new SRF cavities during 11 GeV operations. However, extremely helpful discussions with the Cryo Group have suggested one logical and reasonable path forward which we present below.

The following sections contain a detailed discussion on these issues.

E.1 Comparable Targets

High-power unpolarized liquid hydrogen (LH_2) targets for parity-violating electron scattering experiments have been around for more than a decade. LH_2 targets with internal heat dissipation of up to 1000 W have been successfully and safely run in the SAMPLE, HAPPEX, PVA4, G0 and E158 experiments. The LH_2 target for the Q_{weak} experiment is the first target in the world that will pass 1000 W in internal heating. The Q_{weak} target is designed for 2500 W and is currently in the manufacturing stage, with commissioning due to start in spring 2010. Although these targets could not be more different in geometry and experimental conditions they all have as a central part a cryogenic closed re-circulation loop, made of a

thin-windowed cell traversed by the beam, a heat exchanger, an in-line pump and a high power heater. The central part of the cryogenic loop is the target cell as it is the region where the interaction between the target fluid (nominally LH_2) and the e^- beam takes place. The rest of the loop is designed around the cell to satisfy the needs for cooling power and fluid flow. In this respect the liquid hydrogen target for an 11 GeV Møller experiment will have the same conceptual components as previous LH_2 targets. The 11 GeV Møller target cell design will have to satisfy the detector acceptance requirements, and, more stringently for such a high precision experiment, the target systematic effects that affect the physics measurement will have to be minimized.

In nominal running conditions the Møller target at 11 GeV is rated for 5000 W, a factor of two beyond the rating for the Q_{weak} target. For the first time for such targets, Computational Fluid Dynamics (henceforth, CFD) simulations were used to design the Q_{weak} target cell. The CFD software engines used were `FLUENT 6.3` and `FLUENT 12.0` developed by Fluent Inc. (now part of ANSYS). CFD simulations played an essential role in designing the Q_{weak} target cell. Two basic models were considered for the Q_{weak} target cell: a G0-type model with a longitudinal flow along the beam line and a model with the flow transverse to the beam line. After a long process of optimization of geometry and flow conditions, it was concluded that a transverse flow design will better satisfy the requirements of that experiment. The steady-state CFD simulations were baselined for the G0 target cell by succesfully predicting the measured pressure drop across it. The transient LH_2 density effects on the time scale of the helicity reversal were not studied with `FLUENT` for the Q_{weak} target cell. Such studies are possible, in principle, but they would require a time frame for modeling and developing that is beyond the Q_{weak} target design time frame. The design of the Møller target will undoubtedly benefit tremendously both from CFD simulations and from the running experience with the Q_{weak} target.

E.2 Target Parameters

The Møller experiment at 11 GeV proposes using a 150 cm long liquid hydrogen target cell. The nominal beam intensity is 85 μA and the nominal beam raster size is 5 mm x 5 mm. The nominal running point for LH_2 in the thermodynamic phase space (p, T) is 35 psia (2.38 atm) and 20 K, although these parameters might change slightly depending on the refrigeration solution for the target. In these conditions the liquid is 3.7 K below the liquid-vapor curve and its density is 71.5 kg/m^3. The target thickness is 10.72 g/cm^2 and its radiation length is 17.5 %. The heating power

deposited by the e^- beam in the target cell is given by

$$P = I\rho L\frac{dE}{dx} \tag{E.1}$$

where ρL is the nominal target thickness in beam, I is the beam intensity and dE/dx is the average energy loss through collisions of one electron in unit target thickness. If $dE/dx = 4.97$ MeV/(g/cm^2) for electrons of 11 GeV in LH_2 then $P = 4533$ W. For an Al target cell made with beam entrance and exit windows of 0.127 mm (0.005") each, the heat deposited by the beam in the windows, calculated with Eq. E.1, is 6.4 W per window. The cumulative beam heating in the target cell is then 4546 W. The nominal parameters of the target and beam are in Table E.1. In order to minimize target density variations, all high power LH_2 targets run in a

Table E.1: *Møller LH_2 target and beam nominal parameters.*

Target Parameters		Beam Parameters	
cell length	150 cm	I, E	85 μA, 11 GeV
cell thickness	10.72 g/cm^2	raster	5 mm x 5 mm
radiation length	17.5 %	beam spot	100 μm
p, T	35 psia, 20 K	detected rate	153 GHz
ϕ acceptance	5 mrad (0.3°)	helicity flip rate	2000 Hz
target power	**5000** W	beam power	**4546** W
ρ fluctuations <**26** ppm			

s

closed feedback loop with the high power heater, allowing a constant heat load on the target to be maintained over time. The heater needs to account for beam heating and target power losses to the environment (such as radiative and viscous losses) and maintain a cooling power buffer for the feedback loop. Based on experience with previous such targets, the losses and the buffer account for about 10 % of the beam heating. Taking this into account the Møller target is rated for 5000 W of cooling power in nominal running conditions, which is a factor of 2 higher than the Q_{weak} target rating, and by far the most powerful LH_2 target ever built and with the most stringent requirements on systematic effects.

The measured detector asymmetry width for the Møller detector is given by $\sigma_m^2 = \sigma_A^2 + \sigma_b^2$, where σ_A is the counting statistics width and σ_b accounts for systematic effects independent of counting statistics, which are typically dominated by

the target density fluctuation (boiling) on the time scale of the helicity pair. For the current design parameters, the projected counting statistics width for the experiment is 77.9 ppm. Target density fluctuations on the level of less than 26 ppm would contribute less than 5 % to the measured asymmetry width, σ_m.

E.3 Density Variation

The Møller target will use LH_2 as the target material and it thus contributes two important systematic uncertainties on the physics measurement: density reduction and density fluctuation. The equation of state of the target fluid in steady-state isobaric conditions is $\rho(p,T) = \rho(T)$. Density reduction is the effect of the fluid density variation with temperature caused by beam heating over the volume of the target cell illuminated by the beam. A LH_2 temperature increase of 1 K causes a density reduction of $\Delta\rho/\rho \approx 1.5$ %. Whenever the beam is on target, a dynamic equilibrium is established in the interaction region, where the temperature of the fluid increases locally with respect to the beam-off condition and the fluid density decreases, resulting in a net reduction of the target thickness in beam. If the target fluid density reduction is e.g. 5 % then the experiment would have to run 5 % longer to get the same statistics as expected from a fixed target density. Density reduction can be predicted analytically for laminar fluid flow and it is usually mitigated by increasing the fluid turbulence in the interaction region.

For the Møller target a laminar fluid flow of 1 kg/s transverse to the beam axis would result in a temperature increase of 0.5 K in nominal running conditions and a relative density decrease of less than 1 %, which would be further decreased by turbulence effects and would be negligible in this experiment. A summary of design parameters and target systematic effects for previous and future LH_2 targets used in parity violation experiments is presented in Table E.2. The quoted target systematic effects for targets that have run before are the measured ones, for the Q_{weak} and the Møller targets they are the desired ones. The two highest power LH_2 targets in the world by almost an order of magnitude have the most stringent requirements for target density fluctuation by almost an order of magnitude compared to most previous targets.

The target density fluctuation effect is usually dominated by the target cell windows region. The heat density deposited by the e^- beam in the thin Al windows is typically one order of magnitude higher than the heat density deposited in LH_2. The heat deposited by the beam in the window material is dissipated through conduction in the window material and convection on only one side of the window, the LH_2 side,

Table E.2: *Liquid hydrogen targets for parity violation experiments. The first group represents actual operating targets, while the last two are targets under design.*

	p/T/$\dot{m}$ psia/K/kg/s	L cm	P/I W/μA	E GeV	beam spot mm	$\Delta\rho/\rho$ %	$\delta\rho/\rho$ ppm
SAMPLE	25/20/0.6	40	700/40	0.2	2	1	<1000 @60Hz
HAPPEX	26/19/0.1	20	500/35-55	3	4.8x4.8 6x3		100
PVA4	25/17/0.13	10	250/20	0.854	0.1	0.1	392 @50Hz
E158	21/20/1.8	150	700/11-12	45/48	1	1.5	<65 @120Hz
G0	25/19/0.3	20	500/40-60	3	2x2	1.5	<238 @30Hz
Q_{weak}	35/19/1	35	2500/180	1.165	4x4		<50 @250Hz
Møller	35/20/1	150	5000/85	11	5x5		<26 @2000Hz

as the other side is exposed to vacuum. The target liquid boils at a window with high probability if two partially correlated effects happen simultaneously: surpassing the critical heat flux and a temperature excursion between the window and the bulk liquid greater than some tens of degrees. Typically for these targets the heat flux from the window to LH_2 is much higher than the critical heat flux for boiling. The critical heat flux for LH_2 at a wall is on the order of 10 W/cm^2 [35]. The total heat flux at the windows in nominal conditions is 43 W/cm^2 for the G0, 78 W/cm^2 for the Q_{weak} and 25.6 W/cm^2 for the Møller targets respectively. CFD simulations revealed that over the beam raster area the convective part of the total heat flux is 18 W/cm^2 for the G0 target and 33 W/cm^2 for the Q_{weak} target. The temperature

excursions determined with CFD for the G0 and the Q_{weak} targets at the windows are on the order 10-30 K. The G0 and the Q_{weak} targets seem likely to develop liquid boiling at the windows. Of these three targets the Møller target has the lowest total heat flux at the windows and careful CFD design could drop the convective part of the total heat flux below the boiling threshold.

From experience with previous LH_2 targets, the effect of density fluctuation is mitigated by optimizing both fluid conditions (flow, turbulence etc.) and beam conditions (raster size, intensity). The measurements done with the G0 target [36] at a helicity flip frequency of 30 Hz indicate a drop by a factor of 2.4 in the magnitude of density fluctuations when the raster size was increased from 2 mm to 3 mm at constant pump rotation, and by a factor of 3.5 when the pump pressure drop was doubled at the same raster size.

For the Møller experiment, we plan to run with a helicity flip frequency (2000 Hz) that is nearly two orders of magnitude greater than the 30 Hz that has been used in the completed Jefferson Lab parity experiments. As noted above, the counting statistics and target density fluctuation asymmetry widths add in quadrature to give the measured statistical width. The advantage of the higher helicity flip frequency is that it is expected to reduce the relative contribution of the target density fluctuations to the measured asymmetry width. As the helicity flip frequency is increased, the counting statistics width increases, while the expectation is that the target density fluctuation width will decrease (or at worst remain constant) with increasing frequency.

To make an estimate of the target density fluctuation width for the Møller target, we use the measured G0 target properties as a starting point. The G0 target has a longitudinal flow design similar to the E158 target, which we are using for prototyping a Møller target cell. The G0 target was run in the CW JLAB electron beam (as opposed to the pulsed beam used in the E158 experiment at SLAC). An upper limit of 238 ppm was observed for the target density fluctuations in the G0 target at 40 μA beam current. We estimate the density fluctuations in the Møller target by using conservative power laws for each of the parameters known to affect density fluctuations. We expect the target density fluctuations to vary inversely with the raster area and linearly with the beam power; these expectations have been borne out by previous target studies. Data from previous targets on the dependence on mass flow rate have not been completely consistent (which could be due to the fact that different target designs were being compared), but the dependence always rises faster than linear. For this estimate, we assume a linear dependence on mass flow rate, which is the most conservative choice.

Finally, we estimate the dependence on helicity flip frequency from an empirical

power law measured in Q_{weak} beam tests done in June 2008. Data were taken at helicity flip frequencies of 30 Hz, 250 Hz, and 1000 Hz on both a carbon and 20 cm hydrogen target at a range of beam currents. The hydrogen target available for the test was not one that was optimally designed for minimization of density fluctuations, but we ran at a variety of beam currents to see if our conclusions were valid over a range of "boiling" conditions. The scattered electron rate was monitored with "luminosity" monitor detectors at small scattering angles. The data from the carbon target were used to determine the parameterization of all sources of random noise other than the target density fluctuation effects in the hydrogen target. The result of the work was the target density fluctuation width as function of helicity flip frequency determined at a variety of beam currents. The results are shown in Figure E.1. A simple power law ($\sigma_b \propto f^{-0.4}$) describes the data well as a function of helicity flip frequency f for the beam currents of 40, 60, and 80 μA. Data were also taken at 10 and 20 μA, but contamination from 60 Hz power line noise made it difficult to draw meaningful conclusions; a refined analysis will be pursued to try to extract information at those currents.

In summary, the assumed scaling arguments for estimating the target density fluctuation widths are: linear in beam power, inversely linear in beam raster area, linear in mass flow rate, and $f^{-0.4}$ in helicity flip frequency. The input parameters for the G0 target are an upper limit of 238 ppm target density fluctuations for a 20 cm long target, 40 μA beam current, 2 mm square raster size, 30 Hz helicity reversal rate, and 0.25 kg/s mass flow rate. The corresponding expected parameters for the Møller target are a target length of 150 cm, 85 μA beam current, 5 mm square raster size, 2000 Hz helicity reversal rate, and 1.0 kg/s mass flow rate. Applying the scaling leads to an estimate that the target density fluctuations for the Møller target could be as large as 26 ppm corresponding to 5% excess random noise. These scaling arguments will be studied in even more detail after the Q_{weak} target is commissioned.

E.4 Cell Design

A 150 cm long cell was used in the 55 liter LH_2 target for the E158 Møller scattering experiment at SLAC at 45 GeV and 48 GeV electron beam energies. The E158 target was rated for 700 W beam heating removal and 1000 W cooling power. The E158 target density fluctuations contributed 65 ppm [37] to a Møller detector asymmetry width of 200 ppm at a repetition rate of 120 Hz or about 5 % of the detector asymmetry. A drawing of the target cell for the E158 experiment is in Fig. E.2. The target was designed and built by a group from Caltech led by Cathleen Jones.

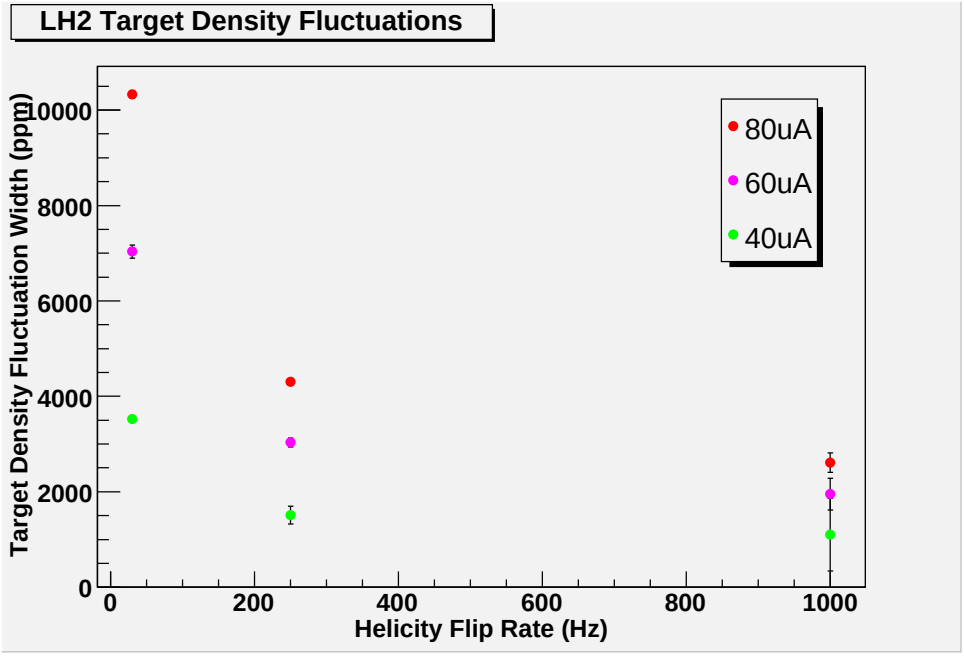

Figure E.1: *Target density fluctuation widths versus helicity flip frequency from recent Q_{weak} beam studies.*

The cell is made of 3" ID pipe with a 3" inlet and outlet that are connected to the rest of the vertical cryogenic loop. Inside the target cell there are 8 wire mesh rings (see Fig. E.2), with a 45^o cut-out and 1.5" diameter clearance in the middle. The rings are thought to increase fluid turbulence and mixing in the cell. This cell is a natural first candidate for a target cell for the Møller experiment at 11 GeV. For this reason the cell design from Fig. E.2 was studied in a steady-state CFD simulation in `FLUENT` under the nominal running conditions from Table E.1. The heating from the electron beam was implemented as a uniform power deposition in the volume of the cell illuminated by the rastered beam to yield 4.5 kW in this volume. The cell walls are made of Al and the beam heating in the windows was implemented also as a uniform power deposition to yield 12.5 W. Hydrogen properties are implemented as functions of temperature in isobaric conditions from the freezing point to 300 K. No boiling model was implemented for hydrogen. The mass rate considered was 1.2 kg/s. The cell volume is 7.8 liters. The cell was simulated both with meshes and without. The results from Figs. E.3a-E.3d are for the cell with internal meshes. The global temperature increase of the LH_2 between the inlet and the outlet to the cell is

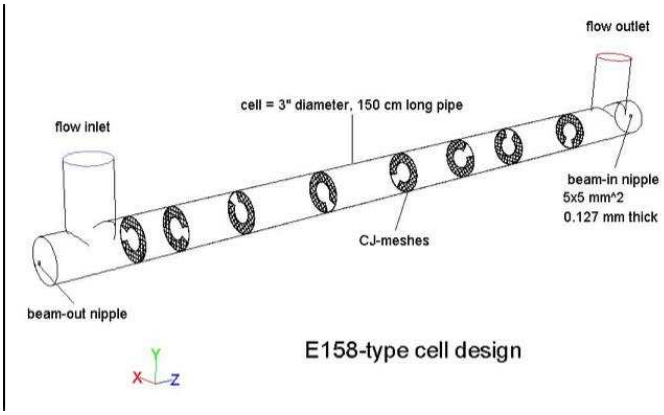

Figure E.2: *E158-type target cell design. Note that the fluid flow (left to right) is opposite the electron beam direction (right to left).*

0.37 K but the average over the beam volume is 1.23 K, which yields a LH_2 density reduction of 2 %. The temperature averaged over the cell windows' beam nipples is 30.1 K for the beam-in window and 34.8 K for the beam-out window. The heat flux, predicted by `FLUENT`, from the window nipples to LH_2 is 4 W/cm^2 for beam-in and 8 W/cm^2 for beam-out respectively, which are both less then the critical heat flux for LH_2. *This would indicate that there is a low probability of liquid boiling at the windows.* Although the cell is symmetrical between the inlet and outlet the flow near the end caps of the cell is not. The cap at the inlet (with the beam-out window) experiences a large vortex with very little flow in the middle, where the liquid seems to be boiling. The pressure drop over this cell at this flow rate is 0.49 psid. The cell design would have to be refined to get rid of the bulk liquid boiling, but it looks promising in the windows region.

E.5 Refrigeration

A preliminary meeting with V. Ganni, D. Arenius and P. Knudsen from the Cryogenics group at JLab took place in Nov. 2008 to try to flesh out a refrigeration solution for the Møller target. If the accelerator delivers electron beams at 11 GeV and all the new SRF cavities continue to show high heatloads, there will be no spare capacity from the new CHL. However the ESR is supposed to undergo a complete makeover with a 4 kW cold box. This ESR-II will deliver 4 kW cooling power at 4 K but it could be modified to deliver 6 kW of cooling power at 15 K and 3 atm.

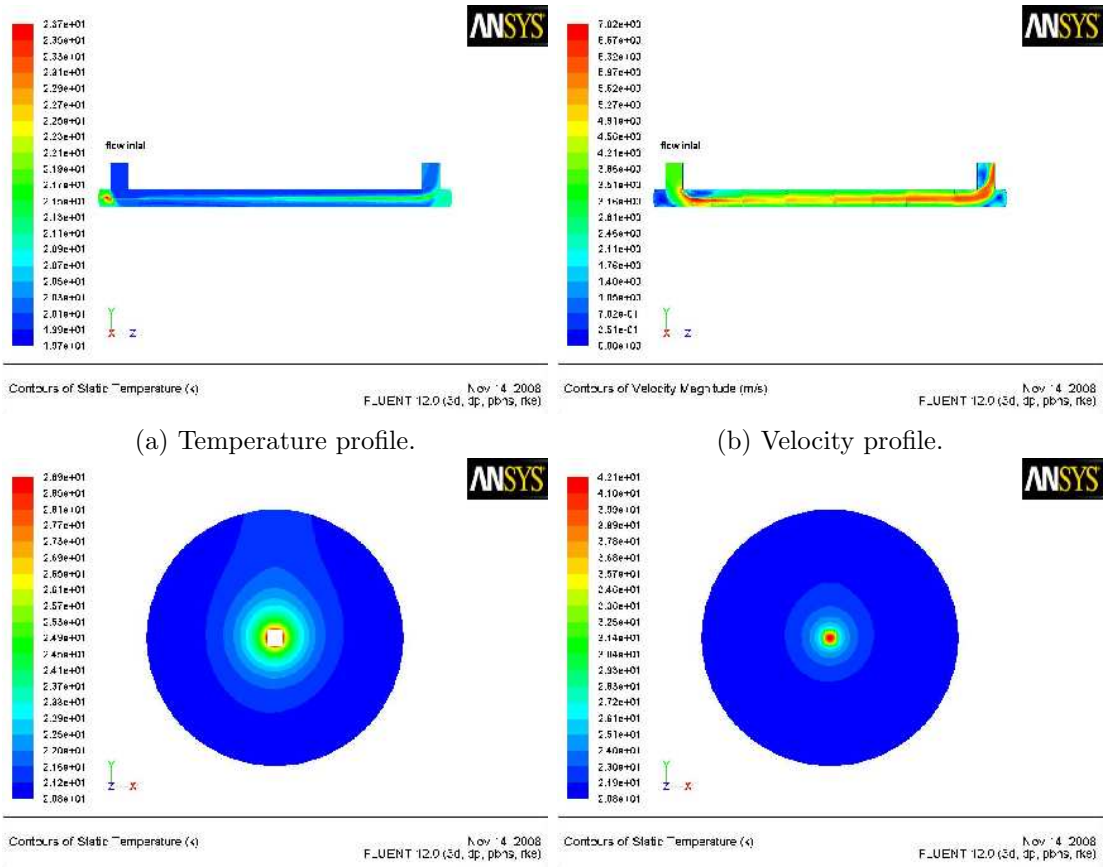

(a) Temperature profile.

(b) Velocity profile.

(c) Beam-out window without nipple.

(d) Beam-out window with nipple.

Figure E.3: *CFD simulations of a E158-type cell in nominal conditions.*

However the return pressure would have to be 2.5 atm, so the expected pressure drop over the target heat exchanger would have to be no more than 0.5 atm. The 6 kW ESR-II seems to be one possible solution for the cooling power needs of the Møller experiment. The ballpark time required for the ESR change would be 2-3 years, but would start only after 12 GeV starts. Along with the cold box installation new coolant delivery lines will have to be installed between the cold box and Hall A to be able to handle flows as high as 200 g/s cold helium gas. This cold box would deliver 5 kW of cooling power with a flow of 183 g/s helium. The cost of the installation of the coolant lines and the change of the cold box from 4 K to 15 K helium was guesstimated to be $1M.

A crude estimate for a counter-flow heat exchanger for 5 kW cooling power working in conjunction with the conditions imposed by a 15 K and 3 atm helium cold box could be made based on a modified Q_{weak} heat exchanger design. The helium flow circuit would be made of two coils in parallel with a total of 24 turns, coil tubing ID of 2 cm, coil fin ID of 4.8 cm and coil diameters of 12.8 cm and 22.4 cm. At the core of the heat exchanger there would be a flow diverter of 8 cm diameter and the shell would have 29 cm diameter with a total length of about 1.2 m and a volume of 85 liters, of which LH_2 would fill about 70 liters. Such a heat exchanger theoretically would deliver a cooling power of 5.2 kW to LH_2 with an expected pressure drop in the helium circuit of 6.5 psid at 172 g/s, and 2 psid in the hydrogen circuit at a mass rate of 1 kg/s.

The other parts of the loop, the high power heater and the pump can be based on the Q_{weak} target designs and running experience. The total hydrogen inventory will depend heavily on a working solution for a heat exchanger. With this crude heat exchanger the target loop would contain on the order of 100 liters, less than twice the hydrogen inventory for the E158 and the Q_{weak} targets respectively.

Appendix F

Compton Polarimetry

Compton polarimetery is a very promising technique for high precision polarimetry at beam energies above a few GeV. Beam interactions with a photon target are non-disruptive, so Compton polarimetry can be employed at high currents as a continuous polarization monitor. The photon target polarization can be measured and monitored with a very high precision, and the scattering between a real photon and free electron has no theoretical uncertainty, such as the atomic or nuclear effects which can complicate other measurements. Radiative corrections to the scattering process are at the level of 0.1% and are very precisely known. The SLD result of 0.5% polarimetry demonstrates the feasibility of very high accuracy Compton polarimetry.

F.1 The Hall A Compton Polarimeter

As pictured in Fig. F.1, the Hall A Compton polarimeter is located in a chicane, about 15 meters long, just below the beamline. After modification to accommodate 11 GeV running, the electron-photon interaction point will be 21 cm below the primary (straight-through) beamline. After the interaction point, the electron beam is bent about 2 degrees by the third chicane magnet and then restored to the main beamline. The scattered electrons are separated from the primary beam and detected using silicon microstrips, just before the fourth chicane magnet. Scattered photons pass through the third chicane magnet to be detected in a calorimeter.

The photon target will be a 0.85 cm long Fabry-Perot cavity containing up to 2 kW of green (532 nm) light. The laser light is polarized using a quarter-wave plate, and can be toggled between opposite polarizations of highly circularly polarized light.

The polarization of the transmitted light from the cavity is continuously monitored, and related to the laser polarization at the interaction point through a precisely measured transfer function. The feedback loop which locks the laser to the cavity resonance can be disabled to enable background measurements.

When well-tuned, the background rates in the photon and electron detectors are similar, and have been held to < 100 Hz/μA in recent use. The dominant source of background is from beam halo or tails intercepting material in the chicane, although Bremstrahlung from interaction with residual gas also contributes. At 11 GeV, the Compton-scattered rates will be in the range of 1 kHz/μA and the asymmetry will range from 32% to -7%. While the details depend on the specific detection and analysis approach is employed, statistical precision of 0.4% can be had in less than 5 minutes for most schemes.

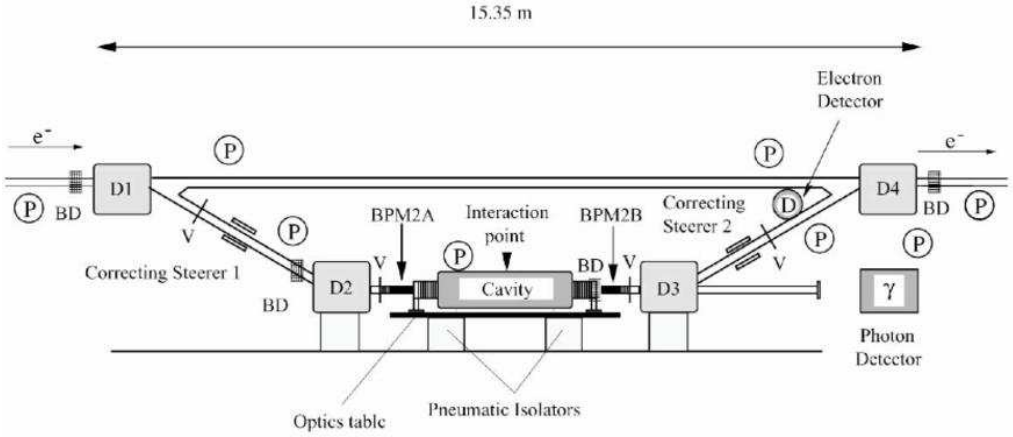

Figure F.1: *Schematic of the Hall A Compton polarimeter. Figure from [38].*

The scattered electrons are detected in 4 planes of silicon microstrips, with 192 strips per plane and a strip pitch of 240 μm, located just upstream of the fourth chicane dipole. The asymmetry is measured as a function of position in the silicon microstrip detector. Although the analyzing power as a function of energy of the Compton scattering process is well-known, an energy calibration is required to convert position in the detector to energy of the electron.

The calorimeter for detecting scattered photons lies about 7 meters downstream of the interaction point. The strong forward boost of scattered photons leads to a tightly collimated photon beam (< 1 mrad), so the calorimeter size relates only to

energy resolution through shower loss. The detector response function is calibrated using the electron detector to tag the photon energy. This response function is convoluted with the expected asymmetry distribution to estimate the analyzing power.

The specific calorimeter to be employed is not yet determined. Hall A has used a lead tungstate array at higher (> 3 GeV) energies. Althought the light yield is low, this is not an issue for higher photon energies of the measurements planned here, and the high speed of this material reduces pile-up issues. At lower energies, Hall A will use a GSO crystal with much higher light yield. This crystal might also be suitable, but it is somewhat slower than the lead tungstate. Designs for multi-layer sampling calorimeters, using either scintillation or Cerenkov light, will also be considered.

F.2 Systematic Uncertainties

Although the electron and photon detectors measure the same scattering events, many of the potential systematic errors arise in detector calibration and are entirely decorrelated between the analyses. Other sources of error, especially those that are related to the scattering process such as photon polarization or the total luminosity, are fully correlated between the two systems. Each of these separate catagories of potential systematic uncertainty: correlated, electron-only, and photon-only, will be discussed in the following sections.

F.2.1 Sources of Correlated Error

Any error associated with the Compton scattering process will be a common source of systematic error between the electron- and photon-detector analyses. One example lies in the energy normalization of the scattering process. The analyzing power is a function of both electron energy and photon energy, so these must be precisely determined. The photon wavelength will be determined to better than 0.1 nm and the electron energy to 5×10^{-4}, which leads to an uncertainty at the level of 0.03%.

A more significant source of error comes from the uncertainty in the photon polarization. The laser polarization at the interaction point is measured directly by opening the vacuum chamber and inserting optical diagnostics. The cavity mirrors must be removed for this measurement, as they do not transmit sufficient light for measurement when the cavity is not resonant. The effect of the mirrors is deduced from the change in the transfer function through the cavity, after the mirrors are

replaced and the cavity locked. This effect is small, typically less than 0.1%. The polariation of the transmitted beam is monitored during production running. In the present Hall A polarimeter, the uncertainty in beam polarization is estimated at 0.35%. Although this number seems quite small, it should be kept in mind that it combines two relatively less challenging measurements: a measure of the depolarization and the linear polarization of the laser light at the level of 8%.

This result can be improved. More frequent measurement of the polarization and monitoring will be required, and a more sophisticated monitoring scheme will be implemented. The effect of vacuum windows will be studied, and if determined to be significant, the strain of the window under vacuum will be included in the transfer function measurement. The circular polarization is near maximum, so the sensitivity to additional birefringence is low. With the necessary effort, the circular polarization of the laser will be known with a precision of not less than 0.2%, which represents an error in the combined linear polarization and depolarization of not worse than 4.5%.

Helicity-correlated changes in luminosity of the laser/electron interaction point can introduce a false asymmetry. Various causes of luminosity variation must be considered, such as electron beam intensity, beam motion or spot-size variation. The control of helicity-correlated beam asymmetries is now a standard technology at Jefferson Lab, and typically achivable results (few part per million intensity, 10's of nanometers beam motion, $< 10^{-3}$ spot size changes) will suitably constrain the electron-photon crossing luminosity variations. Another possible source of false asymmetry would be electronics pickup of the helicity signal, which could potentially impact an integrating photon analysis. However, the demands of the primary experiment for isolation of the helicity signal exceed those for polarimetry by several orders of magnitude. In addition, the laser polarization reversal provides an additional cancellation for asymmetries correlated to the electron beam helicity. Potential effects must be carefully considered, but with due effort, false asymmetries will be a negligible source of uncertainty in this measurement.

Backgrounds are a common, though not fully correlated, problem for the two detector systems. The Hall A polarimeter commonly runs with a signal to background ratio of around 10:1. All known backgrounds are related only to the electron beam, and are not correlated to the presence of the laser light. Frequent, precise background measurements can be easily made by turning off the laser power. As a matter of routine, between 30-60% of data taking is done without the laser, for the purpose of background subtraction. Direct effects of background asymmetries and dilutions are presently estimated to be less than 0.04% in the Hall A system.

F.2.2 Systematic Errors for the Electron Detector

There are two primary sources of potential uncertainty for the electron detector. The first of these is a scale error in the measurement of asymmetries due to an imperfect deadtime correction. The second broadly concerns detector response, spectrometer uniformity and calibration and the impact on the estimated analyzing power.

With data rates potentially up to 100 kHz, DAQ deadtime corrections will be potentially significant, and a dedicated effort to control the related uncertainty will be necessary. The fast-counting DAQ can take very high rates with low deadtimes, and deterministic deadtime intervals are enforced in readout and acquisition electronics stages. The high statistical power of the measurement is of significant use here; the laser power can be varied and the effects mapped to a very high degree of statistical precision. The potential systematic error from deadtime correction arises from asymmetry deadtime associated with the total counting asymmetry. Although the peak asymmetry is high, the total integrated asymmetry is considerably reduced by the accepted range of negative asymmetry. With care, the total asymmetric deadtime correction will introduce no more than 0.2% uncertainty in the determination of polarization.

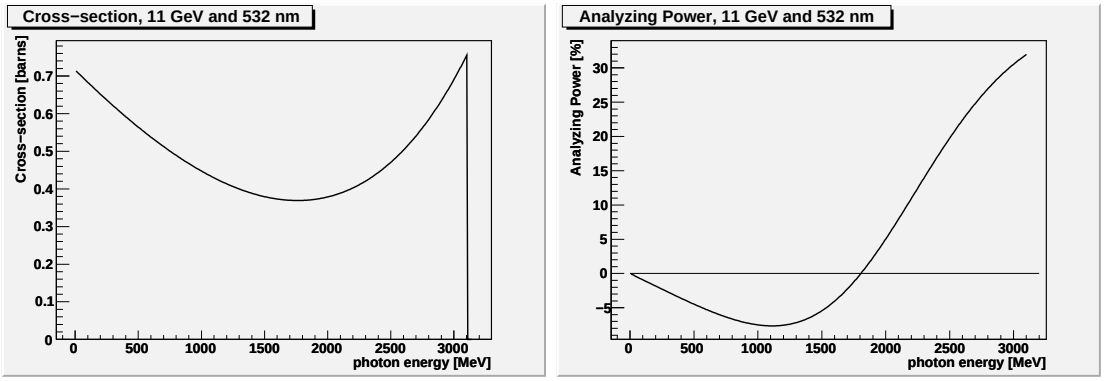

Figure F.2: *The cross-section and asymmetry plotted versus Compton scattered photon energy for the Hall A polarimeter at 11 GeV.*

The analyzing power for the measured electron distribution can be very accurately determined. The calibration is assisted by the accessibility of two easily identified points of well-defined kinematics: the Compton edge and the asymmetry zero-crossing (0-Xing). Both points are fully determined by the beam and photon energies, and provide a precise method for energy calibration of the electron spec-

trum. The asymmetry spectrum for 11 GeV is plotted in Figure F.2. At 11 GeV, the Compton edge is 3.1 GeV below the beam momentum, with a peak asymmetry of $\sim 32\%$, and 0-Xing is 1.8 GeV below beam momentum. At the detector, these are located about 4.7 and 2.7 cm from the primary beam, respectively.

The dominant uncertainties in this method involve the location of these points in the detector and the knowledge of the detector response between the end points. Depending on the analysis method, one can be variously sensitive or insensitive to these uncertainties. Here, we consider three separate methods for analyzing the electron detector data.

- *Integration* The polarization can be determined as a counting asymmetry for the sum of all strips from the Compton edge to the zero crossing.

  Since there is no Compton-scatter rate above the Compton edge, there is no systematic uncertainty in the analyzing power related to the estimated location of this point. The high momentum side of the integration cutoff will not occur precisely at the 0-Xing, but rather at an electron energy corresponding to as much as ± 0.5 of the pitch of the silicon detector strips. Since the asymmetry near the 0-Xing is nearly zero, the error in the 0-Xing location reduces the estimated analyzing power proportionally to the associated fractional change in expected rate; this is effectively an error in background dilution.

  The location of the 0-Xing will be fit using the nearly linear shape of the nearby asymmetry distribution. This procedure will introduce an additional source of statistical noise in the determination of the electron polarization. Small variations in the beam deflection by the third dipole and in the location of the electron detector will reduce systematic bias from the discretization of the data into the silicon strips, or from local differences in efficiency. It should be possible to avoid a systematic bias to a level better than 5% of the width of a strip, which would correspond to a 0.06% effect.

  An error in the 0-Xing location could also arise from an experimental false asymmetry. The slope near the 0-Xing is such that a 0.1% false asymmetry would result in reduction of 0.25% the estimated analyzing power (and so a +0.25% in the measured electron polarization). The false asymmetry would directly represent an error in the electron polarization of about 0.51%, so this effect increases the sensitivity to false asymmetry by factor of about 1.5. Even with this enhancement, the false asymmetry contribution to the polarization will still be negligible.

  Probably the most significant uncertainty in the analyzing power will arise

from efficiency variations among the silicon strips. Strip-by-strip efficiencies can be calculated by comparing track-hit efficiency between the 4 planes of the silicon detector. Inefficiency is expected to be low (less than 1%) and well measured, which will help minimize this effect. Comparison of results from the 4 detector planes will provide a cross-check on this effect, since local variations in asymmetries should be independent between the planes. Significant variations in the location of the detector relative to the primary beam, which would also help control this effect, should be possible, depending on the observed beam halo.

- *Asymmetry Fit* The polarization can also be found from the shape of the asymmetry over all strips between the Compton edge and the zero crossing. This technique would share the small uncertainties on determination of the 0-Xing with the integration technique. However, it would not be sensitive to strip-to-strip variations in efficiency, which is the dominant senstivity for the integration technique.

  This fit would be senstive to knowledge of the magnetic field uniformity. Deviations from the expected shape would introduce systematic uncertainty. Such an an effect may be evident in fit χ^2, could be cross-checked against the rate distribution, and could also be studied in high-statistics electron asymmetry distribution averaged over many runs.

- *Single Strip* The statistical power of the last, single silicon strip at the Compton edge will be significant, capable of 0.5% measurements on time-scales of around 15 minutes. The rate of change of the asymmetry in this region is only 0.9% / mm. Locating this strip, relative to Compton edge, to a little better than half its own width should provide a robust 0.1% accuracy on the analyzing power. This technique would have a greatly reduced sensitivity to the 0-Xing location, dispersion variations or strip efficiency.

For each of these techniques the analyzing power should be estimated with an accuracy of around 0.2% or better. The cross-checks between techniques, each of which have very different sensitivities to possible sources of error, will provide convincing evidence that the system is well understood. Given these considerations, it seems likely that the electron detector analyzing power will not be the dominant source of systematic uncertainty for the polarimetry analysis.

F.2.3 Systematic Errors for the Photon Detector

The determination of the analyzing power is more difficult for the photon calorimeter than for the electron detector due to the width, and shape, of the detector response function. The photon detector analyzing power calculation must convolute this response function with the theoretical analyzing power curve. The response function shape and energy calibration can be studied using the photon tagging through coincidence triggers with the electron detector.

In general, determining the effect of a low-energy threshold on the analyzing power depends sensitively on the shape of the response function; at low energies this is a major source of uncertainty. At high energies, the improved resolution and consistency of the response function shape over the range of interest will significantly reduce this problem. The electron-tagged photon spectrum, which can be calibrated to the zero-crossing and compton edge of the electron spectrum, is crucial to the energy calibration of the photon detector. The optimum location for the low-energy threshold is likely the asymmetry minimum, where uncertainty in the threshold will have minimal effect. Verifing that the electron polariazation result remains constant over variations in the applied lower threshold of the asymmetry analysis provides a useful cross-check of the technique.

Uncertainties related to the threshold, response function shape, and absolute energy calibration can also be eliminated by integrating all signal, without threshold. These previous problems are then replaced with a requirement on the uniformity of the average response over photon energy. At high energies, one expects very uniform behavior, although detector linearity will be crucial. Because the analyzing power integral is energy-weighted, the statistical figure-of-merit in not badly degraded by the negative asymmetry region.

The PREX experiment, with a beam energy of 1.2 GeV, will be unable to detect the asymmetry zero-crossing in the electron detector and so will be relying on the integrating photon method for polarimetry at the level of 1% precision. Complications in the response function for few to 10 MeV photons, and the inability to detect the electrons to tag electrons of such low energy, make that low energy experiment very challenging. Such low energy photons will be only a small correction to the result at 11 GeV. With the ability to study response function with the tagged photon beam over most of the energy range, the photon detector analyzing power normalization in the range of 0.3-0.4% should be achievable.

The rate in the photon detector is similar to that in the electron detector, around 1 kHz/μA, and the deadtime correction represents a similar potential systematic uncertainty. Counting in the photon detector is also senstive to pile-up, which

Relative error (%)	electron	photon
E_{Beam}	0.03	0.03
Laser polarization	0.20	0.20
False asymetries	0.01	0.01
Background	0.05	0.05
Deadtime	0.2	0.0
Pileup	0.0	0.1
Analyzing power	0.15	0.40
Total:	0.33	0.46

Table F.1: *Table of systematic uncertainties for the Hall A Compton polarimeter at 11 GeV. Estimates are described in Sect. F.2.*

distorts the asymmetry distribution. Background and rate distributions will serve as inputs to simulation for corrections on the analyzing power determination. In the current Hall A analysis, pile-up effects are estimated at the level of 1%, and the effect can be controled at a level better than 10% of itself. An integrating photon analysis requires no deadtime correction and has a greatly reduced sensitivity to pile-up, which is a significant advantage for high precision.

F.3 Summary of Compton Polarimetry

The prospects for 0.4% Compton polarimetry are excellent. However, an extremely aggressive and dedicated effort to reducing systematic uncertainty will be required. Table F.3 summarizes the systematic uncertainty estimates discussed above.

These ambitious goals will require vigorous and dedicated efforts to reduce sources of systematic uncertainty. It is expected that some significant fraction of data production time wil be used for studies of the Compton polarimeter system which are not disruptive to the experiment, for example, scans of detector positions, laser power and polarization, data acquisition parameters, etc. The scattering asymmetry at 11 GeV is relatively large, which allows precision at the level of $\sim$0.5% in less than 1 minute of data. Given this high statistical power, these studies will be an effective method for constraining many of the possible experimental systematic uncertainties.

The future use of the Hall A polarimeter at 11 GeV will be a very different situation from the recent operation. The dominant systematic error in recent oper-

ation lay in the determination of the analyzing power. Operating at lower energies, and with an infrared (1064 nm) laser, the asymmetries were significantly lower and therefore the statistical power was worse. In addition, the limits of systematic uncertainty had not been pushed by demands of the experiment precision.

In the case of previous analyses of the electron detector, the zero-crossing calibration had not been exploited. The 0-Xing "integration" analysis was attempted for the first time for the HAPPEX-II and HAPPEX-He measurements. The situation was complicated due to the low beam energy of around 3 GeV, which not only reduced the average asymmetry but also reduced the ratio of Compton-scattered photon energies and the electron energies. At 3 GeV, the zero-crossing was about 5 mm from the primary beam, which was as close as the electron detector could get to the beam. Geometric efficiency at the edge were a signficant complication in this approach. In addition, the microstrip detector was damaged and displayed low and uneven efficiency, which complicated the analysis. The estimated systematic errors for that analysis which were not associated with these efficiency issues are consistent with Table F.3.

For the photon detector, the integration readout method has not yet been used for a physics experiment, and the counting photon analysis was typically limited by uncertainties in the detector response at lower energies. And the rapid access to high statistical power, which is so powerful for cross-checking potential sources of systematic uncertainty, has never before been available to the Hall A Compton.

High-precision Compton polarimetry has also been widely applied at storage rings and colliders. Uncertainties in analyzing power determination have typically limited the precision of high-energy collider Compton photo-detectors to typically $\sim 0.8\%$. These measurements typically use the integrating photon technique for production running, since the electron beam currents are so high. However, in these measurements, photon tagging through coincidence with an electron detector is typically not available for study of the detector response function. The ability of the Hall A Compton polarimeter to perform *in situ* tagged photon calibrations will be a significant advantage.

Appendix G

Møller Polarimeter

G.1 Møller Scattering

Møller polarimeters exploit the properties of the polarized Møller scattering $\vec{e^-} + \vec{e^-} \rightarrow e^- + e^-$. Its unpolarized cross section, first calculated by C. Møller [59], in the Born approximation and the ultrarelativistic limit depends on the scattering angle in c.m. $\Theta_{\rm cm}$ and the Mandelstam variable s as:

$$\frac{d\sigma_\circ}{d\Omega_{\rm cm}} = \frac{\alpha^2}{s} \cdot \frac{(4 - \sin^2\Theta_{\rm cm})^2}{\sin^4\Theta_{\rm cm}}, \tag{G.1}$$

where α is the electomagnetic coupling constant, also presentable as $\alpha = r_e \cdot m_e$, where $r_e = 2.817 \cdot 10^{-13}$ cm is the classical electron radius. In the lab frame of the fixed target experiments, the scattering cross section at $\Theta_{\rm cm} = 90^\circ$ doesn not depend on s:

$$\frac{d\sigma_\circ}{d\Omega}(\Theta_{\rm cm} = 90^\circ) \approx 178 \text{ mb/ster}. \tag{G.2}$$

The polarized cross section depends on the beam and target polarizations $\mathcal{P}_{beam}$ and $\mathcal{P}_{target}$ as:

$$\frac{d\sigma}{d\Omega_{\rm cm}} = \frac{d\sigma_\circ}{d\Omega_{\rm cm}} \cdot (1 + \sum_{i=X,Y,Z} (A^M_{ii} \cdot \mathcal{P}_{targ\ i} \cdot \mathcal{P}_{beam\ i})), \tag{G.3}$$

where $i = X, Y, Z$ defines the projections of the polarizations. The analyzing power A^M, calculated in the same limits as Eq. G.1 [60, 61], depends on the angle $\Theta_{\rm cm}$ and does not depend on s. Assuming that the beam direction is along the Z-axis and

that the scattering happens in the ZX plane:

$$A_{ZZ}^{M} = -\frac{\sin^2\Theta_{\rm cm}\cdot(7+\cos^2\Theta_{\rm cm})}{(3+\cos^2\Theta_{\rm cm})^2}, A_{XX}^{M} = -\frac{\sin^4\Theta_{\rm cm}}{(3+\cos^2\Theta_{\rm cm})^2}, A_{YY}^{M} = -A_{XX}^{M} \quad \text{(G.4)}$$

At $\Theta_{\rm cm} = 90^o$ the analyzing power has its maximum $A_{ZZ\ max}^{M} = 7/9$. A beam transverse polarization in the scattering plane also leads to an asymmetry, though the analyzing power is lower: $A_{XX\ max}^{M} = A_{ZZ}^{M}/7$. The main purpose of the polarimeter is to measure the longitudinal component of the beam polarization.

G.2 Ways to Higher Accuracy

The polarized Møller scattering (described in Section G.1) is a convenient process for measuring the beam polarization. Its counting rate does not depend on the energy, the analyzing power is high (about 80%) and neither depends on the energy, nor changes considerably in the range of the polarimeter acceptance, and two electrons with high energies in the final state make it easy to detect their coincidence and reduce the background to negligible values.

For the polarized electron target only ferromagnetic foils have been used so far [39, 40, 41, 42, 43, 44, 45]. In fully magnetized iron, for instance, about 2.1 electrons from the *d*-shell are polarized and the average electron polarization is about 8%. This value can not be calculated from first principles, but has to be derived from the measured magnetization. Most polarimeters have used foils tilted at an angle of about 20° to the beam and magnetized by external fields of 10-30 mT directed along the beam. In these conditions the magnetization is not fully saturated and depends on many parameters, including the foil annealing and history. The magnetization can be measured, typically with an accuracy of 2-3%. The polarimeter of Hall C at JLab [46, 45] uses foils perpendicular to the beam, magnetized to full saturation in a strong longitudinal field of 3-4 T. In this case, the magnetization has not been measured, but is taken from published data on the properties of bulk iron, which claims an accuracy of $\sim 0.1\%$. In both cases, the orbital contributions to the magnetization of about 5% can be evaluated and subtracted using the magneto-mechanical factor, measured by other dedicated experiments [47]. With strong external fields of 3-4 T several additional correction of about 0.5% have to be made to compensate for extra orbital momenta and other complex effects. These corrections are temperature dependent.

The magnetization of ferromagnetic materials depends on the temperature. The beam heats up the foil and the temperature in the beam area is difficult to measure

or calculate accurately. This limits the average beam current to 2-3 μA, much lower than the current of > 50 μA to be used in the experiment. Using different beam regimes for experiment and polarimetry may become a source of systematic errors, difficult to evaluate. A possible way to solve this problem is to use a fast "kicker" magnet to move the beam back and forth across the edge of a foil located at a distance of about 1 mm from the regular beam position [48].

Another source of errors is the medium-weight atom used for the target. Møller scattering off electrons from the inner atomic shells has a distorted energy-angle correlation for the secondary electrons, with respect to scattering off electrons from the outer shells. A difference of the polarimeter acceptance for these two classes of events is the source of a systematic bias (the so-called Levchuk effect [49]), typically of about 1-5%. This effect forbids using a tight optical collimation of the secondary particles, which would otherwise be favored for background suppression. In most cases, the background is dominated by electron-nucleus scattering and contains one electron in the final state. It can be efficiently suppressed by detecting both secondary Møller electrons in coincidence, however this background typically doubles the detectors' counting rate.

The counting rate depends on the target thickness and the apparatus acceptance. The acceptance should not be too small, because of the Levchuk effect. The associated dead time is typically not negligible and can be an additional source of systematic errors.

The list of systematic errors for the JLab Møller polarimeters in Hall A and Hall C are presented in Table G.1.

Although it is possible to reduce considerably the systematic error of the foil polarization by using a very high magnetization field [45], it is difficult to reduce the other errors, in particular the one associated with the beam current limitations. Also, it is difficult to arrange for continuous measurements since even the thinnest foil used (~ 1 μm) strongly affects the electron beam.

There might be a way to avoid the shortcomings of the ferromagnetic targets. It has been proposed [50, 51, 52] to use polarized atomic hydrogen gas, stored in an ultra-cold magnetic trap, as the target. Such a target of practically 100% polarized electrons would remove the errors associated with the ferromagnetic targets, namely knowledge of the target polarization and the Levchuk effect. The other errors as the analyzing power uncertainty and the dead time can be strongly suppressed. Such a target is thin enough to be used continuously with the experiment. The expected systematic error (see Table G.1) is below 0.5%. A 1% statistical accuracy can be achieved in less than 30 minutes of running. We propose to develop the novel technique of atomic hydrogen targets for Møller polarimetry. This will require

Variable	Hall C	Hall A		
		present	upgraded	proposed
Target polarization	0.25%	2.00%	0.50%	0.01%
Target angle	0.00%	0.50%	0.00%	0.00%
Analyzing power	0.24%	0.30%	0.30%	0.10%
Levchuk effect	0.30%	0.20%	0.20%	0.00%
Target temperature	0.05%	0.00%	0.02%	0.00%
Dead time	-	0.30%	0.30%	0.10%
Background	-	0.30%	0.30%	0.10%
Others	0.10%	0.30%	0.30%	0.30%
Total	0.47%	2.10%	0.80%	0.35%

Table G.1: *A list of systematic errors quoted for the Møller polarimeters in Hall C [45] and in Hall A. The present Hall C configuration is assumed. For Hall A, the first column shows the present configuration, the second column shows the expectations for the high-field target, Hall C style upgrade, which is under way, while the last column shows the expectations for the polarimeter, equipped with an atomic hydrogen target. The regular, low beam current operation is assumed for all, but the last column, which is for operations at high beam currents, but less than* $< 100\ \mu A$.

a dedicated R&D project. Although the technique of hydrogen trapping is well established, there is presently no experience in passing a high intensity beam through such a trap. This project is described in Section G.3.

For the backup solution we consider the technique, being developed for Hall C [48], which involves a polarized foil and a "kicker" magnet used to move the beam. This option is described in Section G.3.10.

In both cases, the spectrometer for the Hall A Møller polarimeter (see Fig. G.1) does not need to be changed.

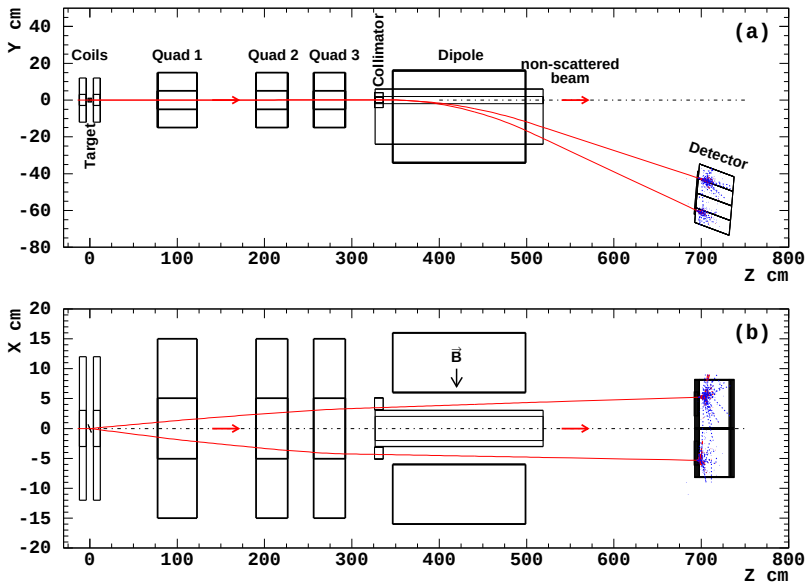

Figure G.1: *The layout of the Hall A Møller polarimeter in it present configuration. The planned upgrade for 12 GeV includes lifting of the detector box to compensate for a smaller deflection in the dipole.*

G.3 Atomic Hydrogen Target

A detailed description of the project can be found in [52]. Here, a summary is presented.

G.3.1 Hydrogen Atom in Magnetic Field

The magnetic field B_S and the hyperfine interaction split the ground state of hydrogen into four states with different energies. The low energy states are $|a\rangle = |\downarrow\uparrow\rangle \cdot \cos\theta - |\uparrow\downarrow\rangle \cdot \sin\theta$ and $|b\rangle = |\downarrow\downarrow\rangle$, where the first and second (crossed) arrows in the brackets indicate the electron and proton spin projections on the magnetic field direction. As far as the electron spin is concerned, state $|b\rangle$ is pure, while state $|a\rangle$ is a superposition. The mixing angle θ depends on the magnetic field B_S and temperature T: $tan\ 2\theta \approx 0.05\ \mathrm{T}/B_S$. At B_S =8 T and $T = 0.3$ K the mixing factor is small: $\sin\theta \approx 0.003$. State $|b\rangle$ is 100% polarized. State $|a\rangle$ is polarized in the same direction as $|b\rangle$ and its polarization differs from unity by $\sim 10^{-5}$.

G.3.2 Storage Cell

In a magnetic field gradient, a force $-\nabla(\vec{\mu_H}\vec{B})$, where μ_H is the atom's magnetic moment, separates the lower and the higher energy states. The lower energy states are pulled into the stronger field, while the higher energy states are repelled from the stronger field. The 0.3 K cylindrical storage cell, made usually of pure copper, is located in the bore of a superconducting ∼8 T solenoid. The polarized hydrogen, consisting of the low energy states, is confined along the cell axis by the magnetic field gradient, and laterally by the wall of the cell (Fig G.2).

At the point of statistical equilibrium, the state population, p follows the Boltzmann distribution:

$$p \propto \exp(\mu_e B/kT), \tag{G.5}$$

where μ_e is the electron's magnetic moment ($\mu_H \approx \mu_e$) and $k = k_B$ is the Boltzmann constant. The cell is mainly populated with states $|a\rangle$ and $|b\rangle$, with an admixture of states $|c\rangle$ and $|d\rangle$ of $\exp(-2\mu_e B/kT) \approx 3 \cdot 10^{-16}$. In the absence of other processes, states $|a\rangle$ and $|b\rangle$ are populated nearly equally. The gas is practically 100% polarized, a small ($\sim 10^{-5}$) oppositely polarized contribution comes from the $|\uparrow\downarrow\rangle$ component of state $|a\rangle$.

The atomic hydrogen density is limited mainly by the process of recombination into H_2 molecules (releasing ∼4.5 eV). The recombination rate is higher at lower temperatures. In gas, recombination by collisions of two atoms is kinematically forbidden but it is allowed in collisions of three atoms. On the walls, which play the role of a third body, there is no kinematic limitation for two atom recombination. At moderate gas densities only the surface recombination matters. In case of polarized atoms, the cross section for recombination is strongly suppressed, because two hydrogen atoms in the triplet electron spin state have no bound states. This fact

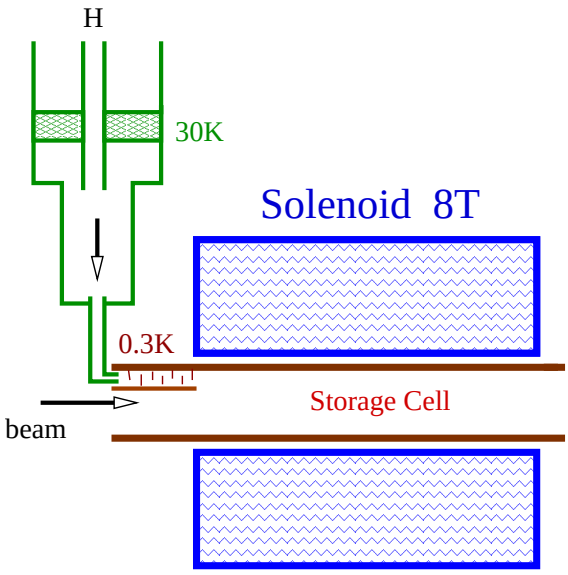

Figure G.2: *A sketch of the storage cell.*

leads to the possibility of reaching relatively high gas densities for polarized atoms in the traps.

A way to reduce the surface recombination on the walls of the storage cell is coating them with a thin film (∼50 nm) of superfluid ^{4}He. The helium film has a very small sticking coefficient[1] for hydrogen atoms.In contrast, hydrogen molecules in thermal equilibrium with the film are absorbed after a few collisions and are frozen in clusters on the metal surface of the trap [53].

The higher energy states are repelled from the storage cell by the magnetic field gradient and leave the cell. Outside of the helium-covered cell, the atoms promptly recombine on surfaces into hydrogen molecules which are either pumped away or are frozen on the walls. Some of the higher energy states recombine within the cell and the molecules eventually are either frozen on the helium-coated wall, or leave the cell by diffusion.

The cell is filled with atomic hydrogen from an RF dissociator. Hydrogen, at 80 K, passes through a Teflon[2] pipe to a nozzle, which is kept at ∼30 K. From the nozzle hydrogen enters into a system of helium-coated baffles, where it is cooled

[1]The sticking coefficient defines the atom's adsorption probability per a collision with a surface.
[2]Teflon has a relatively small sticking coefficient for hydrogen atoms.

down to ∼0.3 K. At 30 K and above, the recombination is suppressed because of the high temperature, while at 0.3 K it is suppressed by helium coating. In the input flow, the atoms and molecules are mixed in comparable amounts, but most of the molecules are frozen out in the baffles and do not enter the cell.

The gas arrives at the region of a strong field gradient, which separates very efficiently the lower and higher atomic energy states, therefore a constant feeding of the cell does not affect the average electron polarization.

This technique was first successfully applied in 1980 [54], and later a density[3] as high as $3 \cdot 10^{17}$ atoms/cm^3 was achieved [55] in a small volume. So far, the storage cell itself has not been put in a high-intensity particle beam.

For the project being discussed a normal storage cell design can be used, with the beam passing along the solenoid axis (Fig. G.2). The double walls of the cylindrical copper cell form a dilution refrigerator mixing chamber. The cell is connected to the beam pipe with no separating windows. The tentative cell parameters are (similar to a working cell [56]): solenoid maximum field of $B_S = 8$ T , solenoid length of $L_S = 30$ cm, cell internal radius of $r_\circ = 2$ cm, cell length of $L_C = 35$ cm and temperature of $T = 0.3$ K. The effective length of such a target is about 20 cm.

For the guideline, we will consider a gas density of $3 \cdot 10^{15}$ cm^{-3}, obtained experimentally [57], for a similar design.

G.3.3 Gas Properties

Important parameters of the target gas are the diffusion speed. At 300 mK the RMS speed of the atoms is ∼80 m/s. For these studies we used a calculated value [58] of the hydrogen atoms cross section $\sigma = 42.3 \cdot 10^{-16}$ cm^2, ignoring the difference between the spin triplet and singlet cross sections. This provided the mean free path $\ell = 0.57$ mm at density of $3 \cdot 10^{15}$ cm^{-3}.

The average time, τ_d for a "low field seeking" atom to travel to the edge of the cell, assuming its starting point is distributed according to the gas density, is[4]: $\tau_d \approx 0.7$ s. This is the cleaning time for an atom with opposite electron spin, should it emerge in the cell and if it does not recombine before. The escape time depends on the initial position of the atom, going from ~ 1 s at $z = 0$ to 0.1 s at $z = 8$ cm. The average wall collision time is about 0.5 ms.

[3] This parameter is called concentration, but we will use the word density in the text, since the mass of the gas is not important here.

[4] This time was estimated using simulation, taking into account the gas density distribution along z and the repelling force in the magnetic field gradient.

G.3.4 Gas Lifetime in the Cell

For the moment we consider the gas behavior with no beam passing through it. Several processes lead to losses of hydrogen atoms from the cell: thermal escape through the magnetic field gradient, recombination in the volume of gas and recombination on the surface of the cell.

The volume recombination can be neglected up to densities of $\sim 10^{17}$ cm^{-3} [55].

The dominant process, limiting the gas density, is the surface recombination. In order to keep the gas density constant the losses have to be compensated by constantly feeding the cell with atomic hydrogen. Our calculations, based on the theory of such cells [55], show, that a very moderate feed rate of $\Phi \sim 1 \cdot 10^{15}$ atoms/s would provide a gas density of $7 \cdot 10^{15}$ cm^{-3}.

This can be compared with the measurement [57] of $3 \cdot 10^{15}$ cm^{-3}. The average lifetime of a "high field seeking" atom in the cell is $\sim$1 h.

G.3.5 Unpolarized Contamination

The most important sources of unpolarized contamination in the target gas in absence of beam have been identified:

1) hydrogen molecules: $\sim 10^{-5}$;

2) high energy atomic states $|c\rangle$ and $|d\rangle$: $\sim 10^{-5}$;

3) excited atomic states $< 10^{-10}$;

4) other gasses, like helium and the residual gas in the cell: $\sim 10^{-3}$

The contributions 1)-3) are present when the cell is filled with hydrogen. They are difficult to measure directly and we have to rely on calculations. Nevertheless, the behavior of such storage cells has been extensively studied and is well understood [55]. The general parameters, like the gas lifetime, or the gas density are predicted with an accuracy better than a factor of 3. The estimates 1)-3) are about 100 times below the level of contamination of about 0.1% which may become important for polarimetry. In contrast, the contribution 4) can be easily measured with beam by taking an empty target measurement. Atomic hydrogen can be completely removed from the cell by heating a small bolometer inside the cell, which would remove the helium coating on this element, and catalyze a fast recombination of hydrogen on its surface. However, it is important to keep this contamination below several percent in order to reduce the systematic error associated with the background subtraction.

G.3.6 Beam Impact on Storage Cell

We have considered various impacts the $\mathcal{I}_b = 100$ μA CEBAF beam can inflict on the storage cell. The beam consists of short bunches with $\tau = \sigma_T \approx 0.5$ ps at a $\mathcal{F} = 499$ MHz repetition rate. The beam spot has a size of about $\sigma_X \approx \sigma_Y \sim 0.1$ mm. The most important depolarization effects we found are:

A) gas depolarization by the RF electromagnetic radiation of the beam: $\sim 3{\cdot}10^{-5}$;

B) contamination from free electrons and ions: $\sim 10^{-5}$;

C) gas excitation and depolarization by the ionization losses: $\sim 10^{-5}$;

D) gas heating by ionization losses: $\sim 10^{-10}$ depolarization and a $\sim$30% density reduction.

The effects A) and B) are described below.

G.3.7 Beam RF Generated Depolarization

The electromagnetic field of the beam has a circular magnetic field component, which couples to the $|a\rangle \rightarrow |d\rangle$ and $|b\rangle \rightarrow |c\rangle$ transitions. The transition frequency depends on the value of the local magnetic field in the solenoid and for the bulk of the gas ranges from 215 to 225 GHz. The spectral density function of the magnetic field can be presented in the form of Fourier series with the characteristic frequency of $\omega_\circ = 2\pi\mathcal{F}$. The Fourier coefficients are basically the Fourier transforms of the magnetic field created by a single bunch. The bunch length is short in comparison with the typical transition frequency ($\omega_{trans}\tau \sim 0.1$). The resonance lines of the spectrum (a reflection of the 499 MHz repetition rate) populate densely the transition range (see Fig. G.3). The induced transition rate depends on the gas density at a given transition frequency. This rate was calculated taking into account the beam parameters and the field map of a realistic solenoid. Provided that the field of the solenoid is fine tuned to avoid the transition resonances for the bulk of the gas in the cell (see Fig. G.3), the depolarization described has the following features:

- the transition rate is proportional to $\mathcal{I}_b^2$;
- the average rate of each of the two transitions is about $0.5 \cdot 10^{-4}$ of the target density per second;
- at the center around the beam the full transition rate is about 6% of the density per second.

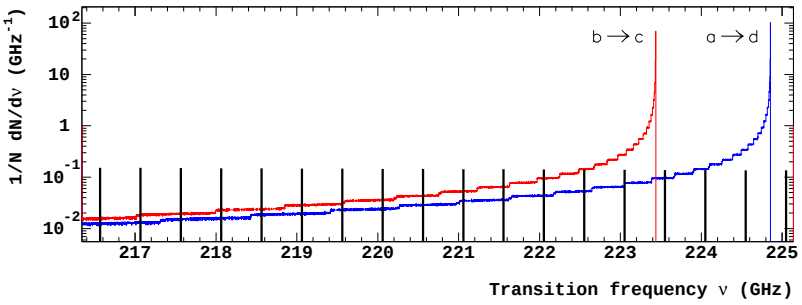

Figure G.3: *Simulated spectra of the transitions on the axis of the hydrogen trap with the maximum field of 8.0 T. The density of atoms depends on the field as* $exp(-\mu_e B/kT)$. *The two curves show* $\frac{1}{N}dN/d\nu_{ad}$ *and* $\frac{1}{N}dN/d\nu_{bc}$ *- the relative number of atoms which can undergo* $|a\rangle \rightarrow |d\rangle$ *and* $|b\rangle \rightarrow |c\rangle$ *transitions at the given frequency, per one GHz. The resonant structure of the spectral function of the beam-induced electromagnetic field is shown as a set of vertical bars, 499 MHz apart.*

In order to estimate the average contamination we take into account that each resonance line presented in Fig. G.3 corresponds to a certain value of the solenoid field and, therefore, affects the gas at a certain z. Using a realistic field map of the solenoid we obtained that the average depolarization in the beam area will be reduced to about $\sim 0.3 \cdot 10^{-4}$ by the lateral gas diffusion and by the escape of the "low field seeking" atoms from the storage cell.

In order to study experimentally the depolarization effect discussed, one can tune the solenoid magnetic field to overlap a resonance line with the transition frequency of the gas at the cell center. This would increase the transition rate by a factor of ∼70.

G.3.8 Contamination by Free Electrons and Ions

The beam would ionize per second about 20% of the atoms in the cylinder around the beam spot. The charged particles would not escape the beam area due to diffusion, as the neutral atoms would do, but will follow the magnetic field lines, parallel to the beam. An elegant way to remove them is to apply a relatively weak ∼1 V/cm electric field perpendicular to the beam. The charged particles will drift at a speed of $v = \vec{E} \times \vec{B}/B^2 \sim 12$ m/s perpendicular to the beam and leave the beam area in about 20 μs. This will reduce the average contamination to a 10^{-5} level.

G.3.9 Application of the Atomic Target to Møller Polarimetry

This feasibility study was done for the possible application of the target discussed to the existing Møller polarimeter in Hall A at JLab.

The beam polarization at JLab is normally about 80%, at beam currents below 100 μA. Scaling the results of the existing polarimeter to the hydrogen target discussed we estimated that at 30 μA a 1% statistical accuracy will be achieved in about 30 min. This is an acceptable time, in particular if the measurements are done in parallel with the main experiment.

There is no obvious way to measure directly the polarization of the hydrogen atoms in the beam area. The contamination from the residual gas is measurable. The rest relies on calculations. All calculations show that the polarization is nearly 100%, with a possible contamination of <0.01%, coming from several contributions. The impact of the most important of these contributions can be studied, at least their upper limits, by deliberately increasing the effect. For example, the beam RF induced transitions can be increased by a factor of ∼70, by fine tuning of the solenoid magnetic field. The contribution from the charged particles in the beam area can be varied by a factor up to $\sim 10^4$, by changing the cleaning electric field.

The systematic errors, associated with the present Hall A polarimeter, when added in quadrature give a total systematic error of about 3%. Scaling these errors to the design with the hydrogen target reduces the total error to about 0.3%. If we scale the accuracy of the Hall C polarimeter (see Table G.1), the projected total error would be better than 0.2%. There is no doubt that achieving such an accuracy is a major challenge and will require re-evaluation of the error budget for including smaller effects, so far neglected. However, the technique described has a potential to deliver an accuracy of 0.4% required for the experiment proposed.

G.3.10 Møller Polarimeter in Hall C

The Hall C Møller polarimeter was originally designed and constructed by the Basel Nuclear Physics group to overcome what has been to date, the most significant systematic uncertainty in the Møller polarimetry technique - namely the knowledge of the polarization of the "target" used in the measurement of the double–spin Møller scattering asymmetry.

As described in Sec. G, the Hall C Møller polarimeter makes use of a pure iron foil, typically 1 to 10 μm thick oriented perpendicular to the electron beam direction and brute–force polarized out of plane using a 3–4 T superconducting solenoid. In

principle, such a target results in kowledge of the target polarization to better than 0.25% [62].

One drawback of this saturated foil target, however, is the need to avoid significant temperature changes due to beam heating. As seen in Fig. G.4, a temperature increase of 60–70 degrees C results in a reduction of the target polarization of $\approx 1\%$. The need to avoid such temperature changes typically limits the beam current used in Møller measurements to 1-2μA. Higher currents can and have been used in Hall C using a circular raster of ≈1 mm radius to limit beam heating. However, even with a large raster, practical beam currents are limited to 20 μA before beam heating becomes significant. This is still well away from the nominal current ($> 50\mu$A) to be used in this experiment. In principle, measurements using the Kerr effect may be used to monitor the relative target polarization, but this requires that the laser impinge on the iron foil at precisely the same point (and perhaps with the same shape) as the electron beam.

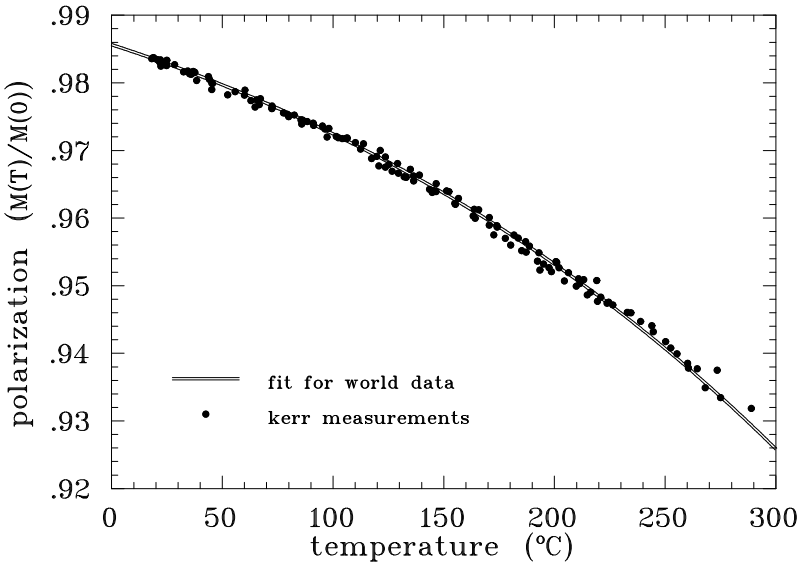

Figure G.4: *Relative magnetization vs. temperature for a pure iron foil driven to magnetic saturation (from [62]). The iron foil used in the Hall C Møller polarimeter is normally at room temperature with no active cooling.*

One can attempt to mitigate foil heating effects using a fast beam kicker system combined with a thin strip or wire target. In this system, the electron beam is kicked at some low duty cycle onto or across a pure iron target. The beam is only impinging

on the target for timescales on the order of μs such that the target does not have much opportunity to heat up, while the relatively long time between kicks allows the target to cool.

A series of tests have been performed in Hall C with two prototype kicker magnets and two different target configurations [48]. Initial tests were performed with 25 μm diameter iron wires replacing the iron foil at the Møller target. While these tests were moderately successful, it was found that the high instantaneous current combined with the relatively thick profile of the target lead to a high rate of random coincidences. The second generation prototype target replaced the iron wires with a 1 μm strip target, reducing the instaneous rate.

Results from the second generation tests are shown in Fig. G.5. In this case, the duration of the beam "kick" was about 10 μs at a repetition rate between 5 and 10 kHz. Data were taken using the kicker and iron strip target up to 40 μA. In general, the results were consistent with there being no effect from target heating, albeit with relatively low precision. Problems with beam transport precluded the use of higher beam currents. Finally, it should be noted that apparent instabilities with either the source or Hall C Møller polarimeter itself (found by taking "calibration" data at 2 μA from a normal iron foil) made it difficult to conclude that target heating effects were completely avoided.

An improved kicker magnet capable of scanning the beam across an iron strip target in ≈ 1 μs has been constructed and will be installed for the Q_{Weak} experiment in Hall C. In addition to the improved kick speed, the new kicker will hold the electron beam at a nearly fixed position on the foil (see Fig. G.6) such that one can gate off the data–taking during periods in which the beam is "in transit." We estimate that allowing the beam to dwell on the iron strip target for periods of $\approx$1 μs with a frequnecy of 2.5 kHZ will keep target depolarization due to heating effects to the 1% level.

Application of a similar technique for this experiment requires consideration of several issues. First, the fastest kicker magnet developed for Hall C will only operate up to a beam energy of $\approx$2 GeV. Given that the currents will likely be about a factor of three smaller, a slower kicker is likely acceptable. For example, a kick duration of 8 μs is sufficiently fast to keep target depolarization effects at the 1% level. Space in the beamline would need to be found, preferably far from the Møller target region to maximize deflection for a given $\int \vec{B} \cdot d\vec{l}$. Also, it should be noted that for the Hall C system, up to 1% effects are deemed acceptable, assuming that we can estimate the correction to the target polarization with a precision of something like 50% of the size of the effect. Since the goal here is 0.5% polarimetry, the allowed effects from target heating will need to be smaller. A kicker capable of kick durations of

≈4 μs yielding 1-2 mm deflection at the Møller target at 11 GeV would need to be designed and built.

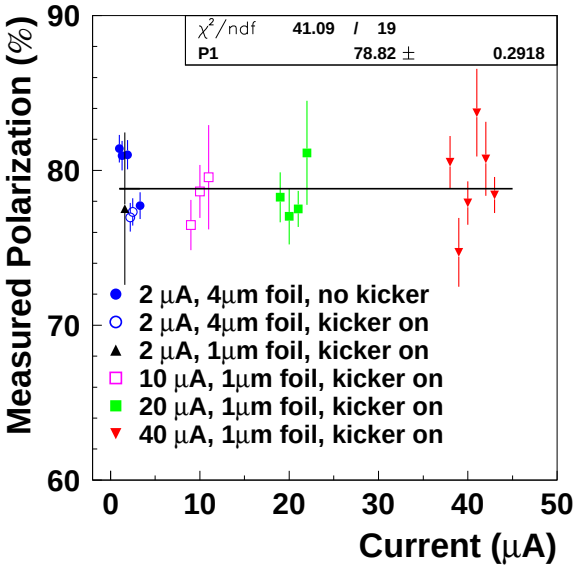

Figure G.5: *Results of polarization measurements taken in Hall C using the second generation kicker magnet impinging on a 1 μm thick iron foil strip target. Measurements were made at beam currents up to 40 μA. Higher currents were not accessible to due to beam losses from the deflected electron beam. Control measurements at 2 μA were not stable, so these measurements cannot be used to prove 1% precision at high currents.*

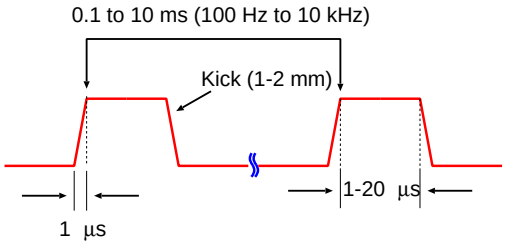

Figure G.6: *Schematic of the operating mode of the new kicker magnet to be installed for Q_{Weak}. The beam is kicked 1-2 mm in about 1 μs and remains stationary on the Møller target for 1 to several μs.*

Bibliography

[1] P. L. Anthony *et al.* [SLAC E158 Collaboration], Phys. Rev. Lett. **95**, 081601 (2005) [arXiv:hep-ex/0504049].

[2] Nuclear Science Advisory Committee Long Range Planning Document (2007): http://www.sc.doe.gov/np/nsac/nsac.html

[3] Ya.B. Zel'dovich, Sov. Phys. JETP **94**, 262 (1959).

[4] E. Derman and W. J. Marciano, Annals Phys. **121**, 147 (1979).

[5] A. Czarnecki and W. J. Marciano, Phys. Rev. D **53**, 1066 (1996) [arXiv:hep-ph/9507420].

[6] J. Erler and M. J. Ramsey-Musolf, Phys. Rev. D **72**, 073003 (2005) [arXiv:hep-ph/0409169].

[7] G. P. Zeller *et al.* [NuTeV Collaboration], Phys. Rev. Lett. **88**, 091802 (2002) [Erratum-ibid. **90**, 239902 (2003)] [arXiv:hep-ex/0110059].

[8] C. Amsler *et al.* [Particle Data Group], Phys. Lett. B **667**, 1 (2008).

[9] R. Barate *et al.* [LEP Working Group for Higgs boson searches and ALEPH Collaboration and and], Phys. Lett. B **565**, 61 (2003) [arXiv:hep-ex/0306033].

[10] [ALEPH Collaboration and DELPHI Collaboration and L3 Collaboration and OPAL Collaboration and SLD Collaboration and LEP Electroweak Working Group and SLD Electroweak Group and SLD Heavy Flavour Group], Phys. Rept. **427**, 257 (2006) [arXiv:hep-ex/0509008].

[11] W. J. Marciano, AIP Conf. Proc. **870**, 236 (2006).

[12] E. Eichten, K. D. Lane and M. E. Peskin, Phys. Rev. Lett. **50**, 811 (1983).

[13] M. J. Ramsey-Musolf, Phys. Rev. C **60**, 015501 (1999) [arXiv:hep-ph/9903264].

[14] A. Kurylov, M. J. Ramsey-Musolf and S. Su, Phys. Rev. D **68**, 035008 (2003) [arXiv:hep-ph/0303026].

[15] M. J. Ramsey-Musolf and S. Su, Phys. Rept. **456**, 1 (2008) [arXiv:hep-ph/0612057].

[16] J. Erler and P. Langacker, Phys. Lett. B **456**, 68 (1999) [arXiv:hep-ph/9903476].

[17] F. Petriello, S. Quackenbush, Y. Li, private communication.

[18] V. Cirigliano, A. Kurylov, M. J. Ramsey-Musolf and P. Vogel, Phys. Rev. D **70**, 075007 (2004) [arXiv:hep-ph/0404233].

[19] P. A. Souder *et al.*, Phys. Rev. Lett. **65**, 694 (1990).

[20] D. T. Spayde *et al.* [SAMPLE Collaboration], Phys. Lett. B **583**, 79 (2004) [arXiv:nucl-ex/0312016].

[21] A. Acha *et al.* [HAPPEX collaboration], Phys. Rev. Lett. **98**, 032301 (2007) [arXiv:nucl-ex/0609002].

[22] The Lead Radius Experiment PREX, E06002, K. Kumar, R. Michaels, P. Souder, G. Urciuoli spokespersons, http://hallaweb.jlab.org/parity/prex/ .

[23] The Qweak Experiment, http://www.jlab.org/Hall-C/Qweak/index.html, , R. Carlini Principal Investigator.

[24] C. Y. Prescott *et al.*, Phys. Lett. B **77**, 347 (1978).

[25] K. D. Paschke, Eur. Phys. J. A **32**, 549 (2007).

[26] K. Abe *et al.* [SLD Collaboration], Phys. Rev. Lett. **84**, 5945 (2000) [arXiv:hep-ex/0004026].

[27] HAPPEXIII: Jefferson Laboratory Experiment E05-009, K. Paschke and P. Souder spokespersons.

[28] Jefferson Laboratory Experiment E05-007, X. Zheng, Contactperson.

[29] S. Agostinelli *et al.* [GEANT4 Collaboration], Nucl. Instrum. Meth. A **506**, 250 (2003).

[30] M. Gericke, "Excess Noise as a Function of Detector Thickness", September 1, 2005, a Qweak technical note available at http://qweak.jlab.org/doc-public/ShowDocument?docid=532 .

[31] R.S. Hicks *et al.*, "Flux Profile Scanners for Scattered High-Energy Electrons", NIM **A553** (2005), pp 470-482.

[32] K. Kinsley, "Measurement of Light Transmission in Radiation Damaged Quartz Bars for Qweak", September 10, 2007, a Qweak technical note available at http://qweak.jlab.org/doc-public/ShowDocument?docid=695 .

[33] J. Cohen-Tanugi *et al.*, "Optical Properties of the DIRC Fused Silica Cherenkov Radiator", NIM **A515** (2003), pp 680-700.

[34] S. Ecklund *et al.*, NIM **A463** (2001) 68.

[35] E. G. Brentari et al., 1965, *Boiling Heat Transfer for Oxygen, Nitrogen, Hidrogen, and Helium*, National Bureau of Standards, TN 317

[36] S. D. Covrig et al., 2005, *The cryogenic target for the G0 experiment at Jefferson Lab*, Nucl. Instr. and Meth. **A 551**, 218-235

[37] J. Gao et al., 2003, *A liquid hydrogen target for the precision measurement of the weak mixing angle in Møller scattering at SLAC*, Nucl. Instr. and Meth. **A 498**, 90-100

[38] N. Falletto *et al*, "Compton scattering off polarized electrons with a high finesse Fabry-Perot cavity at JLab,", *"Nucl. Instrum. Meth."*, A459, 212-425, 2001.

[39] P. S. Cooper *et al.*, "Polarized electron Electron Scattering at GeV Energies," *Phys. Rev. Lett.*, vol. 34, p. 1589, 1975.

[40] B. Wagner *et al.*, "A Møller polarimeter for CW and pulsed intermediate-energy electron beams," *Nucl. Instrum. Meth.*, vol. A294, pp. 541–548, 1990.

[41] J. Arrington *et al.*, "A Variable energy Møller polarimeter at the MIT Bates Linear Accelerator Center," *Nucl. Instrum. Meth.*, vol. A311, pp. 39–48, 1992.

[42] K. B. Beard *et al.*, "Measurement of the polarization of a pulsed electron beam with a Møller polarimeter in the coincidence mode," *Nucl. Instrum. Meth.*, vol. A361, pp. 46–52, 1995.

[43] H. R. Band, G. Mitchell, R. Prepost, and T. Wright, "A Møller polarimeter for high energy electron beams," *Nucl. Instrum. Meth.*, vol. A400, pp. 24–33, 1997.

[44] A. V. Glamazdin *et al.*, "Electron beam Moeller polarimeter at JLAB Hall A," *Fizika*, vol. B8, pp. 91–95, 1999, hep-ex/9912063.

[45] M. Hauger *et al.*, "A high-precision polarimeter," *Nucl. Instrum. Meth.*, vol. A462, pp. 382–392, 2001, nucl-ex/9910013.

[46] P. Steiner, A. Feltham, I. Sick, M. Zeier, and B. Zihlmann, "A high-rate coincidence Møller polarimeter," *Nucl. Instrum. Meth.*, vol. A419, pp. 105–120, 1998.

[47] G. G. Scott, "Review of gyromagnetic ratio experiments," *Rev. Mod. Phys.*, vol. 34, pp. 102–109, Jan 1962.

[48] D. Gaskell, D. G. Meekins, and C. Yan, "New methods for precision Møller polarimetry," *Eur. Phys. J.*, vol. A32, pp. 561–564, 2007.

[49] L. G. Levchuk, "The Intraatomic motion of bound electrons as a possible source of a systematic error in electron beam polarization measurements by means of a Møller polarimeter," *Nucl. Instrum. Meth.*, vol. A345, pp. 496–499, 1994.

[50] E. Chudakov and V. Luppov, "Møller polarimetry with atomic hydrogen targets," *IEEE Trans. Nucl. Sci.*, vol. 51, pp. 1533–1540, 2004.

[51] E. Chudakov and V. Luppov, "Moeller polarimetry with atomic hydrogen targets," *Eur. Phys. J.*, vol. A24S2, pp. 123–126, 2005.

[52] E. Chudakov and V. Luppov, "Møller polarimetry with atomic hydrogen targets," tech. rep., JLab, 2005. `http://www.jlab.org/~gen/hyd/loi_3.pdf`.

[53] I. F. Silvera, "Ultimate fate of a gas of atomic hydrogen in a liquid-helium chamber: Recombination and burial," *Phys. Rev. B*, vol. 29, pp. 3899–3904, Apr 1984.

[54] I. F. Silvera and J. T. M. Walraven, "Stabilization of atomic hydrogen at low temperature," *Phys. Rev. Lett.*, vol. 44, pp. 164–168, Jan 1980.

[55] I. F. Silvera and J. T. M. Walraven, "Spin polarized atomic hydrogen," *Progress in Low Temperature Physics, vol. X*, pp. 139–370, 1986.

[56] T. Roser *et al.*, "Microwave driven extraction of stabilized spin polarized atomic hydrogen," *Nucl. Instrum. Meth.*, vol. A301, pp. 42–46, 1991.

[57] M. Mertig, V. G. Luppov, T. Roser, and B. Vuaridel, "Continuous density measurement of atomic hydrogen by means of a bolometer," *Rev. Sci. Instrum.*, vol. 62, pp. 251–252, 1991.

[58] M. D. Miller and L. H. Nosanow, "Possible "new" quantum systems. ii. properties of the isotopes of spin-aligned hydrogen," *Phys. Rev. B*, vol. 15, pp. 4376–4385, May 1977.

[59] C. Møller, "Zur Theorie des Durchgangs schneller Elektronen durch Materie," *Annalen der Physik*, vol. 406, pp. 531–585, 1932.

[60] A. A. Kresnin and L. N. Rosentsveig, "Polarization asymmetry of møller scattering," *Soviet JETP*, vol. 5, pp. 288–292, 1957.

[61] A. M. Bincer, "Scattering of longitudinally polarized fermions," *Phys. Rev.*, vol. 107, pp. 1434–1438, Sep 1957.

[62] L. V. de Bever, J. Jourdan, M. Loppacher, S. Robinson, I. Sick and J. Zhao, "A target for precise Mller polarimetry," *Nucl. Instrum. Meth.*, vol. A400, pp. 379–386, 1997.